LBL-36126
UC-400

Lawrence Berkeley Laboratory

UNIVERSITY OF CALIFORNIA

EARTH SCIENCES DIVISION

Analysis of In-Situ Rock Joint Strength Using Digital Borehole Scanner Images

B.B. Thapa
(Ph.D. Thesis)

September 1994

Prepared for the U.S. Department of Energy under Contract Number DE-AC03-76SF00098

Analysis of In-Situ Rock Joint Strength Using Digital Borehole Scanner Images

By

Bhaskar Bahadur Thapa

B.S. (Carnegie-Mellon University) 1985
M.S. (Carnegie-Mellon University) 1987

A dissertation submitted in partial satisfaction of the

requirements for the degree of

Doctor of Philosophy

in

Engineering-Civil Engineering

in the

GRADUATE DIVISION

of the

UNIVERSITY OF CALIFORNIA at BERKELEY

Committee in charge:

Professor Richard E. Goodman
Professor Nicholas Sitar
Professor H. Frank Morrison
Professor Chikaosa Tanimoto

1994

Analysis of In-Situ Rock Joint Strength Using Digital Borehole Scanner Images

by

Bhaskar Bahadur Thapa

Abstract

Analysis of In-Situ Rock Joint Strength Using Digital Borehole Scanner Images

by

Bhaskar Bahadur Thapa

Doctor of Philosophy in Engineering-Civil Engineering

University of California at Berkeley

Professor Richard E. Goodman, Chair

The availability of high resolution digital images of borehole walls using the Borehole Scanner System has made it possible to develop new methods of in-situ rock characterization. This thesis addresses particularly new approaches to the characterization of in-situ joint strength arising from surface roughness.

An image processing technique is used to extract the roughness profile from joints in the unrolled image of the borehole wall. A method for estimating in-situ Rengers envelopes using this data is presented along with results from using the method on joints in a borehole in porphyritic granite. Next, an analysis of the joint dilation angle anisotropy is described and applied to the porphyritic granite joints. The results indicate that the dilation angle of the joints studied are anisotropic at small scales and tend to reflect joint waviness as scale increases.

A procedure to unroll the opposing roughness profiles a joint to obtain a two dimensional sample is presented. The measurement of apertures during this process is

shown to produce an error which increases with the dip of the joint. The two dimensional sample of opposing profiles is used in a new kinematic analysis of the joint shear stress-shear deformation behavior. Examples of applying these methods on the porphyritic granite joints are presented.

The unrolled opposing profiles were used in a numerical simulation of a direct shear test using Discontinuous Deformation Analysis. Results were compared to laboratory test results using core samples containing the same joints. The simulated dilatancy and shear stress-shear deformation curves were close to the laboratory curves in the case of a joint in porphyritic granite.

Approved by: Richard E. Goodman, Professor of Civil Engineering

Richard E Goodman — Signature

August 8, 1994 — Date

Dedicated to my parents, Bhekh and Rita, for whom this achievement is a reflection of their lifelong series of endeavors and accomplishments, and to my dear wife, Sumira, with whom I share this first attainment of our new life together

Table of Contents

LIST OF FIGURES

LIST OF TABLES

ACKNOWLEDGMENTS

Professor Richard E. Goodman gave me the opportunity to pursue the studies leading to this thesis. I learned many things from Professor Goodman while taking his classes, doing field work, consulting on projects, thinking through ideas, watching him sing at the opera and even playing tennis. I am deeply grateful for having been able to spend time with and learn from this wonderful man.

This thesis would not have been possible without the support provided by Dr. Kenzi Karasaki, of Lawrence Berkeley Laboratory. I am indebted to him for the opportunity to think freely during my research and for guidance whenever I needed it.

Professor Chikaosa Tanimoto of Kyoto University first introduced me to the Borehole Scanner System and gave me the opportunity to do my field work in Japan. Mr. Yoshitaka Matsumoto, the president of Core Corporation allowed me to use the Borehole Scanner System for my research. Mr. Osamu Murakami, Chief Engineer at Core Corporation, taught me all I know about the Borehole Scanner System. I am grateful to all of these individuals.

I have profited from many discussions with people at Berkeley, Kyoto and Tokyo during my research. Professors Tor Brekke, Neville Cook, Nick Sitar and Bill Deitrich have always been helpful whenever I went to talk to them. My colleagues at Berekely Te-Chih Ke, Eric Lindquist and Ed Medly were always willing to listen to and comment on my work as I progressed. I am particularly grateful to Te-Chih Ke for letting me use his DDA code and teaching me how to use it. Wes Bethel at LBL helped me in learning AVS. Kiyoshi Kishida at Kyoto University helped me on innumerable occasions during my stays in Kyoto. In

particular, I am thankful for the help I got from Kishida and his students Mr. Naoki, Mr. Nakanishi and Mr. Fujisaki in performing the laboratory direct shear tests at Kyoto. While at Core Corporation in Tokyo, I learnt field and laboratory aspects of the Borehole Scanner System from Mr. Nobohiro Miyawaki, Mr. Shimizu and Mr. Mishima.

My interest in doing this Ph.D. program started from my research into landslide risk analysis on hill roads in Nepal. I am thankful for that experience to my supervisor at that time Mr. Birendra Deoja and to the institution where I worked at the time - International Centre for Integrated Mountain Development in Nepal.

I deeply appreciate the support and encouragement of my family and friends during the time it took to complete this PhD program. This work would not have been possible without their contributions.

I am grateful to the Geological Engineering Foundation, The California Mining and Mineral Resources Research Institute, the Jane Lewis Fellowship, the Berkeley Civil Engineering Department, and the Parker Davis Trask Fellowship for providing financial assistance during my PhD program. This work was carried out under U.S. Department of Energy Contract No. DEAC03 - 76SF00098 for the Director, Office of Civilian Radioactive Waste Management, Office of External Relations, and was administered by the Nevada Operations Office, U.S. Department of Energy.

CHAPTER 1
INTRODUCTION

1.1 Joint characterization

Joints commonly render rock masses into discontinuous material with anisotropic, non-homogeneous, non-linear mechanical and hydraulic properties. Furthermore, the influence joints have on the mechanical and hydraulic behavior of the rockmass depends on a wide variety of specific joint characteristics. Detailed descriptions of such joint characteristics are given in Bieniawski (1989), Dershowitz and Einstein et. al. (1988) and Brekke and Howard (1972). These joint characteristics include origin mode, size, orientation, spacing, persistence, infilling, wall alteration and strength, aperture, surface roughness and intersections made with other joints. Mode of origin is a characteristic which refers to whether the joint developed as a tensile or shear fracture. Joint properties affected by the joint's surface roughness will reflect the mode of origin of the joint. The size of the joint in terms of a length or surface area can vary from millimeters to kilometers. Knowledge of the joint size is useful in determining the importance of a given joint for the scale of the problem being studied. Joint orientation and spacing define the geometric configuration of the joint system which is important in understanding the behavior of the overall rockmass. Joint persistence refers to the fraction of the total joint size not occupied by rock bridges. Persistence gives an idea of the deviation of joint behavior that may be expected from a joint with no rock bridges. Infilling is material deposited on the joint and often consists of clay minerals. Joint wall alteration occurs where fluid flow is present and can substantially alter the mechanical and hydraulic properties of the joint. Finally, the joint aperture is the distance separating opposing joint walls. Joint aperture and surface roughness

are fundamentally important for mechanical and hydraulic behavior as will be shown later.

Many studies have been done to study the relationships between joint characteristics and the mechanical and hydraulic behavior of joints or rock block systems defined by joints. The closure curve of opposing interlocking joint walls under normal compression has been found to be hyperbolic with initial aperture, joint wall rock strength and surface roughness being the main joint characteristics affecting closure behavior (Bandis et. al. 1983). Bandis et. al. (1983) also found the closure curve of dislocated joints to be best described by a semilogarithmic function. Patton (1966), Schneider (1976), and Barton and Choubey (1977) have investigated joint shear deformation behavior and found it to be controlled by the surface roughness, joint wall compressive strength and the residual friction angle of the joint wall. An alternate model of shear strength that also accounts for the strength of the joint asperities was presented by Ladanyi and Archambault (1970). Coupled hydromechanical behavior of joints can be studied using a modified form of Darcy's law where an equivalent smooth wall aperture is used instead of the true joint aperture (Makurat et. al., 1990). Bandis (1994) describes a model for estimating the equivalent smooth wall aperture assuming radial flow through one joint in an isolated borehole section during a pumping test. Barton et. al. (1985) describe a relationship between the equivalent smooth wall aperture, the true joint aperture and the Joint Roughness Coefficient. Barton (1974) describes the influence of joint infilling on shear deformation behavior in relation to two extreme cases: one where the infilling thickness is less than the roughness amplitude and the other where the infilling thickness is large enough to mask the effect of surface roughness during shear deformation. Barton and Bandis (1980) present results and recommendations from a study of the scale effects of joint characteristics on shear deformation

behavior. Construction of probabilistic three dimensional geometric models of the joint and rock block system based on joint orientation, trace lengths and spacings are described by Pointe (1994) and Dershowitz and Einstein et. al. (1988). The stability of a system of blocks delineated by joints has been rigorously shown by Block Theory to be controlled by joint orientation and strength (Goodman and Shi, 1985). The conclusions of Block Theory have also been validated through field studies (Hatzor, 1992). Long (1994) describes a technique to simulate fluid flow through fractured rock using a probabilistic characterization of the joint geometry. The basic relations that these various investigations have produced have made it possible to gain geologic insights. For instance, in structural geology studies, paleo stress field orientations and relative ages are inferred from regional joint orientations and cross-cutting relationships respectively (Suppe, 1985). Geomorphologic studies of erosion through cliff retreat and mass wasting involve considerations related to joint genesis, weathering and strength (Selby, 1982).

1.2 Methods of joint characterization

Accompanying the progress in understanding of the basic relationships between joint characteristics and mechanical and hydraulic joint behavior, have been improvements in methods of measuring and predicting the joint properties of concern. There are many complementary and competing techniques available for evaluating geometric, mechanical, fluid flow and geologic properties of joints. These methods can be broadly viewed as borehole based and surface based methods.

1.2.1 Borehole Methods

Geophysical well logging methods measure some property of the borehole wall which, directly or indirectly, is used to evaluate joint characteristics. Goodman (1976) and Telford et. al. (1990) provide detailed descriptions of these

methods, which are only listed here. Electrical resistivity surveys are used to identify fracture locations using the lower resistivities of altered joint walls. The dipmeter enables estimation of joint orientation from its record of electrical resistivity on four microresistivity pads separated by 90 degrees. Caliper logs show joint locations in terms of increased borehole diameter. Goodman (1989) describes the flat jack, hydraulic fracturing and overcoring techniques of stress measurement. Seismic tomography is used to identify fractured zones in the rockmass between boreholes using correlations between higher fracture density with lower seismic wave velocities and higher attenuation (Tanimoto et. al., 1994). Pump tests and tracer injection tests conducted over packed off segments of adjacent boreholes are used to evaluate joint connectivity, transmissivity and hydraulic conductivity (Lee, 1982). Logging of oriented core is used to estimate joint orientation. The joint walls obtained from core samples are used in direct shear tests and measurement of joint surface roughness.

The borehole televiewer produces an image of the acoustic reflectivity of the borehole wall. This device consists of an acoustic transmitter-reciever unit that follows a spiral path as it is pulled up the borehole. Since the amplitude of the reflected acoustic wave will be lower along parts of the spiral path that fall on joints, the joints show up as dark areas in the televiewer image. The televiewer image is used to calculate orientations, locations and spacings of joints. Zemanek et. al. (1970) provide a detailed description of the televiewer.

Several optical instruments have been used to study joints in boreholes. The borehole camera takes color pictures of overlapping segments of a borehole wall. The camera points down the borehole towards a conical mirror that deflects the light reflecting off the borehole wall. Interpretation of the image is done by analyzing either a cylindrical reconstruction of the borehole wall or a flat donut shaped projection of the borehole wall (Trantina, A. and Cluff, L.S., 1963). The

orientation and location of joints can be obtained from the borehole camera. The borehole TV system uses a video camera that points down the borehole at a mirror inclined at 45 degrees which deflects light reflected from the borehole wall to the video camera (Briggs, 1964). Unlike the conical mirror of the borehole camera, the mirror in the borehole TV receives light reflected off only a portion of the borehole circumference. Adjacent portions of the borehole circumference can be obtained by rotating the mirror. The orientation and location of joints can be measured from a mosaic of adjacent borehole TV images. Finally, a periscope device called a stratoscope (Cluff, 1966) can be used to view the borehole wall at depths of less than 70 feet. A camera can also be attached to the eyepiece of the stratoscope.

1.2.2 Surface Methods

Joints can be mapped by observation of natural exposures, surface excavations and tunnel walls. Alternatively, photographs may be used instead of manual joint mapping for convenience. In the case of regional joint studies and inaccessible areas, aerial photographs or satellite images may be the only alternatives. The data in maps or photographs are analyzed for joint set orientations (Goodman, 1976), joint spacing distributions and joint trace length distributions (Priest and Hudson, 1976). In the case of mechanical stability problems, keyblocks can be identified directly from the joint map as specific polygons formed by intersecting joints (Shi and Goodman,1989).

Joint strength can be measured by in-situ direct shear tests , laboratory direct shear and triaxial tests using joint samples from accessible surfaces (Goodman, 1976), push and pull tests (Barton et.al,1990), field and laboratory tilt tests (Barton and Choubey, 1977), induced wedge tests (Thapa and Goodman, 1994), measurement of joint surface roughness (Fecker and Rengers, 1971),

and field block sliding tests. Snow (1970) describes photographic techniques of aperture measurement.

1.3 Limitations of existing joint characterization methods

Even with the various capabilities acquired as a result of the advances in joint characterization described above, there remains a need for further development. Hudson (1994) has reviewed existing methods of joint characterization and finds many core sample based methods to be unsatisfactory, borehole camera based methods to be better and surface based methods to be mostly satisfactory. Given that many important joint and rockmass characterization tasks are done on sites where surface exposure is not available, there is at least a need for advances in borehole based joint characterization methods.

A major cause for the poor performance of core sample based methods is the disturbance of the sample caused during the drilling and recovery process. For instance, the use of oriented core for estimation of joint orientation can be misleading if the core recovery is poor (Goodman, 1976). Sample disturbance makes it difficult to assess in-situ properties such as infilling and wall strength. Weak material critical to the evaluation of rockmass properties in highly weathered or fault zones, are difficult to recover. Open joints may be damaged during overcoring and subsequent aperture measurements may not be accurate. Additionally, destressing effects make aperture measurements questionable, particularly when the measurements are made near the ground surface. Persistence is impossible to assess from a borehole and difficult to estimate from surface observations of trace lengths. Improvements in areas such as these can be expected to make significant improvements in understanding and predicting the mechanical and hydraulic behavior of joints and jointed rockmasses.

1.4 Objectives

Recently, a new instrument called the Borehole Scanner System (BSS) has become available. The BSS is an optical instrument that produces a digital unrolled image of the borehole wall. The BSS[1], and a similar instrument called the Borehole Image Processing System[2] (BIPS) provide significant advantages over the existing borehole imaging instruments described earlier. As will be shown later, the advantages presented by the BSS makes it possible to develop a number of new approaches to rock and joint characterization. The research in this thesis addresses particularly new approaches to the characterization of in-situ joint strength arising from surface roughness. A means of extracting the joint roughness profile from BSS image is examined first. Subsequently, profile analysis for strength characterization in terms of the dilation angle is developed for single and opposing profiles. Next a method for assessing the anisotropy of joint strength is developed. The final topic of this thesis is a numerical simulation of joint shear deformation behavior using DDA and comparison to laboratory results.

To provide data for the investigations of this thesis, BSS field measurements were made on two 3.5 inch diameter boreholes at an underground powerhouse site in Japan. Each borehole was about 70 meters long. Core samples from the boreholes were available for laboratory direct shear testing. The results of this thesis are not site specific and may be used on any site where similar quality BSS data can be collected. Also, although the work described in this thesis is based on the BSS, the results are general and can be used with either system.

---

[1]Developed by Core Corporation, 3-4-15-903 Mita, Minato-ku, Tokyo 108, Japan
[2]Developed by Raax Company, 1400 Hermann Drive, 4-C, Houston, TX 77004

The methods developed in this thesis were implemented in C language computer programs. Other than the programs for extracting the roughness profile, these programs are fully portable and can be run on any IBM compatible personal computer. The profile extraction routines are made to be a part of a larger image processing program.

CHAPTER 2

THE BOREHOLE SCANNER SYSTEM

2.1 Description of the BSS and Field Use

The BSS consists of a probe, depth encoder, winch, controller, TV monitor and a VTR unit as shown in Figure 2.1. The watertight probe houses a white light source and a magnetic compass[1] at the bottom . A mirror rotating at 3000 rpm sits directly above the lamp, and reflects light from the lamp onto the borehole wall through a glass window. The light reflected off the borehole wall is again reflected by another side of the same rotating mirror into a photoelectric transformer. The photoelectric transformer measures the intensity of the incoming light in the red, blue and green wavelength bands and converts the intensities into digital form. The digital data from the photoelectric transformer is passed to an azimuth gauge which marks the point in the data stream corresponding to north. The data then passes through an amplifier to the controller at the surface via a cable with a tensile strength of 900 lb/ft^2. The entire borehole wall is scanned along a spiral path in this manner as the winch lowers the probe.

The depth encoder at the top of the borehole records the depth at which the probe is scanning as the probe is lowered into the borehole. The minimum depth increment the encoder can detect is 0.1 mm at present. The controller receives the depth data from the depth encoder in addition to the oriented borehole wall reflectance data. The combined depth and reflectance data is stored on a digital tape. Subsequently, the data are also recorded on a video

---

[1] The magnetic compass is currently being replaced by a gyroscope to avoid problems in magnetic rocks.

tape and displayed as a scrolling unrolled image of the borehole wall on a TV monitor.

The BSS can be used to scan boreholes with diameters ranging from 66 mm to 150 mm. Currently, the BSS can be used to scan boreholes upto 1000 m. deep at a maximum rate of 72 meters per hour. The inclination of the boreholes may range from vertical to sub-vertical to horizontal. At present, any water in the borehole must be clear[2].

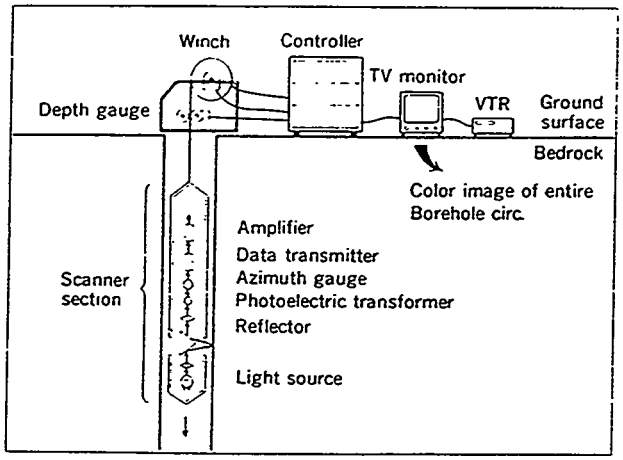

Figure 2.1: Schematic of the BSS

Prior to scanning, boreholes are flushed with clear water for about 48 hours and left undisturbed for about 24 hours to allow suspended particles to settle. This may not be possible in unstable terrain such as a landslide zone. In such cases, scanning is done immediately after drilling a few meters. The borehole is then cased and the drilling and scanning sequence repeated over successive depth intervals. In the case of horizontal or near horizontal boreholes, the scanner is first inserted into the borehole encased in a polythene pipe with just the scanning window of the probe protruding from the end of the pipe. The pipe is pulled back out as the winch pulls the probe back during the

[2] The manufacturer of the BSS, Core Corp., is planning to make another version of the equipment with an infrared light source. This change is expected to make it possible to scan boreholes with muddy water.

scanning. Use of the polythene pipe in this manner has an added advantage of protecting the scanner in case of borehole collapse. The disadvantage in using a pipe is the irregularity in the scanning path caused by occasional departures from a steady withdrawal rate of the pipe.

It is convenient to have access to the site by van since the winch and generator are difficult to carry long distances by hand. On difficult slopes, a crane may be needed to lower the winch and generator to the borehole. Two people are usually sufficient to perform the scanning on vertical boreholes--more people are needed to assist in the case of horizontal boreholes. The TV monitor is always watched during scanning to enable quick response in case of a borehole collapse.

2.2 Description of BSS Data

One complete revolution of the probe's mirror picks up reflectance from all of the contiguous segments on the borehole wall at the same depth. The contiguous segments along the periphery of the borehole wall are discretized into a line of 1000 data points covering reflectance from equal angular intervals. A data point in each such line is a three dimensional vector defining the reflectance intensity, on a scale of 0 to 255, in the red, green and blue (RGB) wavelength bands. The location of the borehole wall segment represented by each such point is defined by the depth at which the point was scanned and the rotation sequence number (1-1000), which specifies the azimuth of the data point with respect to north. Thus the entire borehole wall is represented by lines of RGB data points at successive depths. A true color unrolled image of the borehole wall can be obtained by combining the RGB components of each data point on a computer. Each data point is represented by one pixel on a computer display of the borehole wall. Figure 2.2 shows a typical image obtained from BSS data by this process.

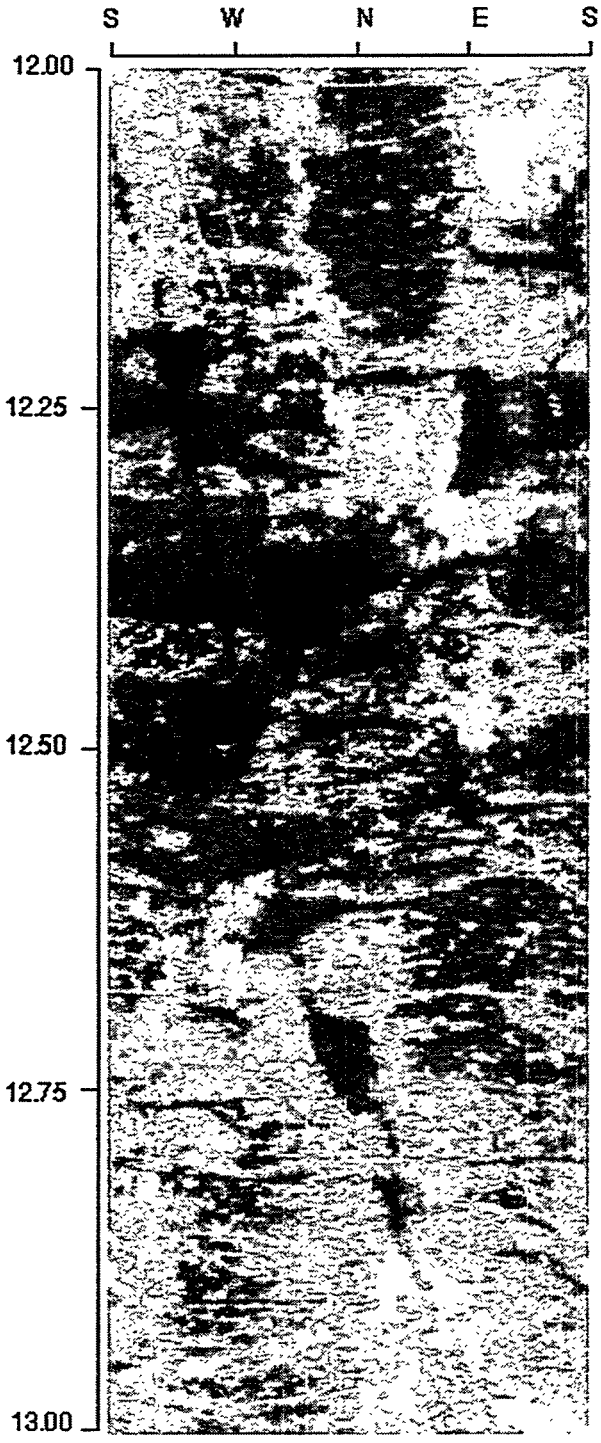

Figure 2.2: Unrolled image of borehole wall

The vertical resolution of the BSS data depends on the rate at which the probe is lowered into the borehole. This rate can be controlled from the winch. The maximum vertical resolution of 0.1 mm requires a slow lowering rate while a faster rate may be more desirable if fine detail is not important. The resolution along the periphery of the borehole wall depends on the borehole size. An 89 mm diameter borehole will have a horizontal resolution of 0.28 mm.

With three numbers assigned to each data point at high resolution, the BSS produces a large volume of data. To facilitate data manipulation, only 500 of the available 1000 horizontal points are transferred to the data analysis computer system. In this form, one meter of BSS data typically requires about 3 MB of storage space. A rewriteable magnetic-optical disk with a capacity of about 300 MB per side is used for BSS data storage and manipulation on a personal computer.

2.3 Advantages of the BSS

The BSS offers advantages over existing borehole wall imaging techniques and presents new opportunities to analyze rock mass properties in-situ.

2.3.1 Advantages over existing imaging methods

The horizontal view of the borehole wall produced by the BSS is easier to analyze and visualize than the conically projected view produced by the borehole camera. The BSS shares this advantage over the borehole camera with the borehole TV and televiewer. Unlike the borehole TV however, the scanning mode of operation utilized by the BSS and the televiewer results in far more efficient data collection. While the BSS scanning gathers an unrolled image of the borehole wall at a rate of 72 meters per hour, the borehole TV works at a rate of 1-2 meters per hour. This is because the borehole TV has to be manually rotated through successive 40 degree intervals at each depth increment.

Furthermore, while the unrolled image of the borehole wall collected by the BSS is displayed in real time, the borehole TV images of segments of the borehole wall have to be manually spliced together afterwards.

The BSS has several advantages over the televiewer. First, the optical reflectance mapped by the BSS produces an image with more geologic information, since the BSS captures lithological and fracture details, while the acoustic reflectance from the televiewer provides no lithologic data. Next, the resolution of the televiewer is considerably poorer than optical tools because the wavelength of sound used in the televiewer is about 1000 times larger than the wavelength of visible light (Zemanek et. al., 1970). Zemanek et. al. (1970) estimate that the televiewer will have a resolution of 0.79 mm under ideal borehole conditions. Barton (1988) reports a typical resolution of the televiewer to be a few millimeters horizontally and one centimeter vertically in a 12 inch borehole. The BSS would produce data with a horizontal resolution of 0.95 mm and vertical resolution of 0.1 mm from the same 12 inch borehole. Unlike the televiewer whose operation requires the borehole to be filled with some fluid, the BSS will work in gas filled boreholes. This difference between the two instruments is important for non-vertical boreholes. An advantage of the televiewer is that the fluid in the borehole need not be clear as long as it is homogeneous. However, the quality and resolution of the televiewer image is reduced when operating in drilling mud.

The availability of the BSS data in digital format provides flexibility for data manipulation and analysis on a computer. This feature of BSS data is a significant improvement over televiewer logs which are usually constructed from Polaroid photographs of successive displays of acoustic reflectivity on a oscilloscope screen. A system to digitize such televiewer logs has recently been developed by Barton (1988).

2.3.2 New possibilities for in-situ characterization

The availability of the high resolution true color digital BSS data for computer based analysis makes it feasible to extract several in-situ rock properties for the first time. The BSS data also increases the efficiency at which joint orientations and apertures can be measured compared with other methods. Tanimoto et. al. (1992) describe how the BSS data can be analyzed for joint orientations and apertures at a rate of 10 - 50 meters a day compared to 1 - 2 meters a day in the case of borehole TV data.

The texture of the rock sampled by the BSS image can be quantified using a number of parameters. Fabbri (1984) describes image processing techniques applied to thin section images to measure grain size distributions, interparticle distances, grain circumference, cross-sectional areas of grains, grain orientations and porosity. Although BSS images do not have the resolution of thin section images, similar image processing and interpretation techniques can be developed for analyzing the borehole wall texture. Parameters describing larger textural features of interest can also be measured. Tang and Quek (1986) describe a Bayesian method for estimating boulder size distributions and volumetric proportions from borehole logs for construction planning. A similar approach can be used with BSS data to estimate these parameters. These boulder parameters are also of interest to geomorpologists studying the size and occurrence time of paleo floods. Recent work (Lindquist, 1994) shows the strength of melange is a function of the volumetric proportion occupied by blocks. As with the boulders, the BSS data can be used to estimate the proportion of blocks in a melange rockmass.

The three dimensional vector defining the color of each pixel in the BSS image makes it possible to identify regions of special interest. One example of such a region is a mineral grain or group of minerals. Feldspar for instance, may

have RGB reflectance intensities in the ranges 245-250, 250-255 and 240-255 respectively. A computer program can locate all feldspar crystals by isolating all pixels having RGB values in that range. More generally, a region growing image processing algorithm can be used to find all regions in the image having the same RGB values as a region defined by the user with a mouse. This approach to mineral identification requires user RGB value specification of the mineral of interest by observation of the BSS image and comparison with core samples when possible. A more general approach would utilize a predetermined library (Hunt and Salisbury, 1970) of the spectral reflectance characteristics of minerals. However, such spectral signatures used to uniquely identify minerals and rocks (Siegal and Gullipse, 1980) require many bands of reflectance data in the visible and near-infrared wavelengths. The currently available BSS does not provide such data. In addition to the petrologic analysis that would be made possible by mineralogy identification, knowledge of the minerals on joint walls would provide information on the basic friction angle of the joints intersected by the borehole.

Another region of interest in the BSS image is a weathering zone near the surface, fault or a joint. The RGB characteristics of a known conductive joint can be used in a region growing program to locate other possibly conducting joints in the same rocktype assuming joint wall alteration will be similar. Joints that are potentially troublesome from a mechanical point of view, such as those coated with chlorite and serpentinite or those filled with swelling clay, can also be located using a reference joint.

Statistical simulations of rockmass jointing are important for mechanical and fluid flow problems (Einstein, 1993). Such simulations typically involve numerous assumptions regarding distribution types, joint shapes and joint extents. The unrolled BSS borehole image provides a way to verify, update or calibrate the simulation model assumptions and parameters. For example, the

persistence of joints may be estimated through a trial and error process of assuming a set of values, making predictions for an adjacent borehole, comparing the prediction to the BSS data in that borehole and revising the assumed prediction so as to reduce discrepancies. BSS data from a reference borehole may be used to obtain the other parameters of the jointing model. The goodness of fit of a given simulation to the BSS data may be judged by the percentage of pixels in the simulation that are the same as in the BSS data.

Edge extraction image processing techniques can be applied to the BSS image to find the roughness profile of joints. The roughness profile is a fundamental joint feature and can be analyzed for a number of parameters. One such parameter is the joint dilation angle. The joint shear strength is completely defined by the dilation angle and the basic friction angle referred to earlier. The opposing in-situ joint profiles obtainable from the BSS data makes it possible to extend the existing method of deriving the dilation angle from roughness profiles which is applicable to perfectly mated joints only. Once dilation angles have been found for all joints in the various boreholes at a site, a spatial analysis of the variation of strength on different joint sets may be performed. For example, contours of joint strength would provide a quick way to assess weak zones.

The dilation angle derived from BSS data can be analyzed for anisotropy. Strength anisotropy can have a significant influence on deformations in jointed rock where block geometry constrains movement to certain kinematically feasible directions only. The BSS data provides the first opportunity to study this parameter in-situ.

After obtaining roughness profiles of opposing walls of a joint, the aperture along the entire joint sample can be obtained as the width of the opening separating the two sides. Aperture distributions can be compiled for various joint sets in this way. The data also enables a study of the relationship

between joint roughness and aperture, which may be of interest in fluid flow research. Additionally, the correlation of roughness profiles on opposing sides may be studied in-situ just as it is done using core samples (Brown, et. al. 1986).

Parts or all of the opposing joint roughness profiles can be unrolled into a two dimensional sample of the joint surface. The unrolled samples can then be used to simulate a laboratory direct shear test using a method such as Discontinuous Deformation Analysis (DDA) (Shi,1985). In-situ shear deformation characteristics of the joints can be studied in this way.

Fourier transforms of in-situ joint roughness profiles may yield important information regarding joint genesis and subsequent alteration. Comparison of the power spectra of the roughness profile with the power spectra of the image of the joint wall can be used to see if the roughness profile reflects the grain size distribution of the rock wall. For instance, the power spectra of a sandstone joint wall composed of the same grain size would show a peak at the wavelength corresponding to the grain size. The power spectra of a purely tensile joint in this rock would also show a peak at the wavelength corresponding to the grain size. On the other hand, if joint alteration had significantly altered the roughness profile of the joint subsequent to its genesis, the power spectra of the roughness profile would show different peaks.

The fourier transform of the joint roughness profile can be used for other purposes as well. The slope of the power spectra can be used to estimate the fractal dimension of the joint surface roughness (Brown et. al. 1985). Subsequently, the fractal dimension can be used to simulate three dimensional models of the opposing joint surfaces. The fractal dimension or the moment (Tanimoto, et. al. 1994) may also be used to correlate joints across boreholes or to make joint membership assignments together with orientation. Tanimoto et. al. (1994) also show that the moment of the power spectra shows a strong

correlation to the Joint Roughness Coefficient (JRC) (Barton and Choubey, 1977). Utilizing this correlation, the BSS data can be used to estimate in-situ JRC values.

The BSS data may also be used for deformation analysis. Borchers et. al. (1993) report an analysis of fault offset made using BIPS data. Deformation analysis using BSS data may be very helpful in identifying the mode of failure in certain cases. For example, Ke et. al. (1994) describe a slope where it was difficult to decide if failure was occurring by sliding or toppling. Identification of a wedge shaped aperture distributions on tensile cracks would strongly suggest a toppling failure in this case. BSS data may also be useful in structural geology strain analysis to compile regional deformation patterns. Such assessments of regional deformation are used to interpret crustal movement and tectonic evolution (Ramsay and Huber, 1983).

CHAPTER 3
ROUGHNESS PROFILE EXTRACTION

3.1 Hardware and Software

The personal computer (PC) and graphics workstation as well as the software on them used in the roughness extraction process are described in this section.

3.1.1 PC environment

A specially configured PC with two screens, a special graphics adapter board, an external magnteo-optical (MO) disk drive and an external 8 mm tape drive is used to process the raw BSS data stored on a 8mm digital tape by the controller during field operation. All of the software used to process the BSS data with the PC was developed by Core Corp. Preprocessor utilities are used to transfer the raw data from digital tapes to rewritable MO disks. The data transfer utilities divide the raw data into files containing the data for successive one meter intervals. From the original data, which has 1000 pixels on each scanline, the data transfer utilities produce three files with 500, 100 and 10 pixels per scanline for every meter interval. This reduction of the raw data is done to suit the needs of the main analysis program and may be bypassed if desired.

The main analysis program, called Expert, reads the three files for each meter of the borehole and produces three types of displays of the unrolled borehole wall. The 10 pixel wide file is used to display the entire borehole so the user can select an interval of interest for more detailed analysis. The 50 pixel wide file is used to display a more detailed view of the meter of interest for user selection of a portion of the image within the meter for detailed analysis. Finally, the 500 pixel wide file is used for a detailed display from which the user interactively analyzes joint orientation and aperture. The joint orientation routine

simulates a sine curve using three user defined points lying on the joint. Another routine calculates an average aperture from the vertical distance between pairs of user defined points on the upper and lower joint walls. Expert also has several image processing routines that can be used to produce monochrome displays and RGB histograms, filter out noise and enhance the image. One example of how these image processing features can be used is the correction made on unusually dark images to uniformly increase brightness. A rotating cylindrical view of the borehole wall may also be seen using Expert.

Postprocessor routines are used to produce hardcopies of the BSS data and joint analysis results on a color laser printer with a 500 dpi capability. The results of joint analysis printed out are a joint trace map of the borehole wall, rose diagram of joint orientations and an equal area contour plot of joint densities. The trace map gives the strike and dip of joints, an average aperture for each joint and comments about the joint type.

For this thesis, the Expert program was used only to analyze joint orientations. Expert does not have the image processing tools needed to extract the roughness profile. Further development of Expert for roughness profile extraction on the PC was inconvenient since the PC works in Japanese, and is incompatible with the IBM PC. The 500 pixel wide data files were transferred to a graphics workstation for further analysis. It would have been desirable to work with the 1000 pixel files but these were not available at the time the work was done. However, the methods developed in this thesis are independent of the file size and future work can utilize 1000 pixel files.

3.1.2 AVS on a Graphics Workstation

The 500 pixel wide BSS data files were transferred from the NEC PC MO disk to the disk drive of a graphics workstation through a network file transfer utility. A utility program was written to convert the BSS data to a format readable

by a program called Application Visualization System (AVS). AVS[1] is a general purpose image processing and graphic visualization program. AVS was selected for use because it has a large library of image processing and three dimensional geometrical visualization modules. Also, AVS allows users to write their own modules, if the AVS library is not sufficient. A visual programming feature, called the network editor, in AVS makes it possible for the user to combine self-written and library modules to produce networks designed for specific tasks.

The AVS library modules were not sufficient to extract joint roughness profiles. Thus, additional custom modules had to be written and combined with the AVS modules to implement the thresholding edge extraction method described below. However, for geometric visualization of a cylindrical projection of the BSS image, the AVS modules were more than adequate. AVS allows the user to view such projections from any angle and to view plane slices made through the projection.

3.2 Review of edge extraction image processing techniques

Digital image processing methods are used to enhance images for human perception and to analyze scenes for autonomous machine perception (Gonzalez and Woods, 1992). These methods have found applications in medicine, geography, archeology, physics, astronomy, biology, nuclear medicine, law enforcement and defense. Only a small subset of these methods relating to edge extraction is of interest in defining the roughness profile of joints. They are described below.

3.2.1 General concepts

In image analysis, segmentation methods are used to extract edges and other features of interest from an image. These methods divide the image into

---

[1] Produced by Advanced Visual Systems, Inc., 300 Fifth Ave., Waltham, MA 02154

constituent segments based on two properties of intensity values: discontinuity and similarity (Gonzalez and Woods, 1992).

In monochrome images, a discontinuity can be detected based on a sharp change in gray-level intensity. Figure 3.1 illustrates one way of detecting such a discontinuity using derivative operators. In Figure 3.1, the location of discontinuities separating the light stripe from the dark background, and visa versa, are graphically represented by intensity changes and maxima and minima of the first and second derivatives of the intensity function. The intensity is shown to change smoothly between the light and dark stripes because digital images are slightly blurred from sampling (Gonzalez and Woods, 1992). The gray-level or intensity in monochrome images ranges from 0 (black) to 255 (white).

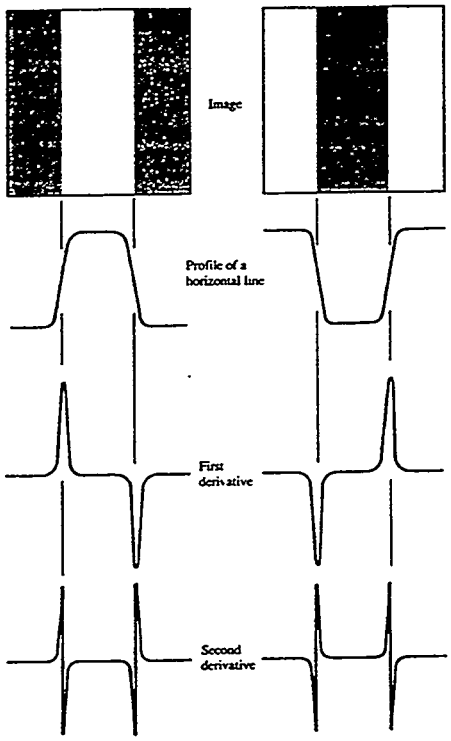

Figure 3.1: Discontinuity detection in images (after Gonzalez and Woods, 1992)

Similarity of gray-level intensities of a given feature in a monochrome images is the other major image property used in segmentation. Figure 3.2 shows a histogram of gray-level values for an image where the feature and background occupy two distinct ranges of intensity separated by a threshold value of T. In this case, the threshold value of T can be used to segment the image into the feature of interest and the background.

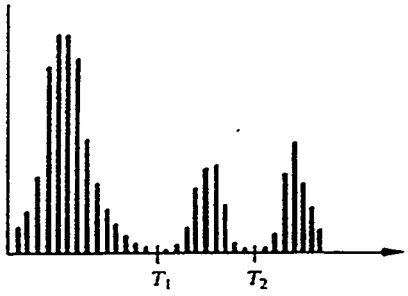

Figure 3.2: Segmentation using thresholding (after Gonzalez and Woods, 1992)

3.2.2 Thresholding method of profile extraction

All of the profile extraction processing is done on a monochrome transform of the BSS image. The roughness profile is extracted from the BSS image in four steps. The first step involves thresholding of the original image f(x,y) between two thresholds T_1 and T_2 to produce a binary image g(x,y) such that

$$g(x,y) = \begin{cases} 255 \text{ if } T_1 < f(x,y) \le T_2 \\ 0 \quad \text{otherwise} \end{cases} \qquad (3.1)$$

In Eqn. (3.1), the coordinates (x,y) refer to the row and column number of each pixel. The thresholds T_1 and T_2 are chosen so that in the binary image g(x,y), all pixels falling inside the joint aperture are white while the pixels outside the aperture on the rock wall, are black. To accomplish this segmentation, the selection of T_1 and T_2 has to be made so as to cover only the dark range of intensities of the pixels in the aperture region between opposing joint walls. T_1

and T_2 can be determined from a histogram of the image intensities (as in Figure 3.2) or by probing the image with a mouse on a screen display of the image. The value of T_1 can usually be set to zero. Figure 3.3 illustrates the application of the thresholding operation on a monochrome image.

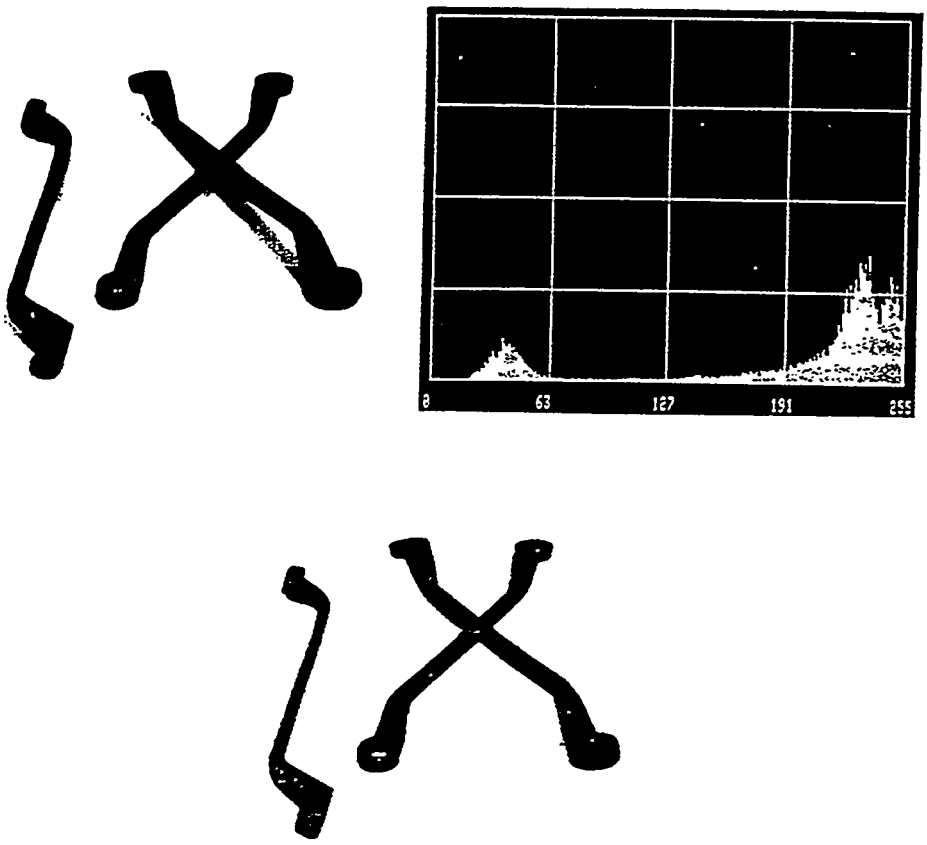

Figure 3.3: Illustration of thresholding (after Gonzalez and Woods, 1992)

After obtaining the binary image g(x,y), the pixels on the roughness profile are isolated by detecting the discontinuity separating the rock wall from the joint aperture region. No differential operators are needed to detect the discontinuity in the binary image. Instead, the roughness profile pixels are isolated by using

the fact that only pixels on the profile and pixels in the aperture region will have at least one white adjacent pixel in the binary image. The pixels on the profile and those in the aperture region can be further distinguished by the fact the profile pixels in the binary image will be black while the pixels in the aperture region will be white. Only the pixels on the rock wall qualify as points on the roughness profile. These rules are applied on the binary image g(x,y) to produce another binary image h(x,y) in which pixels on the roughness profile have an intensity of zero and all other pixels have intensities of 255.

The next step involves using a pixel connectivity routine to produce an ASCII file listing of consecutive roughness profile pixel image coordinates. The connectivity routine begins at the first pixel on the profile and searches for the next pixel on the profile until no further connected pixels can be found. The center pixel in the 3X3 pixel box of Figure 3.4 is a pixel on the roughness profile and the adjacent pixels are candidate consecutive profile points. The numbers in the adjacent cells identify the cell. The search sequence for the upper profile is 2,3,6,8,9 and the search sequence for the lower profile is 8,9,6,3,2. The first adjacent pixel with an intensity of zero is identified as the next profile point. That point then becomes the center pixel in Figure 3.4 and the search is repeated.

1	2	3
4	X,Y	6
7	8	9

Figure 3.4: Pixel connectivity search sequence

The final step in the profile extraction procedure is a transformation of coordinates. The ASCII file produced by the connectivity routine contains profile points in AVS (x,y) image coordinates. A utility program was written to substitute

borehole coordinates of rotation number and depth for the image coordinates by comparison to the original BSS image.

3.3 Implementation of the Thresholding method in AVS

The thresholding method described above was implemented in three AVS networks. These networks and examples of their use on BSS data are presented below. All three networks are used on a single joint in succession. An image of the example joint prior to analysis is shown in Figure 3.6.

3.3.1 Threshold network

The thresholding operation only works on images where there is a clear and constant intensity threshold separating the joint wall and aperture region. Initial attempts to use the thresholding operation on the entire joint were unsuccessful because the upper threshold limit was not constant over the entire joint. The upper threshold limit is only constant over small regions of the joint where the aperture and lighting are more or less uniform. This situation made it necessary to implement the thresholding operation in a way that allowed the user to work over small regions of the joint and compile the results at the end.

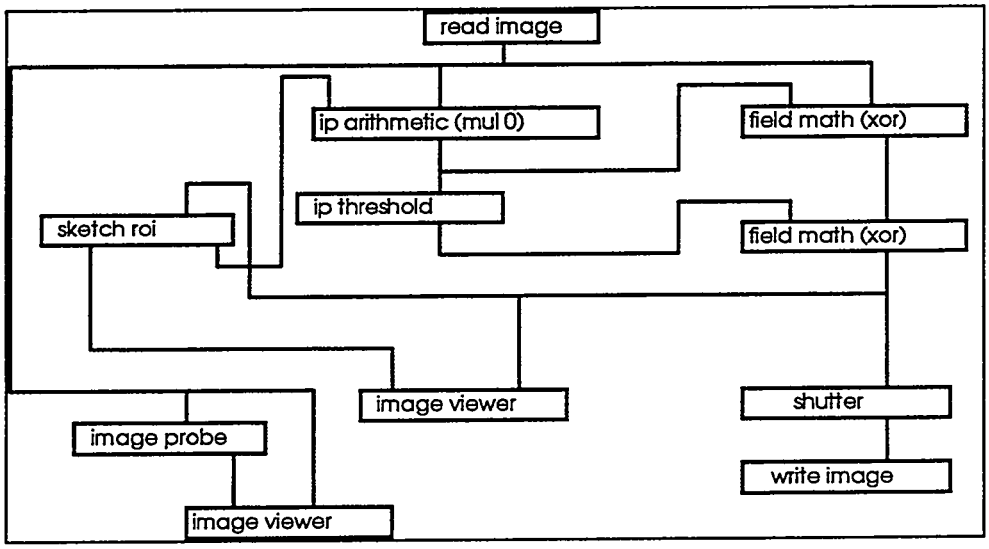

Figure 3.5: Threshold AVS network

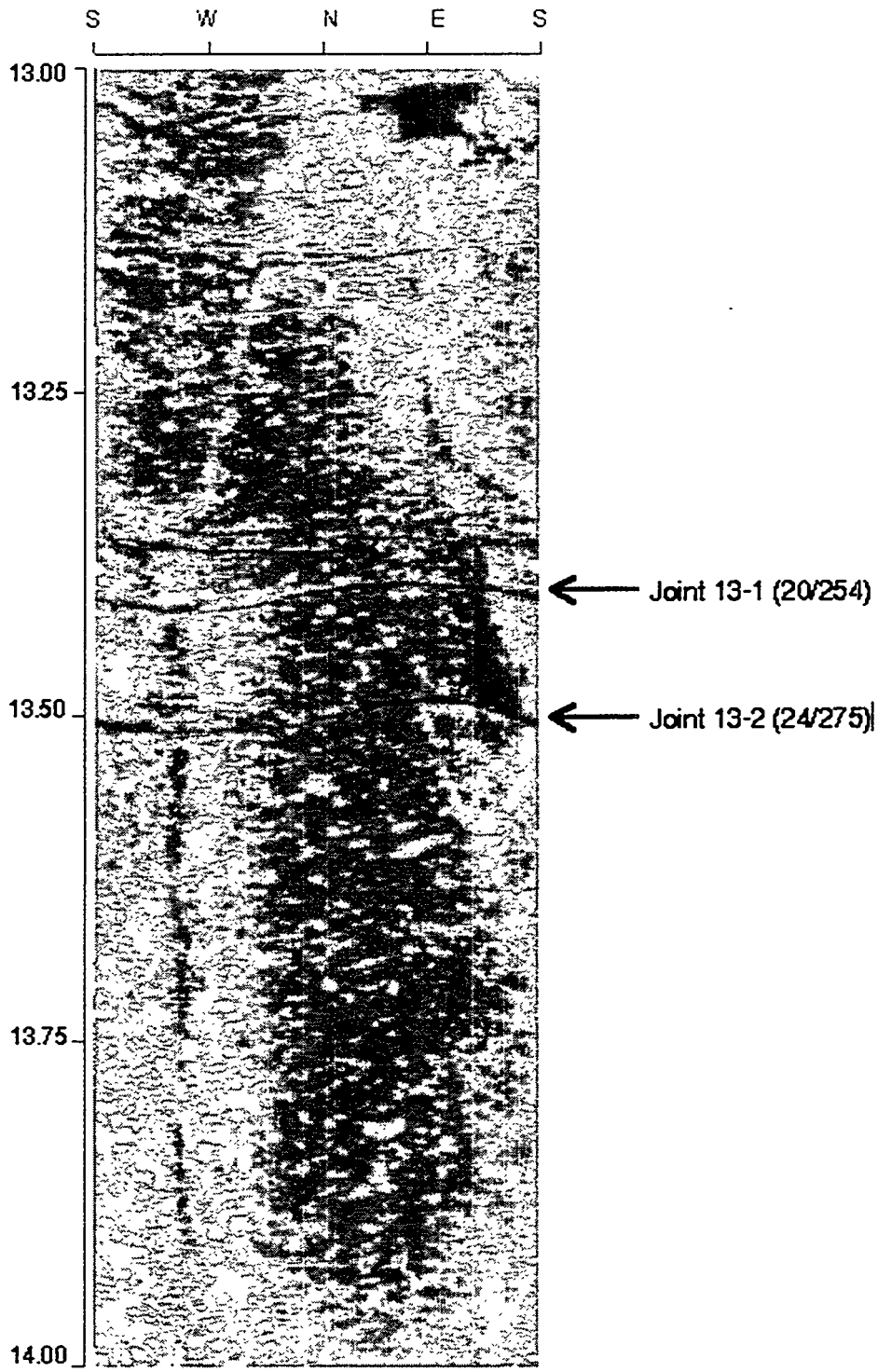

Figure 3.6: Original image showing joint 13-1

The threshold network flow diagram implemented in AVS is shown in Figure 3.5. The network first reads the BSS image file and displays it in a window. The user can magnify the displayed image to get a closer look at the joint. The 'image probe' module allows the user to see the intensity of any pixel selected by the mouse and thereby identify a region with a constant upper threshold limit. Next, the 'sketch roi' module allows the user to define a Region Of Interest (ROI) using the mouse. Once the ROI has been defined, Eqn. (3.1) is used as coded in the 'ip threshold' module to analyze that region, and a binary image, g(x,y), of the ROI is saved on a disk file. The entire joint is covered by repeating this procedure in as many ROI's as needed.

3.3.2 Edge locator network

The edge locator network operates on the binary ROI produced by the threshold network. The binary ROI from the threshold network is directly fed to the edge locator network so that the ROI does not have to be redefined. Figure 3.7 shows the edge locator network.

The 'edge locator' module shown in Figure 3.7 is not an AVS module. The code written for 'edge locator' scans through the ROI and applies the rules described earlier for isolating roughness profile pixels. The resulting roughness profile is exactly one pixel thick. The 'sketch roi' and associated modules in the edge locator network are used only if the ROI has to be redefined. The result of applying the edge locator network to joint 13-1 is shown in Figure 3.8. The roughness profile pixels in Figure 3.8 have been overlain on the original BSS image.

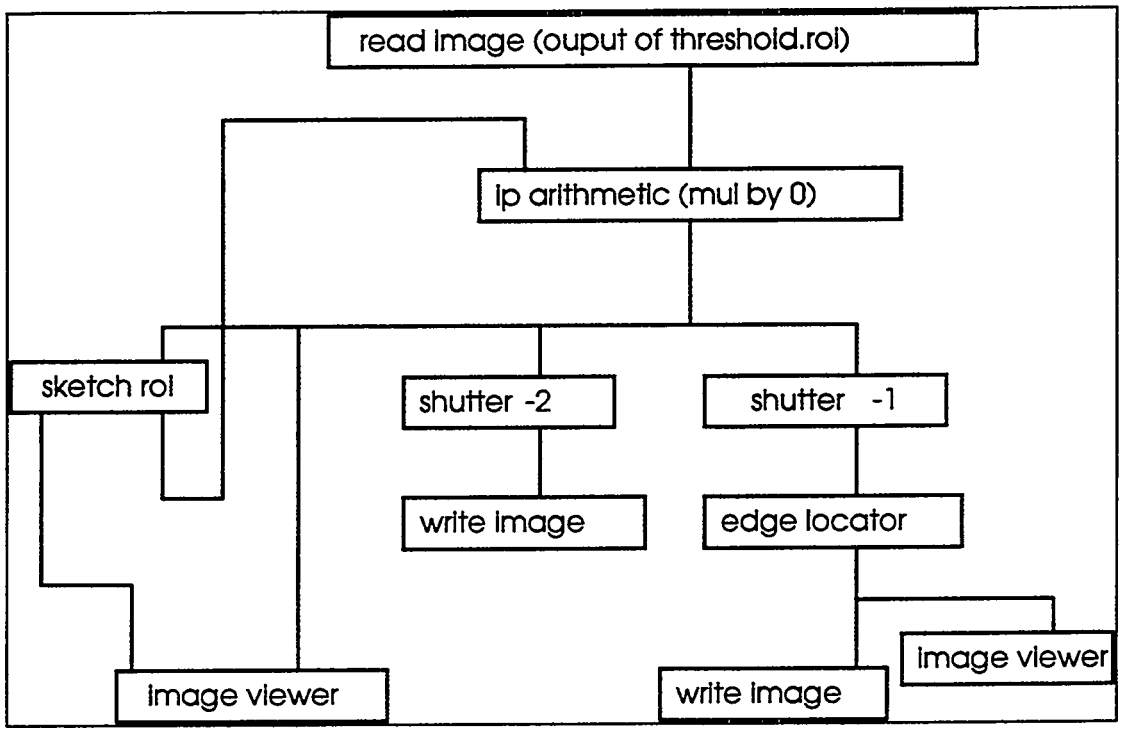

Figure 3.7: Edge locator network

3.3.3 Profiler network

The 'get profile' module of the profiler network was written to implement the pixel connectivity search pattern shown in Figure 3.4. The user defines the coordinates of the first pixel on either the upper or lower profile. Those coordinates can be found by using the 'image probe' module. The upper and lower profiles are processed independently and the user must specify which profile is being analyzed. Figure 3.9 shows the profiler network. Table 3.1 shows a partial listing of the image coordinates of profile points for joint 13-1. The full list contains 550 points and is listed in Appendix A.

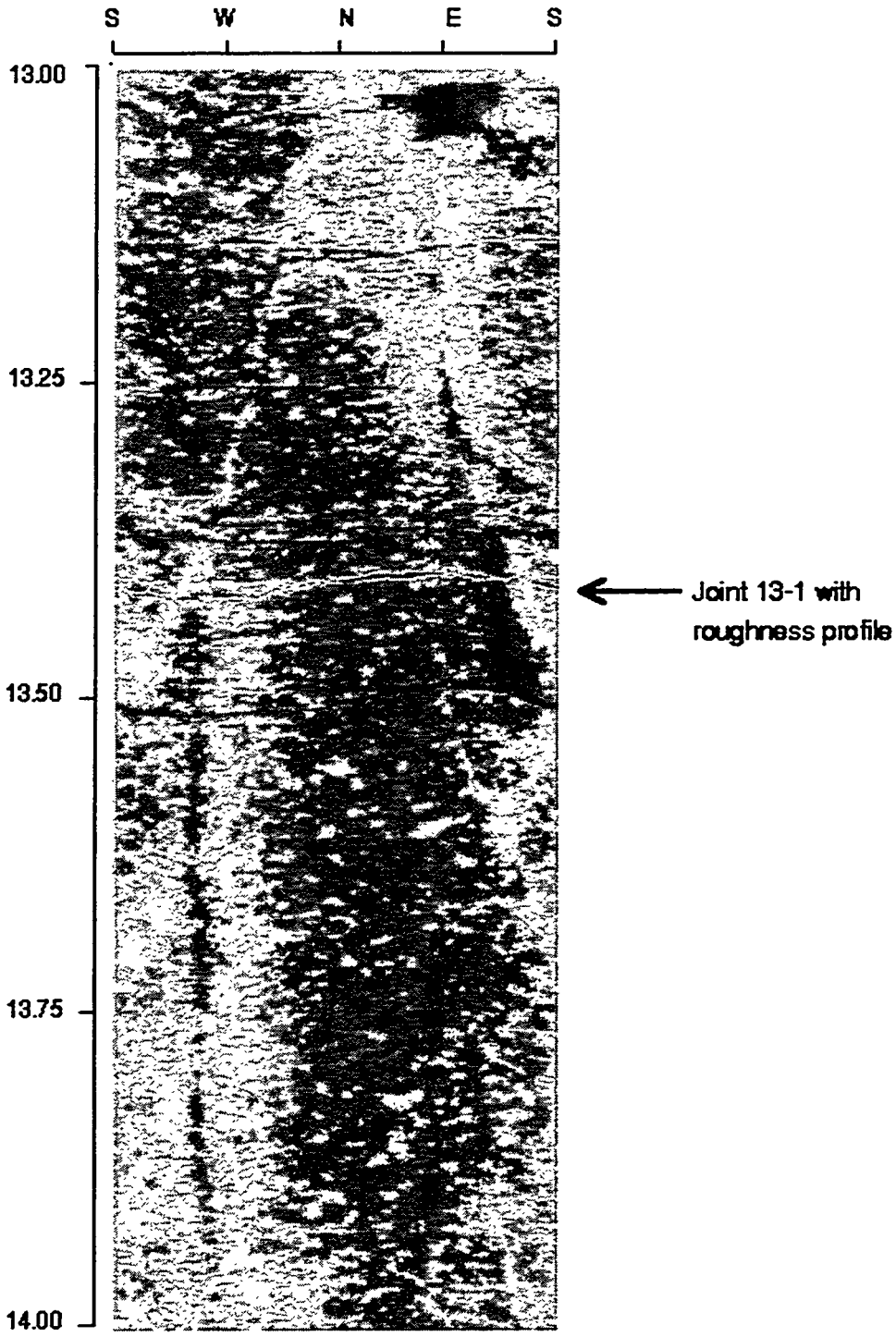

Figure 3.8: Overlay of joint 13-1 roughness profile on unrolled image of borehole wall

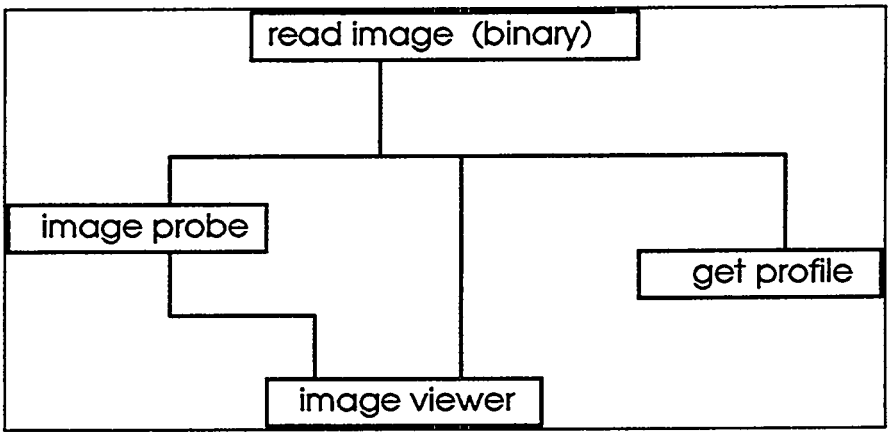

Figure 3.9: Profiler network

3.3.4 Coordinate transforms

AVS is not needed once the ASCII file containing roughness profile image coordinates has been obtained from the profiler network. The last step in the profile extraction procedure is the coordinate transform discussed earlier. Once the image coordinates have been converted to borehole coordinates of rotation number and depth, the rotation number is further converted into an azimuth. The conversion to azimuth is done by linear interpolation between rotation numbers whose azimuths are known from the BSS data recording format. The linear interpolation is justified because the rotation rate of the BSS probe's mirror is uniform as it scans each line of the borehole wall. The roughness profile pixel borehole coordinates are partially listed in Table 3.1. As with the image coordinates, a full listing is given in Appendix A.

Table 3.1: Partial list of roughness profile for joint 13-1

Upper profile of joint 13-1				Lower profile of joint 13-1			
rotation data	depth data in image y	azimuth by global_c	depth data in mm	rotation data	depth data in image y	azimuth by global_c	depth data in mm
1	650	180.72	13428.25	1	655	180.72	13434.5
2	650	181.44	13428.25	2	655	181.44	13434.5
3	650	182.16	13428.25	3	656	182.16	13432.25
4	650	182.88001	13428.25	4	656	182.88001	13432.25
4	651	182.88001	13430.25	4	655	182.88001	13434.5
5	651	183.60001	13430.25	5	655	183.60001	13434.5
6	651	184.32001	13430.25	6	655	184.32001	13434.5
7	651	185.03999	13430.25	7	655	185.03999	13434.5
7	652	185.03999	13430.75	8	655	185.76	13434.5
8	652	185.76	13430.75	9	655	186.48	13434.5
8	653	185.76	13433	10	655	187.2	13434.5
9	653	186.48	13433	11	656	187.92	13432.25
10	653	187.2	13433	12	656	188.64	13432.25
11	653	187.92	13433	13	657	189.36	13434.5
11	654	187.92	13432.25	14	657	190.08	13434.5
12	654	188.64	13432.25	15	657	190.8	13434.5
13	654	189.36	13432.25	16	658	191.52	13433.5
13	655	189.36	13434.5	17	659	192.24001	13434
14	655	190.08	13434.5	18	660	192.96001	13436
14	656	190.08	13432.25	18	661	192.96001	13436.75
15	656	190.8	13432.25	19	662	193.67999	13436
16	656	191.52	13432.25	20	663	194.39999	13435.25
17	656	192.24001	13432.25	21	664	195.12	13435.75
17	657	192.24001	13434.5	22	664	195.84	13435.75
18	657	192.96001	13434.5	23	664	196.56	13435.75
19	657	193.67999	13434.5	24	664	197.28	13435.75
20	657	194.39999	13434.5	25	664	198	13435.75

CHAPTER 4

ANALYSIS FOR IN-SITU MECHANICAL JOINT PROPERTIES

4.1 Overview

In-situ joint profiles obtained from BSS images may be analyzed for a number of mechanical joint properties. Analyses developed for estimating in-situ joint dilation angles and shear strength are described in this chapter. Considerations related to joint aperture estimation that grew out of the work on mechanical properties are also described.

The BSS data used in developing and testing the methods described in this thesis were collected from two vertical boreholes 3-5 and 4-1 at a site of a proposed underground powerhouse in the central part of Honshu Island in Japan. The two boreholes are located in an exploratory adit situated 70 meters beneath a steep valley where the basement rocks are porphyritic granite, rhyolite and slate. The site was subjected to late Cretaceous volcanic movement and contains many steeply dipping joints with high joint frequency and wide apertures (Tanimoto et. al, 1994).

A total of 30 joints from borehole 3-5 and 2 joints from borehole 4-1 were used in this thesis. Unrolled images of the parts of boreholes 3-5 and 4-1 containing these joints are presented in Appendix B. The joints will be referred to by the identification labels shown in the images of Appendix B. Unfortunately, the scanning rate used at the site was not optimal and as a result the vertical resolution of the BSS data is only 0.5 mm. The scanner version used at the time of the scanning had a maximum vertical resolution of 0.25 mm. The horizontal resolution of the data is 0.56 mm. This too could have been improved to 0.25 mm had the 1000 pixel format data been available. All joints from borehole 3-5 were in porphyritic granite and all joints in borehole 4-1 were in rhyolite.

Opposing roughness profiles were extracted from all joints using the method discussed in Chapter 3.

4.2 Joint Dilatancy and Renger's envelope

Following a review of the role of joint roughness in shear strength, a method of analyzing the BSS data for the joint dilation angle is presented in this section.

4.2.1 Background

The peak shear strength of joints, τ , is a stress dependent property that is controlled by joint surface friction and dilation. Additionally, the shear strength may be influenced by rotation and rolling effects on the joint surface, cementation (Goodman, 1976) and rock bridges. Patton (1966) expressed joint shear strength by

$$\begin{aligned} \tau &= \sigma \tan\left(\phi_\mu + i\right) && \text{for low } \sigma \\ \tau &= S_j + \sigma \tan\phi_r && \text{for high } \sigma \end{aligned} \qquad (4.1)$$

where σ is the normal stress acting across the joint, ϕ_μ is the basic friction angle, i is the joint dilation or roughness angle, S_j is the shear strength intercept and ϕ_r is the residual friction angle. Figure 4.1 illustrates this bilinear shear strength criterion.

The expression for τ in low normal stress conditions, known as Patton's law, accounts for the shear resistance caused by overriding of asperities inclined at i degrees to the mean joint plane during the shearing process. Figure 4.2 illustrates the limit equilibrium condition that gives rise to the additional shearing resistance caused by inclined asperities. In addition to the peak shear strength, the shape of the shear stress - shear deformation curve and the rate of dilatancy are also controlled by surface roughness (Goodman, 1989).

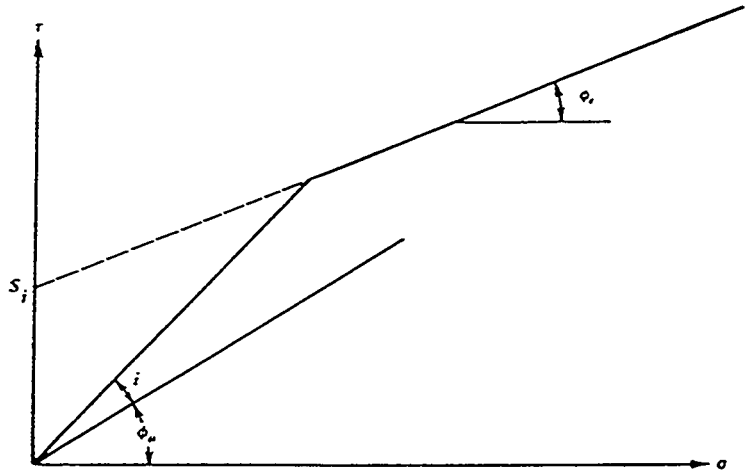

Figure 4.1: Bilinear shear strength criterion (after Goodman, 1976)

With increasing normal stress, less shearing force is required to shear through the asperities than to override them. Under such conditions, Patton's law is replaced by an expression that combines the shear strength intercept and the residual friction angle as shown in Figure 4.1 and Eqn. (4.1). Goodman (1976) provides a review of alternate equations to the bilinear criterion.

In addition to its contribution to shear strength through the dilation angle, surface roughness also brings about an increase in shear strength in confined conditions due to the volume change it causes. If the blocks on either side of the joint are not free to dilate as shear displacement takes place, additional normal stress is developed across the joint. This increase in normal stress increases the shearing resistance over the next increment of shear displacement. Heuze (1979) gives analytical expressions for increments of normal stress developed under such circumstances and Boyle (1980) shows the influence of this phenomena on block stability using a block reaction curve.

The fundamental role of joint surface roughness in shear strength has led to the development of several methods of measuring roughness profiles and dilation angles from accessible joint surfaces. Fecker and Rengers (1971)

measured dilation angles at various scales by measuring the orientation of flat plates of different lengths. Wire gauges profilometers have been used by Barton and Choubey (1977) for profiling along a line. Similarly, profiles have been obtained using a laser sensor (Tanimoto et. al.) and from photographs using photogrammetric techniques (Miller et. al., 1989).

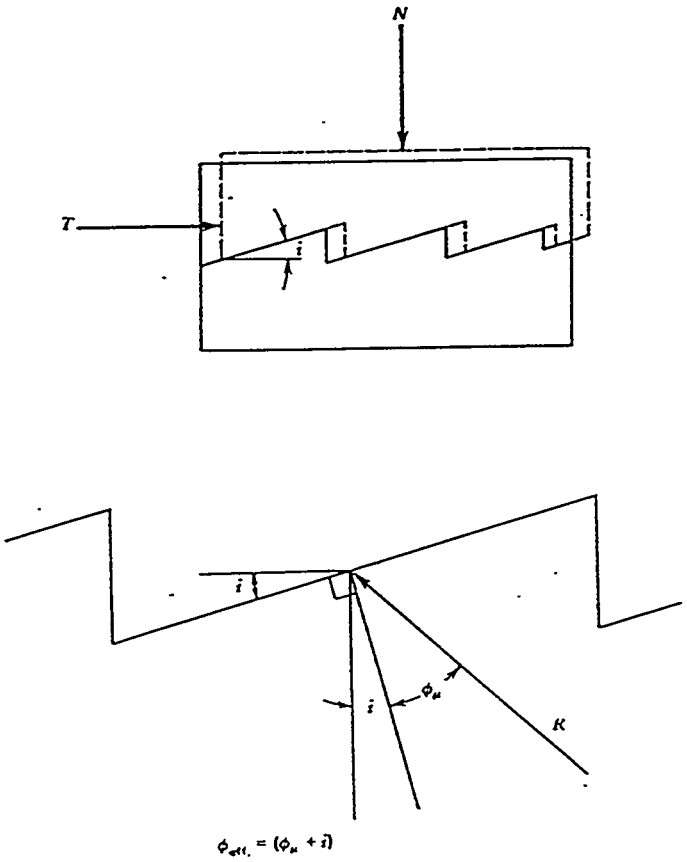

Figure 4.2: Limit equilibrium represented by Patton's law (after Goodman, 1989)

Analysis of joint roughness profiles for the dilation angle is done by making repeated measurements of lines connecting profile points separated by a range of base lengths, as first described by Rengers (1970). The roughness angles measured in this way are plotted as a function of base length. The

envelope to all points plotted in this way is known as the Rengers envelope. Figure 4.3 illustrates Rengers method and the resulting envelope. The roughness angle for the displacement distance of interest can be read off directly from the Rengers envelope and used in Eqn. (4.1) to estimate the joint shear strength. Barton and Choubey (1977) recommend using 1% of the block size as the peak displacement distance. In addition to the shear strength, Rengers envelope can also be used for calculating the dilatancy and shear deformation curves, as described by Schneider (1976).

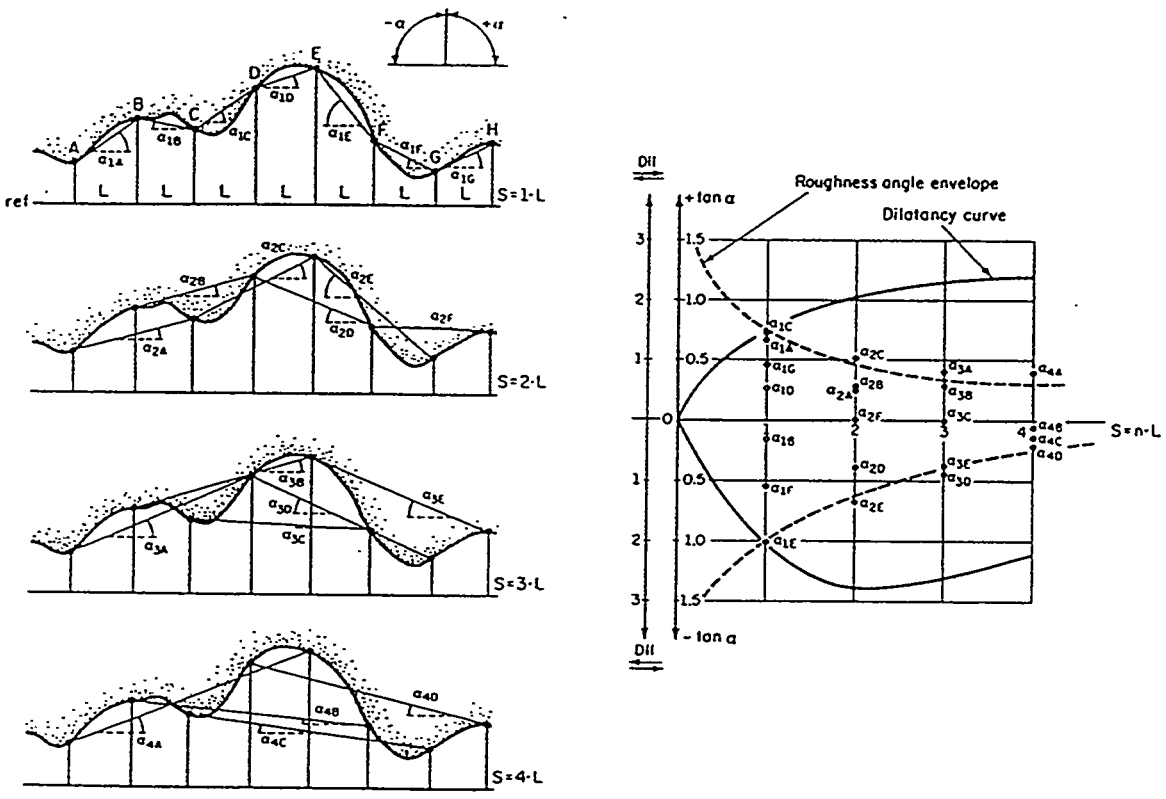

Figure 4.3: Rengers roughness analysis and envelope (after Goodman, 1976)

4.2.2 Estimation of Rengers envelopes using BSS profiles

The roughness profile points extracted from the BSS image constitute a sample of the joint surface topography along a path determined by the intersection of the borehole with the joint surface. This interpretation of the BSS

profile is based on an assumption that the drilling process has not altered the joint roughness. Furthermore, the borehole is assumed to be circular and vertical for the calculation of the location of all image pixels. The difference between the BSS derived sample and profiles obtained by other methods is the non-linear profiling path and in-situ measurement in the case of the BSS profile.

As described earlier, calculation of the dilation angle is done with respect to a mean joint plane. The shearing process is assumed to involve translation along this mean translation plane and dilation normal to it but no rotation about it. One way to determine the orientation the mean translation plane is to use the estimate of the orientation of the joint in the BSS image. This method has the disadvantage of misrepresenting the mean translation plane due to local joint waviness. An alternate method is to fit planes between sets of three contacting points on the joint and use the mean of these planes as the mean translation plane. However, this method cannot be used on joints where there are no contacting points in the BSS sample of the opposing joint surfaces. The joint orientation measured in the BSS image is assumed to be the mean translation plane in this thesis. The Expert program was used to estimate the joint orientations.

The roughness angle is calculated from the angle between chords connecting profile points and the normal vector to the mean translation plane:

$$i = 90 - \tan^{-1}\left(\frac{\bar{c} \bullet \bar{n}}{\|n\|}\right) \qquad (4.2)$$

where $\bar{c}$ is the chord vector connecting two profile points and $\bar{n}$ is the joint unit normal vector. The unit joint normal vector $n(a,b,c)$is obtained from the strike (α) and dip (β) of the joint as

$$a = \sin\alpha \sin\beta$$
$$b = \sin\alpha \cos\beta \qquad (4.3)$$
$$c = \cos\alpha$$

The magnitude of the base length, d, for each chord is

$$d = \|\vec{c}\| \cos(i) \qquad (4.4)$$

Rengers envelope for a specific sliding direction can be constructed by finding the maximum roughness angles made by all chords pointing in the sliding direction. The upper and lower joint profiles are evaluated individually. For each $(i\ ,d)$ pair of the envelope calculated for a certain sliding direction, there will be a symmetric $(-i\ ,d)$ pair for the opposite direction. The upper limit of the base length that can be obtained depends on the borehole size and the dip angle of the joint. In the case of joints analyzed in boreholes 3-5 and 4-1, this upper limit is about 90 mm. The lower limit of the base length depends on the resolution.

If the surface roughness of the joint being analyzed is isotropic, the construction of the Rengers envelope can utilize all pairs of profile points for calculating $(i\ ,d)$ pairs, and not just those that define chords in a specific direction. The increase in the number of profile sample point pairs used in this case leads to a more reliable Rengers envelope. Evaluation of joint isotropy is described later in this chapter.

A computer program was written to implement the method described above. The program reads in points on a profile, calculates pairs of $(i\ ,d)$ points in one or all directions and prints the results to an ASCII file. In order to verify the program, it was tested using a synthetic profile generated from points of intersection of a vertical borehole and a smooth joint plane. The Rengers envelope produced by using the synthetic profile shows the roughness angle to be zero at all base lengths, as expected. At very small base lengths, the

roughness angle is greater than zero due to numerical errors as shown in Appendix C.

4.2.3 Renger's envelopes for borehole 3-5 joints

Rengers envelopes were calculated for joints in borehole 3-5. Figure 4.4 shows Rengers envelopes for the upper and lower profiles of joint 19-1, which happens to be a joint with isotropic roughness as explained later. In the case of joint 19-1, the upper and lower profiles have nearly the same Rengers envelopes although the lower profile has consistently lower roughness angles at all scales by a few degrees. Unlike the perfectly mated opposing joint profiles analyzed by Rengers, the opposing profiles from BSS images will not necessarily produce identical envelopes. This is because the in-situ condition may not be one where the opposing profiles are perfectly mated. Infact, differences in the envelopes of opposing profiles may provide an indication of preferential joint wall alteration or wear of wall asperities. For instance, the slightly lower roughness angles of the lower profile in Figure 4.4 may be due to mineralogical alteration of the lower joint wall by unsaturated fluid flow.

The shape of the roughness angle curve shows a decreasing roughness angle with increasing displacement distance as expected. The roughness angle is seen to increase rapidly at displacement distances of less than 20 mm and decreases gradually at larger displacements. The large roughness angles observed at very small scales shown in Figure 4.4 is in agreement with similar conclusions reached by Barton (1980).

Rengers envelopes for joint 21-1, which has anisotropic roughness, are shown in Figure 4.5 for the minimum and maximum roughness directions of each profile. As with joint 19-1, joint 21-1 has similar envelopes on opposing profiles. However, the anisotropy of joint 21-1's surface roughness results in a substantial difference in the envelopes taken in the maximum and minimum

roughness directions (analysis for the maximum and minimum roughness directions are described later). The difference in roughness angle is lowest at small displacement distances and increases to a high value of about 20 degrees at a displacement distance of about 45 mm. Thereafter, the difference decreases gradually.

Rengers envelopes for some additional joints from borehole 3-5 are given in Appendix D.

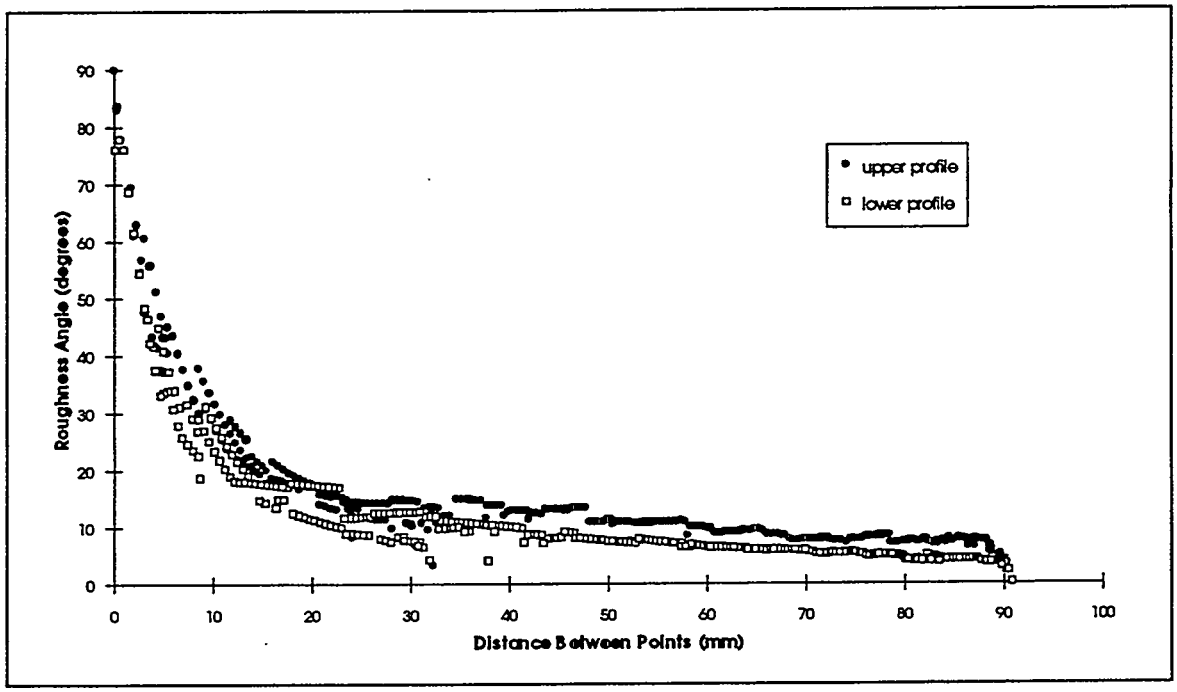

Figure 4.4: Rengers envelopes for opposing profiles of joint 19-1

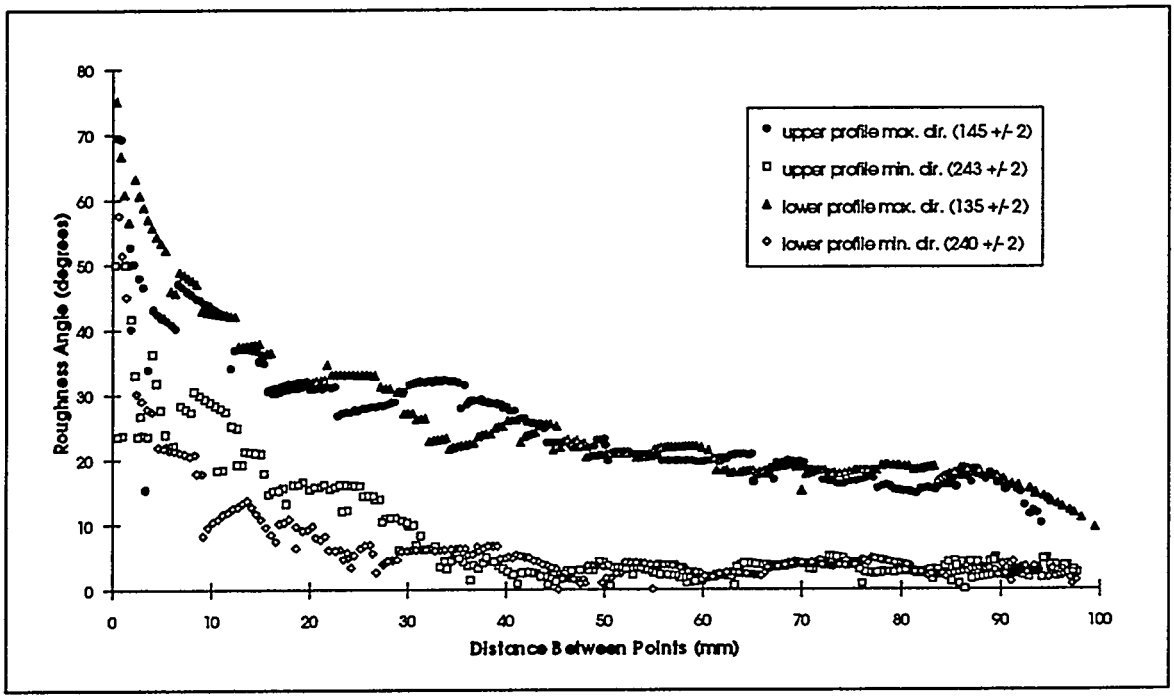

Figure 4.5: Rengers envelopes for opposing profiles of joint 21-1

4.3 Dilation angle anisotropy

After a brief review of the sources, importance and existing analysis of surface roughness, this section describes how dilation angle anisotropy may be measured using BSS data. The method is then applied to joints from borehole 3-5.

4.3.1 Background

The surfaces of natural joints may have some structure that leads to anisotropic roughness. Figure 4.6 shows a schematic drawing of some surface morphology features of joints described by Suppe (1985). The fringe is composed of a series of en-echelon fractures at the edge of the joint surface. Plumose structure consists of undulations along lines fanning out from a single point and terminating at the fringes. Conchoidal structures are discrete jumps in joint orientation occurring perpendicularly to the plumose structure lines. Other types of surface structures such as striations and ripple marks may also be observed. Figure 4.7 shows a saw-tooth surface structure from a joint in slate at

the Auburn dam site in California. All of these surface structures would lead to anisotropic dilation angles.

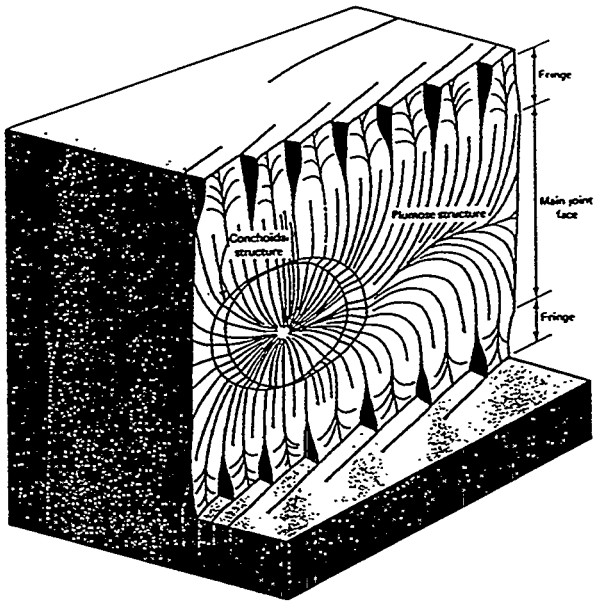

Figure 4.6: Schematic of joint surface morphology (after Suppe, 1985)

Dilation angle anisotropy leads to anisotropic joint strength. This fact makes dilation angle anisotropy a critical element in the stability of discontinuous rockmasses. Blocks defined by intersecting discontinuities are kinematically constrained to move only in certain directions. As a result of the dilation angle anisotropy, the directions in which key blocks may move could be relatively weak or strong depending on the joint strength.

Despite the importance of anisotropic dilation angles in deformation problems, the topic has received little attention in the past. Goodman (1976) presents an example of anisotropic roughness using a scatter plot of joint normals on a stereonet, and shows how the profiling direction leads to dilation angle anisotropy on a joint surface composed of planes with the same dip and

Figure 4.7: Saw-tooth joint morphology from Auburn dam, California

opposite dip directions. Huang and Doong (1990) performed laboratory direct shear tests on joint replicas in different directions and compared the results to predictions using Barton's equation (Barton and Choubey, 1977) based on profiles measured in nine separate directions. They found that the laboratory shear strengths were anisotropic, but that the anisotropy decreased with increasing normal stress. Also, they found that the analytical predictions using the anisotropic roughness profiles gave results which were close to the laboratory test results. Harrison and Goodfellow (1993) describe an analytical method of quantitatively evaluating roughness anisotropy at various scales using

multivariate statistics. After applying the method on four joints, they found that the roughness anisotropy decreases with increasing scale.

4.3.2 Method of anisotropy analysis - example of joint 10-1

The analysis of the BSS derived roughness profiles for dilation angle anisotropy is the same as the analysis for the roughness angle in terms of calculating pairs, (i, d), of dilation angles and baselengths. However, in the case of the anisotropy analysis, the azimuth of the vector connecting pairs of profile points is also calculated, so that the result consists of a list of triplets (i, d, a) where a stands for the azimuth of the vector defining the triplet. Note that these triplets correspond to the maximum dilation angle in a given direction and at a certain scale.

The anisotropy analysis method was coded in a program. The program reads pairs of points defining one joint profile and prints out a file containing pairs of (i, a) points at up to five scale intervals chosen by the user. The program was tested on the already mentioned synthetic profile data. The first test case was a smooth joint (45/180) which gave a computed dilation angle of zero in all directions at all scales. In a second test, the synthetic profile for a smooth flat joint was modified by raising the z axis position of profile points between azimuths 85 and 90, by 5 mm. As expected, at a scale slightly larger than the borehole diameter, the roughness angle was greater than zero between azimuths 85 and 90 while the roughness angle remained zero in other directions. The second test was repeated on a smooth plane inclined at 45 degrees and the program was found to give correct results for this test profile as well. The results of the first two verification tests are given in Appendix E.

The (i, a) data pairs generated by the anisotropy analysis program are used to produce an anisotropy curve for each opposing joint profile as shown in

Figure 4.8 for joint 10-1 in borehole 3-5. The anisotropy curve of Figure 4.8 is presented in terms of four scale intervals.

4.3.3 Interpretation of anisotropy curves

Interpretation of the joint surface topography from the anisotropy curve of Figure 4.8 is an inverse problem. Different surface shapes will produce different anisotropy curves. Furthermore, as with any inverse problem, the solution to the surface topography problem may not be unique -- i.e. more than one surface topography model may satisfy the anisotropy curve. The simplest anisotropy curve would be a flat line within a small roughness angle interval. For this case, the joint surface model would simply consist of a smooth plane. The first and third tests used to verify aniso.c correspond to this case (see Appendix A.5). As the shape of the anisotropy curve becomes more complex, the interpretation also becomes more difficult. In this thesis trial and error is used to find a surface model that fits the anisotropy curve.

It is not always necessary to find a surface topography model to use the anisotropy curve. For mechanical stability problems for instance, just knowing whether there is any anisotropy will enable further analysis to account for the effect of surface shape. If the surface is found to be anisotropic, Rengers envelopes will have to be taken in the sliding direction only. Direct shear tests should also be done in the sliding direction in this case.

The deviation of joint surfaces from planarity is generally considered to be the result of roughness at small scales and waviness at large scales. Since undulations at both scales can affect the peak shear strength, it is necessary to determine the scale of interest before attempting to interpret anisotropy curves. For mechanical problems, Barton and Choubey's (1977) recommendation of using 1% of the joint length as the peak shear displacement distance can be

Fig. 4.8(a.1): Anisotropy curve for lower profile of joint 10-1 at a scale of 4.5 to 5.5 mm

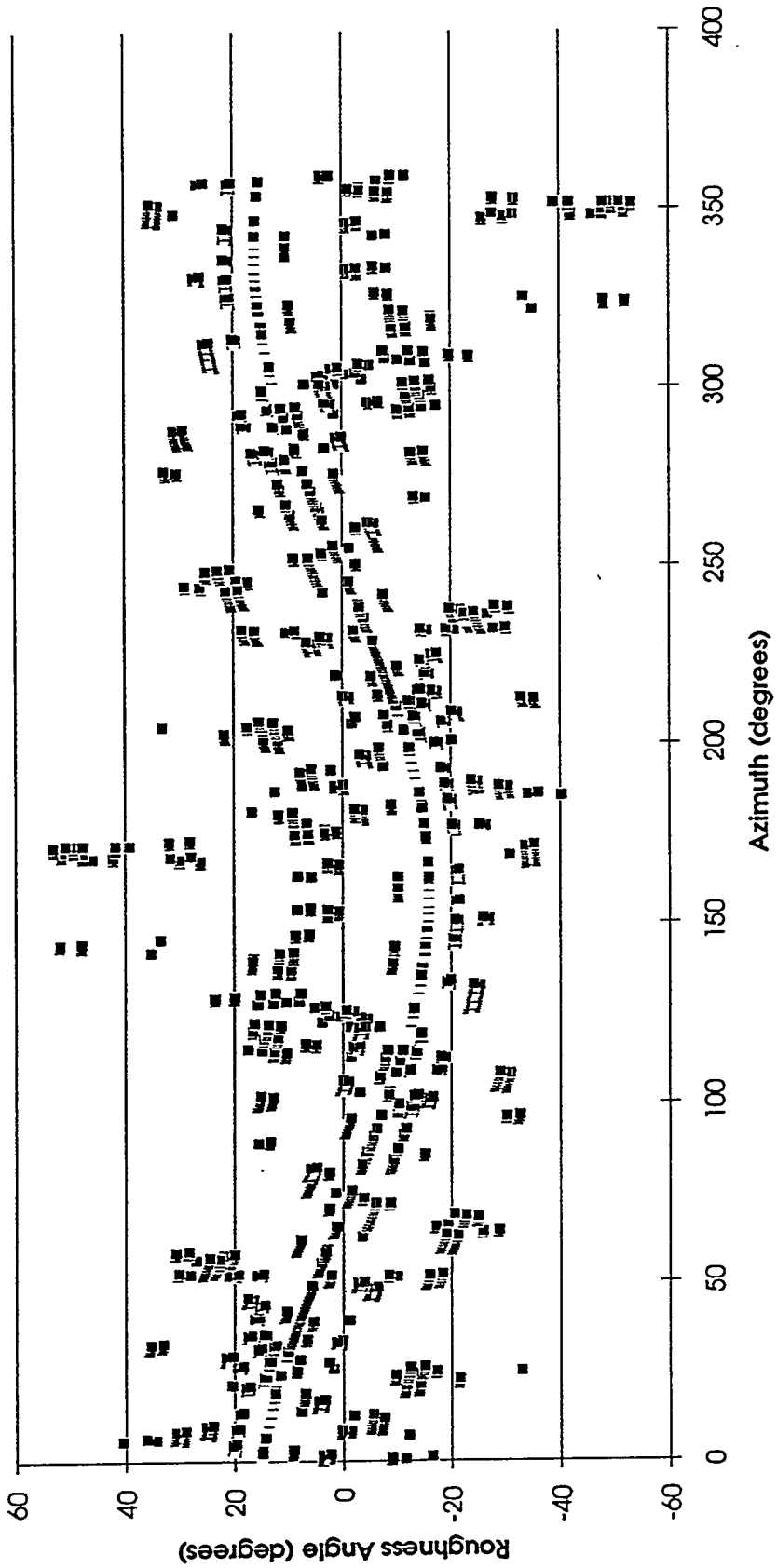

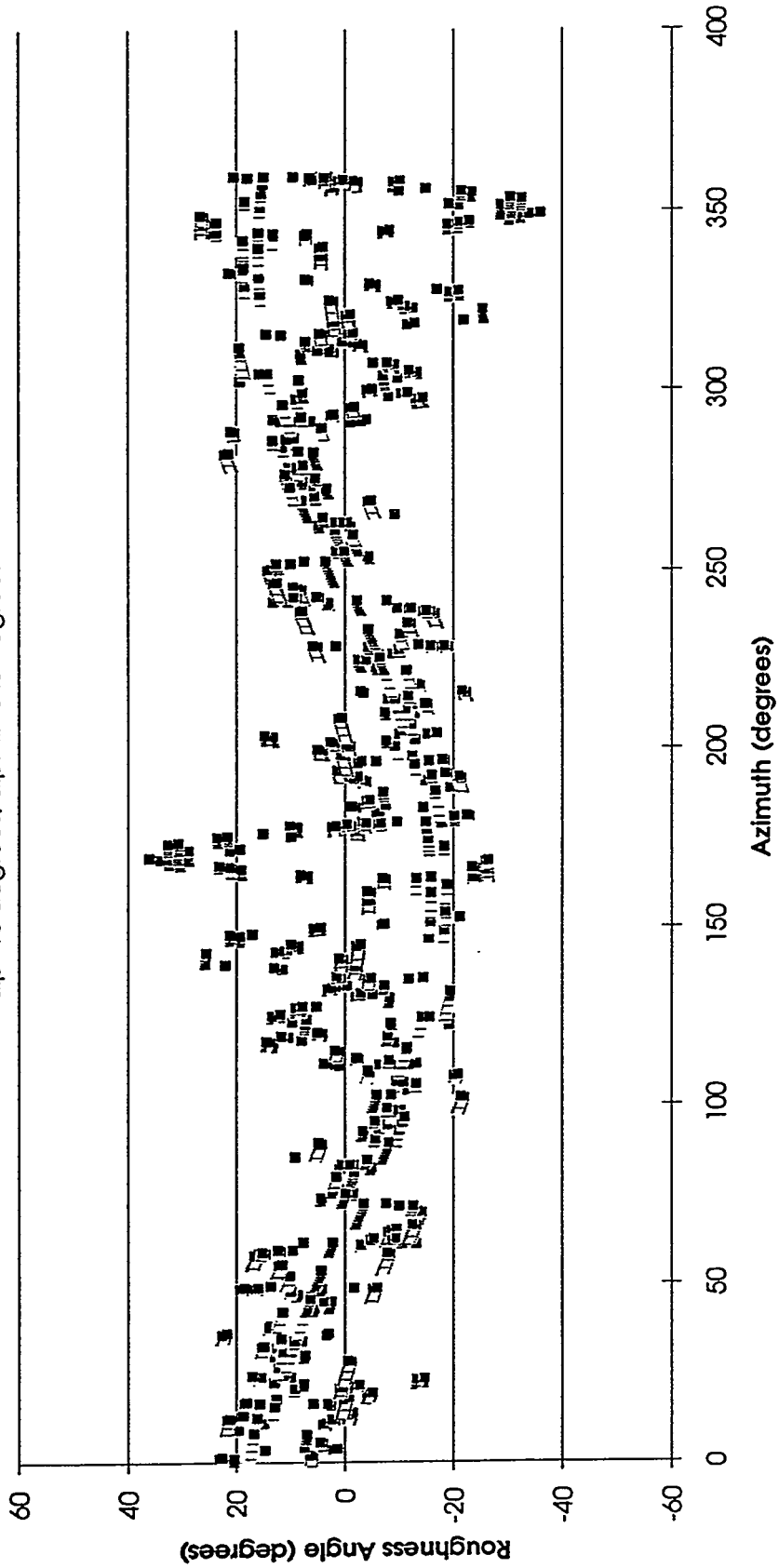
Fig. 4.8(a.2): Anisotropy curve for lower profile of joint 10-1 at a scale of 9.5 to 10.5 mm
dip=16 degrees, dip.dir=340 degrees
Roughness Angle (degrees)
60
40
20
0
-20
-40
-60
Azimuth (degrees)
0
50
100
150
200
250
300
350
400

Fig.4.8(a.3): Anisotropy curve for lower profile of joint 10-1 at a scale of 34.5 to 35.5 mm

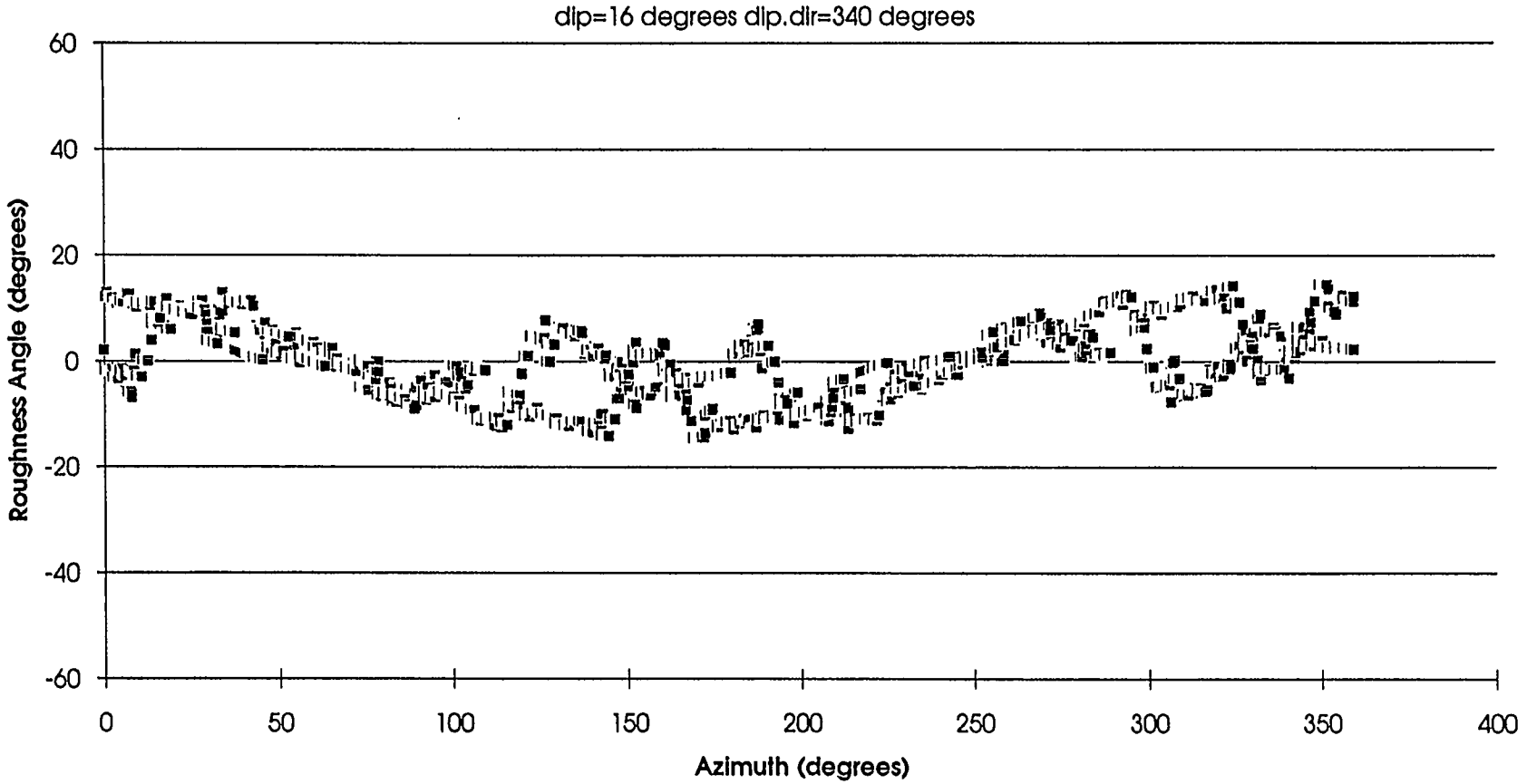

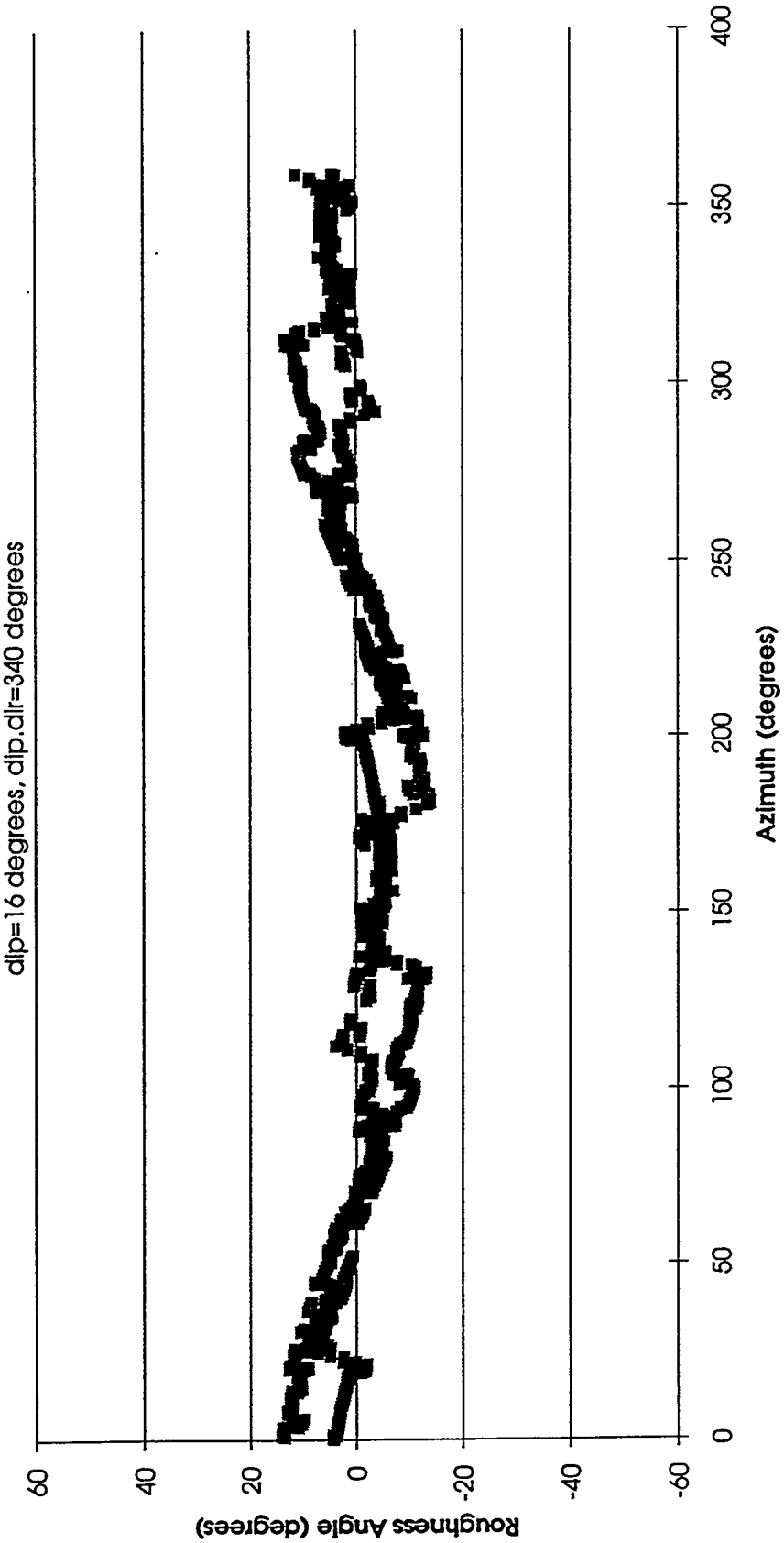

Fig. 4.8(a.4): Anisotropy curve for lower profile of joint 10-1 at a scale of 49.5 to 50.5 mm

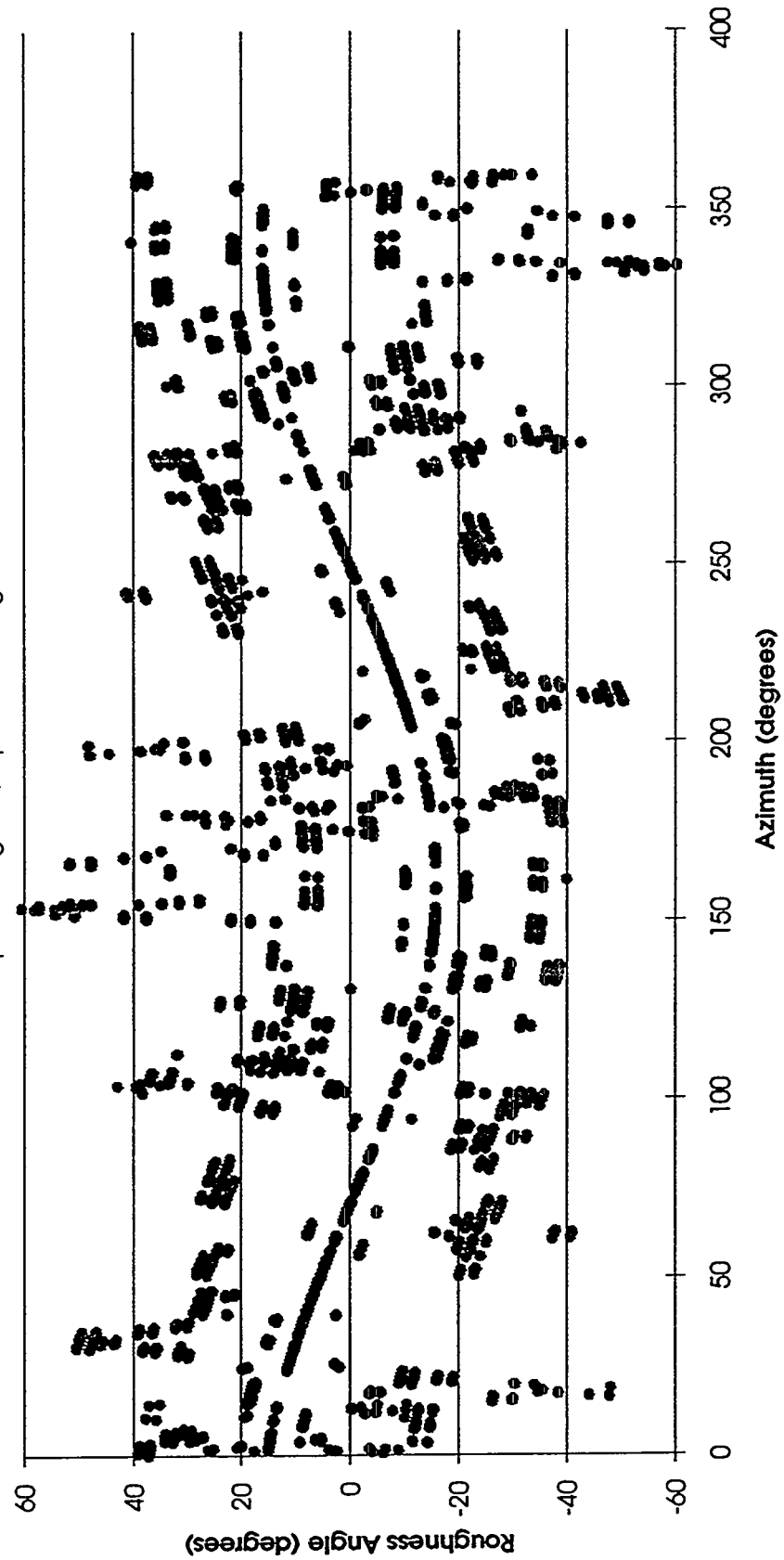

Fig. 4.8(b.1): Anisotropy curve for upper profile of joint 10-1 at a scale of 4.5 to 5.5 mm

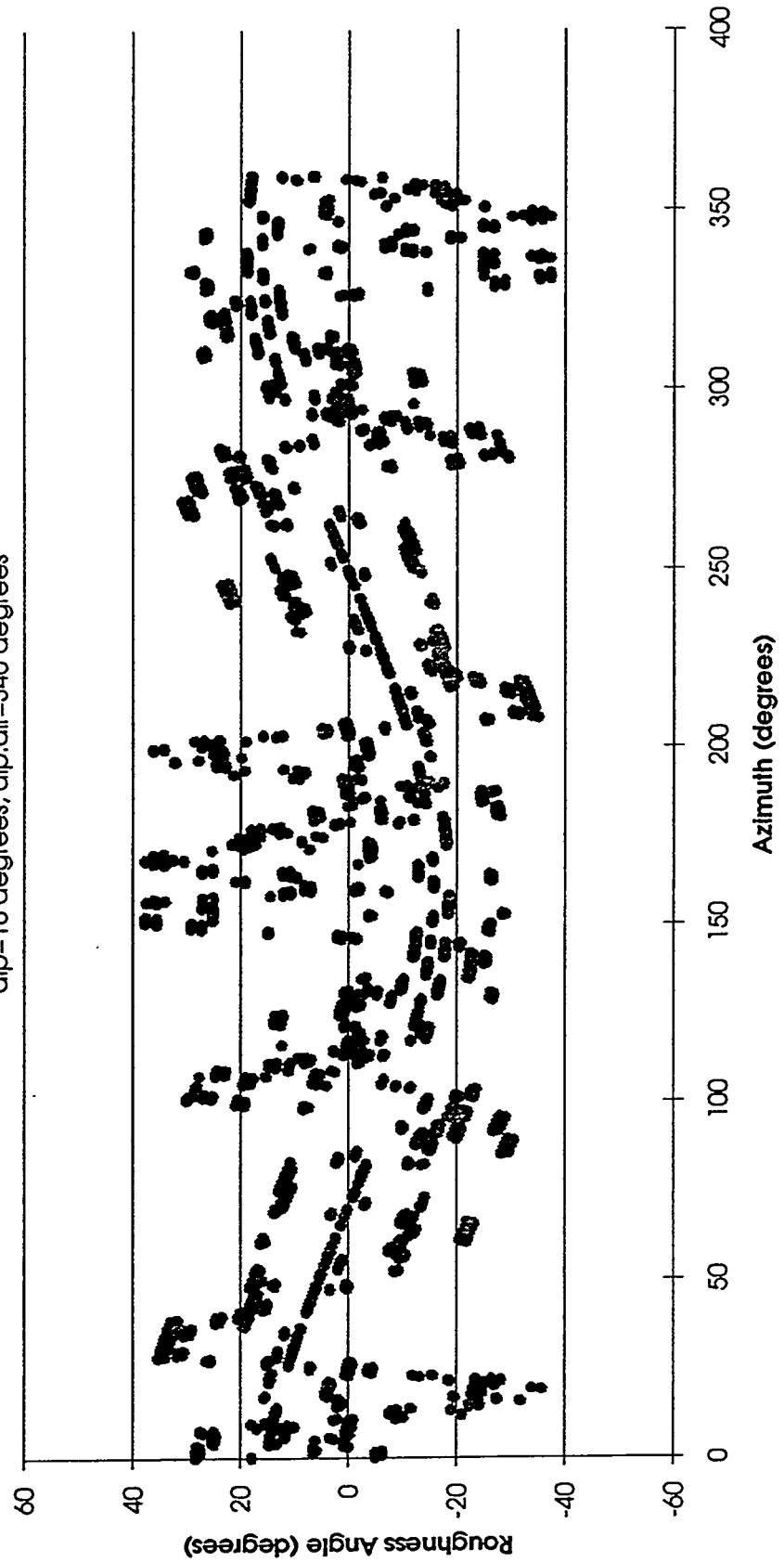

Fig. 4.8(b.2): Anisotropy curve for upper profile of joint 10-1 at a scale of 9.5 to 10.5 mm

Fig. 4.8(b.3): Anisotropy curve for upper profile of joint 10-1 at a scale of 34.5 to 35.5 mm

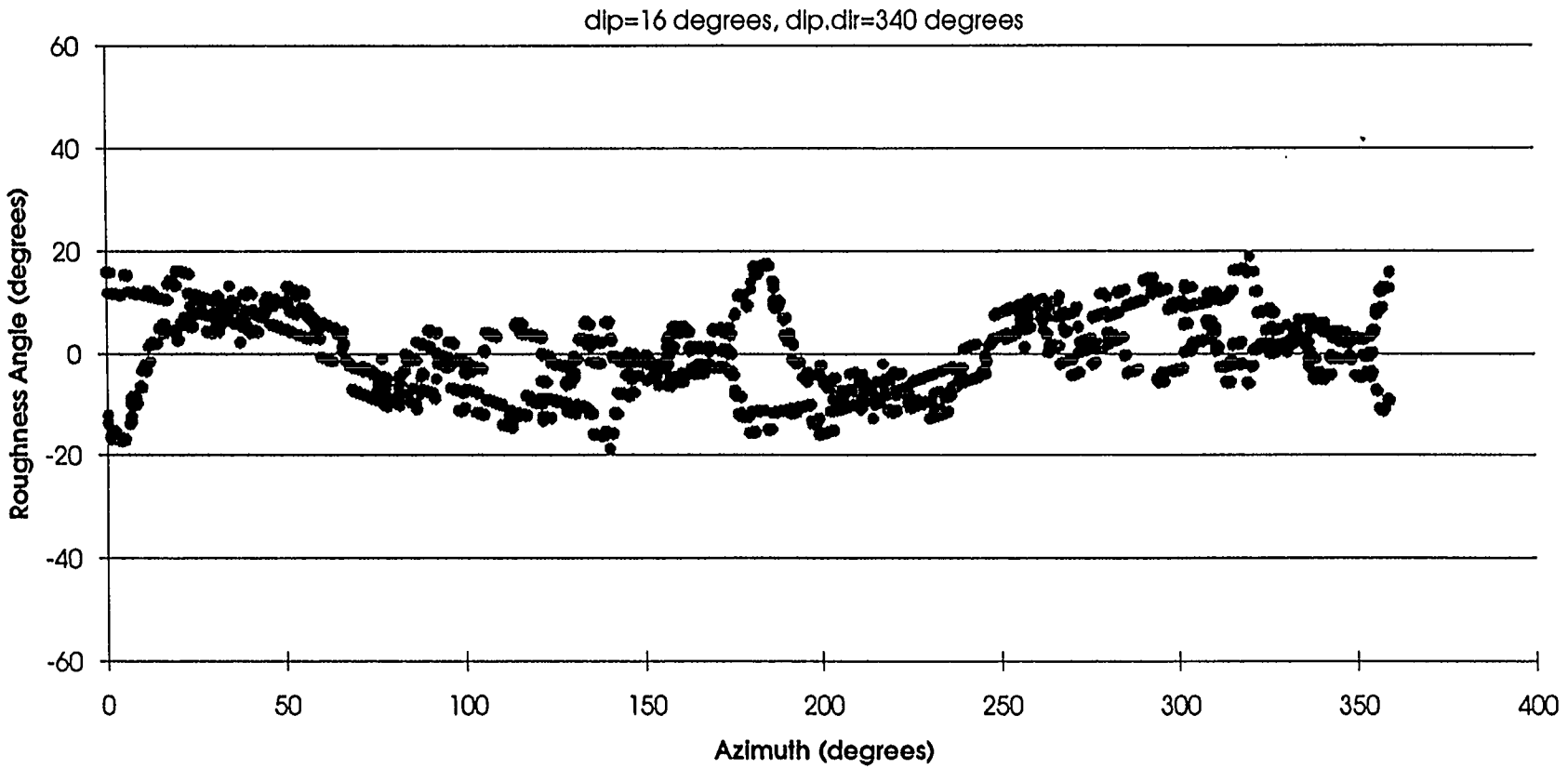

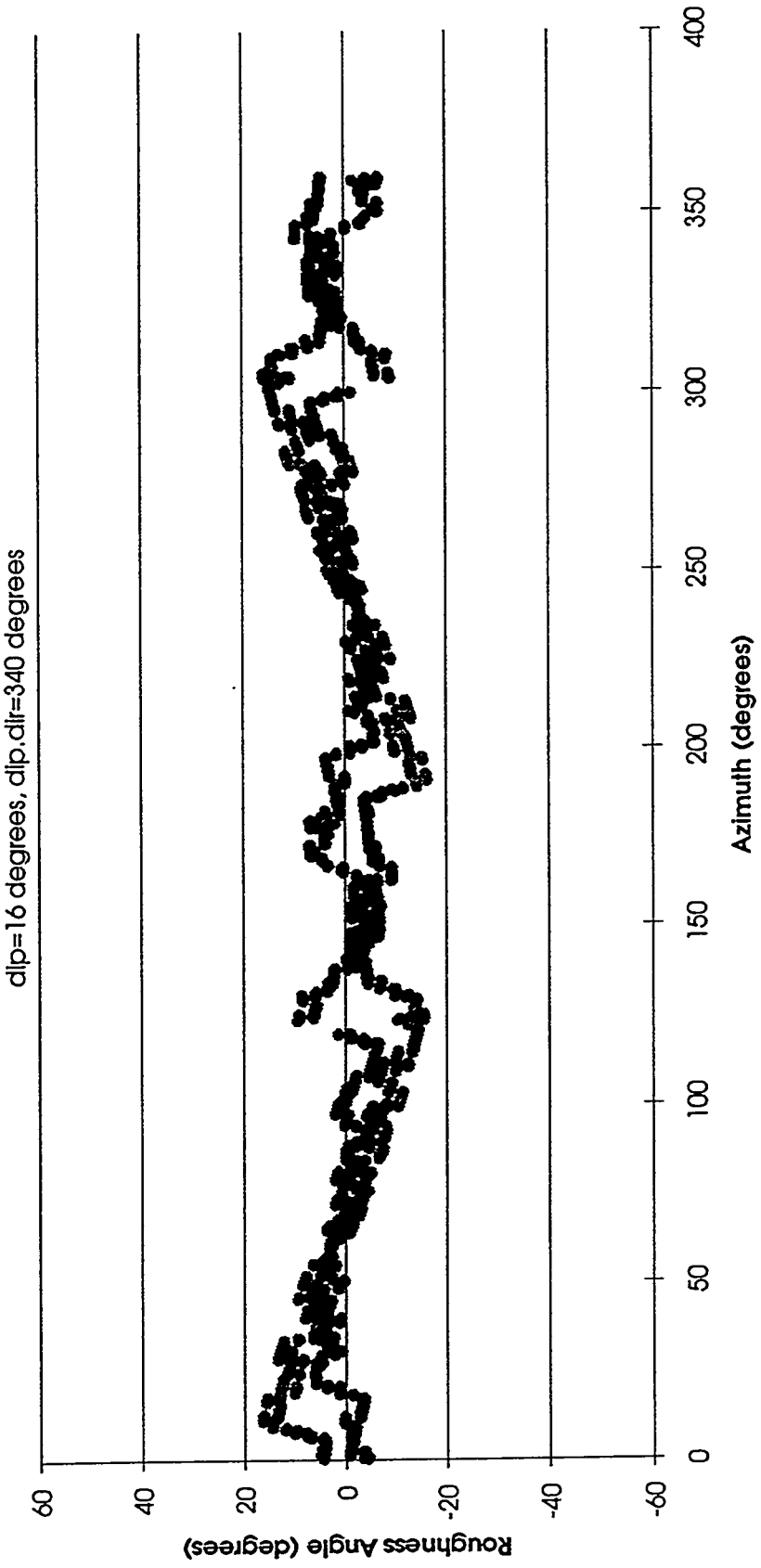

Fig. 4.8(b.4): Anisotropy curve for upper profile of joint 10-1 at a scale of 49.5 to 50.5 mm

used to select the scale of interest, as explained earlier for the use of Rengers envelope. For purposes of anisotropy curve interpretation herein, the average block size or joint length, is assumed to be 1 m so that surface undulations at scales of less than 1 cm are considered to be roughness that contributes to peak shear strength while undulations at scales larger than 1 cm are considered to be part of the joint's waviness which does not influence peak shear strength.

The anisotropy curves shown in Figure 4.8 are symmetric about azimuth 180, since each vector that connects profile points produces a positive and negative dilation angle in opposite directions, as explained in Section 4.2.2. In Figure 4.8(a), the dilation angles appear to be close to isotropic. However, there are azimuth intervals, such as between 50 and 100, in which the dilation angles are clearly lower than in other directions. In contrast to the small scales, the larger scales define a clear pattern of anisotropy. The larger scales show the dilation angles to be about 20 degrees towards the dip direction and its opposite, while the dilation angle is shown to be zero towards the strike directions. The dilation angles between these four directions have intermediate values of the dilation angle. This pattern fits a model consisting of a nearly planar surface with the same dip direction as the joint, but with a slightly larger dip as shown in Figure 4.8(c). Thus the undulation about the mean plane shown in Figure 4.8(a) at the larger scales could be the joint waviness. However, the anisotropy curve may also be reflecting an error in the dip of the mean joint plane. The anisotropy curve for the upper joint wall shown in Figure 4.8(b) indicates a more isotropic surface roughness at the small scales compared to the lower joint wall. The waviness at larger scales on the upper joint wall resembles the waviness of the lower joint wall.

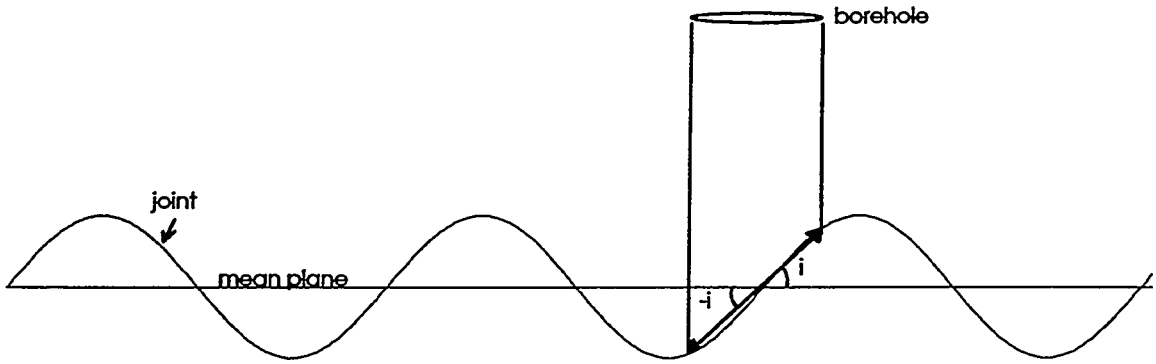

Anisotropy curves for this undulating joint surface are shown below for two dip directions. The maximum roughness angle is observed along the dip direction and the roughness angle is zero along the strike. Intermediate values of the roughness angle are observed in between these directions.

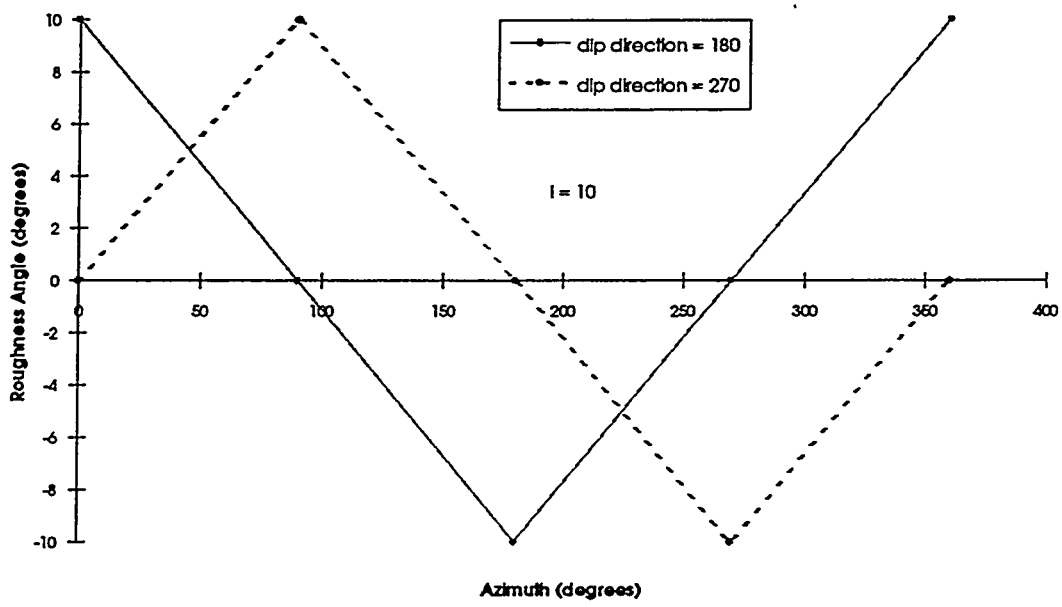

Figure 4.8(c): Interpretation of joint waviness from anisotropy curves

4.3.4 Anisotropy of borehole 3-5 joints

Anisotropy curves were constructed for the opposing joints profiles from borehole 3-5. Two scales of 5 mm $\pm$ .5 and 10 mm $\pm$ .5 were used to analyze roughness anisotropy. Two other scales of 34 mm $\pm$ .5 and 50 mm $\pm$ .5 were

used to assess waviness anisotropy. Some of the anisotropy curves analyzed from borehole 3-5 are given in Appendix F as examples. Table 4.1 summarizes the findings of this anisotropy analysis.

Table 4.1 shows that most of the joint surfaces are anisotropic at the larger scales corresponding to waviness. Very few joints are isotropic at any scale, but many joints are close to being isotropic at the smaller scales and especially at the smallest scale. In Table 4.1, the joints labeled as being close to isotropic typically show lower roughness angles in one or two narrow azimuth bands. If a larger interval were used to specify the scale of interest in the anisotropy analysis program, it is possible the additional $(i\ ,a)$ samples would tend to make the anisotropy curve appear more isotropic. Also, judging from the trend of decreasing anisotropy at smaller scales, analysis of anisotropy at scales less than 5 mm would probably show even more roughness isotropy than seen at the smaller scales in Table 4.1.

The data in Table 4.1 show that when the joint surface is close to being isotropic, it is usually so at small scales and exhibits anisotropy with increasing scale. This characteristic is probably due to waviness at larger scales. Examples of this are seen in the case of joints 13-1, 15-3, 19-2, 19-3 and 21-2. There is a disagreement between this observation and the finding of Harrison and Goodfellow (1993) who found anisotropy to decrease with increasing scale. This disagreement is probably due to the differences in scales used here and in Harrison and Goodfellow's studies where the scales used ranged from 75 mm to 200 mm. The scales used here are reflecting an increase in the anisotropy due to a transition from roughness to waviness, while the large scales used by Harrison and Goodfellow will tend to show decreasing anisotropy as the wavelength of the waviness is exceeded. However, there are joints in borehole 3-5 that follow the trend described by Harrsion and Goodfellow even at the

smaller scales used in this thesis. Joint 20-2 and the lower profile of joint 19-1 are such examples.

Table 4.1: Anisotropy analysis results for joints of borehole 3-5

Joint	Lower Profile Scales in mm				Upper Profile Scales in mm			
Label	4.5-5.5	9.5-10.5	34.5-35.5	49.5-50.5	4.5-5.5	9.5-10.5	34.5-35.5	49.5-50.5
9-1	NI	NI	A	A	NI	A	A	A
10-1	NI	NI	A	A	NI	NI	A	A
10-2	A	A	A	A	A	A	A	A
10-3	NI	A	A	A	NI	A	A	A
10-4	A	A	A	A	A	A	A	A
11-1	A	A	A	A	NI	NI	A	A
13-1	I	NI	A	A	NI	NI	A	A
13-2	NI	A	A	A	NI	NI	NI	NI
14-1	A	A	A	A	NI	NI	A	A
14-2	A	A	A	A	A	A	A	A
14-3	NI	A	A	A	A	A	A	A
14-4	A	A	A	A	A	A	A	A
15-1	NI	NI	NI	NI	NI	NI	A	A
15-2	A	A	A	A	A	A	A	A
15-3	NI	A	A	A	NI	A	A	A
15-4	NI	NI	I	I	A	A	A	A
15-5	A	A	A	A	I	A	A	A
17-1	A	A	A	A	A	A	A	A
17-2	A	A	A	A	A	A	A	A
18-1	A	A	A	A	A	A	A	A
19-1	A	A	NI	NI	NI	NI	NI	NI
19-2	NI	A	A	A	NI	A	A	A
19-3	NI	NI	A	A	NI	NI	A	A
19-4	A	A	A	A	A	A	A	A
20-1	A	A	A	A	NI	NI	A	A
20-2	A	A	NI	NI	A	A	NI	NI
20-3	A	A	A	A	A	A	A	A
21-1	A	A	A	A	A	A	A	A
21-2	I	NI	A	A	I	I	A	A
21-3	NI	A	NI	NI	I	NI	NI	NI
A: anisotropic; I: isotropic; NI: nearly isotropic								

The anisotropy curves at the smaller scales do not fall into a clear pattern that would allow a surface topography to be interpreted. With increasing scale, the anisotropy curves begin to show patterns. Most of the joints show a near

planar waviness towards the dip direction as in the case of joint 10-1 described in Section 4.3.3. From this observation, it appears joint waviness usually involves undulations about the mean plane towards the dip direction. Table 4.2 lists the interpretation of waviness forms made form the anisotropy curves for borehole 3-5 joints.

Table 4.2: Form of anisotropy at larger scales in borehole 3-5 joints

Joint	Upper Profile	Lower Profile	Joint	Upper Profile	Lower Profile
9-1	near plane	near plane	15-4	near plane	smooth
10-1	near plane	near plane	15-5	near plane	near plane
10-2	complex	complex	17-1	near plane	near plane
10-3	complex	complex	17-2	near plane	near plane
10-4	complex	complex	18-1	near plane	complex
11-1	complex	complex	19-1	smooth	smooth
13-1	near plane	smooth	19-2	near plane	near plane
13-2	near plane	near plane	19-3	complex	near plane
14-1	smooth	complex	19-4	near plane	near plane
14-2	near plane	near plane	20-1	near plane	near plane
14-3	complex	complex	20-2	near plane	near plane
14-4	complex	complex	20-3	near plane	near plane
15-1	near plane	near plane	21-1	near plane	near plane
15-2	near plane	near plane	21-2	near plane	near plane
15-3	complex	complex	21-3	smooth	smooth

4.4 Unrolling profiles into two dimensions

The roughness profiles extracted from the BSS image are samples of points from opposing three dimensional curved surfaces of the joint walls. These samples lie along curves determined by the intersection of the borehole with the joint walls. Unrolled two dimensional opposing joint profiles are desirable since the methods of analyzing joint shear strength, described later in this chapter, require a two dimensional representation of the opposing joint profiles. Prior to unrolling, pairs of opposing profile points have to be defined. This pairing produces measurements of the joint aperture. The aperture measurement method is explained before going on to the discussion of profile unrolling.

4.4.1 Aperture measurement

Joint aperture is defined by the magnitude of the vector connecting points on the lower profile to points on the upper profile. The vector connecting opposing profile points is directed normal to the mean joint plane. When the mean joint plane is has a dip greater than 0^{o} and less than 90^{o}, and the borehole is vertical, the aperture vector originating on a lower profile point will generally not intersect any upper profile point. This situation is shown in Figure 4.9. Since the majority of joints intersected by the borehole will have a geometric configuration similar to Figure 4.9, measurement of joint aperture requires some method of accounting for this problem.

Figure 4.9 shows two smooth opposing joint walls with the same orientation being intersected by a vertical borehole. The intersection produces traces of the borehole wall in the upper and lower profiles. These traces, in discrete form, would be the equivalent of the BSS profiles. The true aperture of the joint is shown by the vector $\bar{n}$ connecting the lower profile point o to its true opposing point a. However, in the BSS profiles, the vector $\bar{n}$ cannot be found since point a does not lie on the curve defined by the intersection of the borehole with the upper joint wall. Since the true aperture cannot be found, one of two alternative approaches may be taken to estimate $\bar{n}$. One approach involves correction of an apparent aperture vector such as $\bar{b}$, which is directed vertically parallel to the borehole axis:

$$\|\bar{n}\| = \|\bar{b}\|\cos\theta \qquad (4.5)$$

The apparent aperture approach assumes the upper joint wall is a smooth plane between points b and a as shown in Figure 4.9. This assumption contradicts the

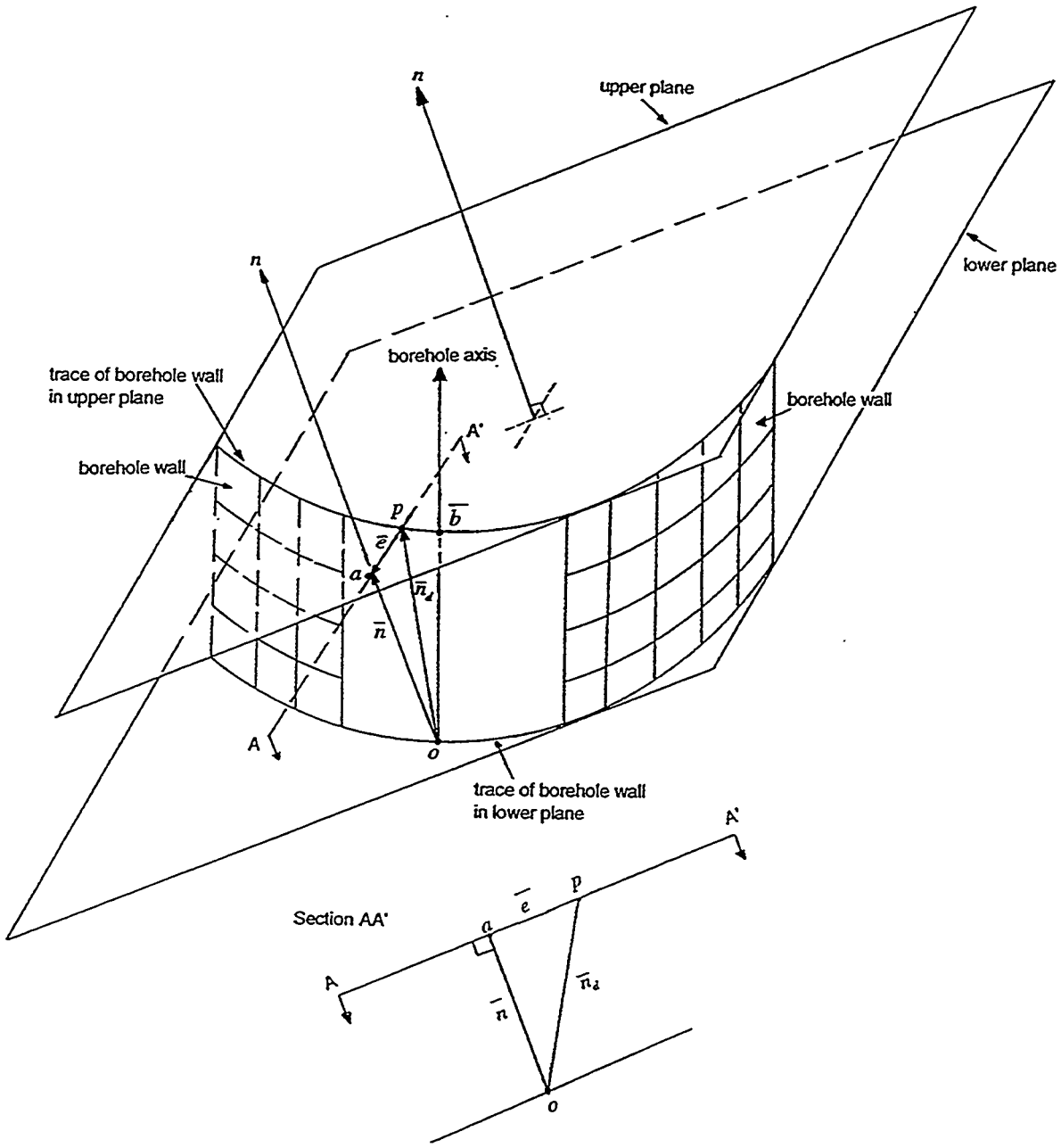

Figure 4.9: Aperture measurement error

entire exercise of measuring roughness and apertures where deviations from a mean plane are being sought. The other approach to aperture measurement uses the vector $\bar{n}_d$ as the estimate of $\bar{n}$. Point p on vector $\bar{n}_d$ is chosen so that the error vector $\bar{e}$ is a minimum along one or more segments of the profile. This second approach, based on error minimization, is used in this thesis in order to observe magnitudes of the aperture measurement error for real joints.

4.4.1.1 Synthetic experiment of aperture measurement error

A synthetic experiment was carried out to study the sensitivity of the aperture measurement error to the geometric parameters defining Figure 4.9. A program was written to generate upper and lower profile points by intersecting a cylinder with two parallel planes separated by a constant true aperture. The borehole diameter, orientation of the planes and the constant true aperture are user defined in the program. Once the upper and lower profile points are generated, the program proceeds with aperture measurement beginning with the highest profile point on the lower profile (this point will be 180^{o} from the dip direction). Using the highest profile point as point o, the program finds point a as

$$a_i = o_i + \bar{n}_i \delta \qquad (4.6)$$

where $i = x, y, z$ and δ is the true aperture

Point p is found by finding a point on the upper profile that lies on a plane (G) perpendicular to both joint planes and having the same strike as the joint planes. Since both $\bar{n}$ and $\bar{e}$ lie on plane G, its coefficients can be found as

$$G(a,b,c) = \bar{e} \times \bar{n} \qquad (4.7)$$

The vector $\bar{e}$ in Eqn. (4.3) is horizontal as it lies along the strike of plane G so $e_z = 0$. The other two unit components of $\bar{e}$ can be found as

$$e_x = \sin(\alpha + 90)$$
$$e_y = \cos(\alpha + 90) \qquad (4.8)$$

where α is the dip direction of the opposing planes

Once point p is found in this way, the vectors $\bar{n}_d$ and $\bar{e}$ are found and their magnitudes stored as one aperture measurement. The point o is then moved to the next lower profile point. Since the problem is symmetric about the dip direction, it does not matter which side of the dip direction is chosen as the next location of point o. The procedure of finding points a and p is then repeated. The search for point p that satisfies the equation of plane G always begins from the highest upper profile point and proceeds sequentially towards the dip direction. Upper profile points that have already been paired with a lower profile point are not used in the search. The first upper profile point found to satisfy the equation for plane G is selected as point p.

Figure 4.10 shows the aperture measurement error for a case with a dip of 45^o and a borehole radius of 10 mm. The error is a minimum at lower profile points with depths in between the high and low profile point depths. The error jumps to a maximum at the high and low profile depth points which lie along the dip direction vector. The errors are symmetrical about the strike as well as the dip direction lines (Figure 4.10 shows apertures measured between 0^o and 180^o only -- the data from 180^o to 360^o produce identical results due to the symmetry). The aperture pairs represented in Figure 4.10 do not include some lower profile points towards the dip direction, as plane G for these points do not intersect any upper profile points.

Other cases with decreasing values of dip were also analyzed. The results for these other cases were similar to Figure 4.10 and are given in Appendix G. These results show that the aperture measurement errors decrease with decreasing dip. The results from all the cases are summarized in Figure

4.11. Analysis of the results shown in Appendix G and Figure 4.11 show that while aperture measurement error increases with increasing dip, since there are more opposing profile points in joints with higher dips, the length of consecutive opposing pairs with errors within a small limit remains almost constant.

Figure 4.12 shows the results for a case with a dip of 45^{o} and a borehole radius of 76 mm. The only difference in the results, in comparison to the cases with a smaller borehole radius, is the increase in the cumulative distance between consecutive opposing pairs with errors close to zero.

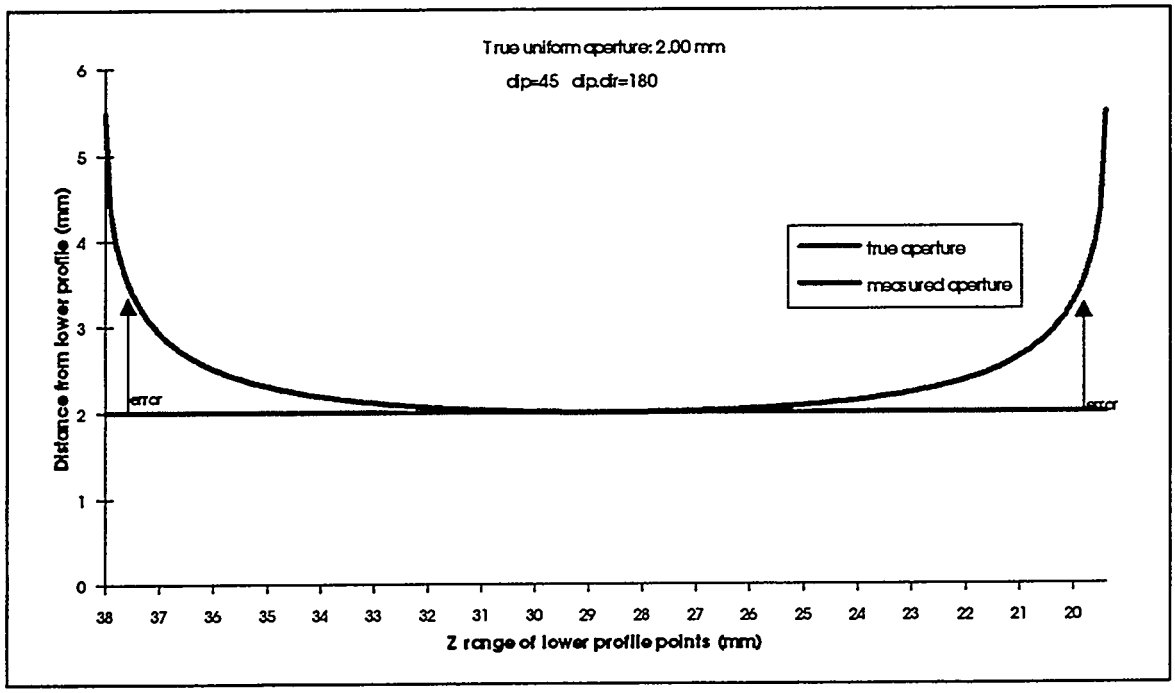

Figure 4.10: Synthetic aperture measurement errors for 45^{o} dip

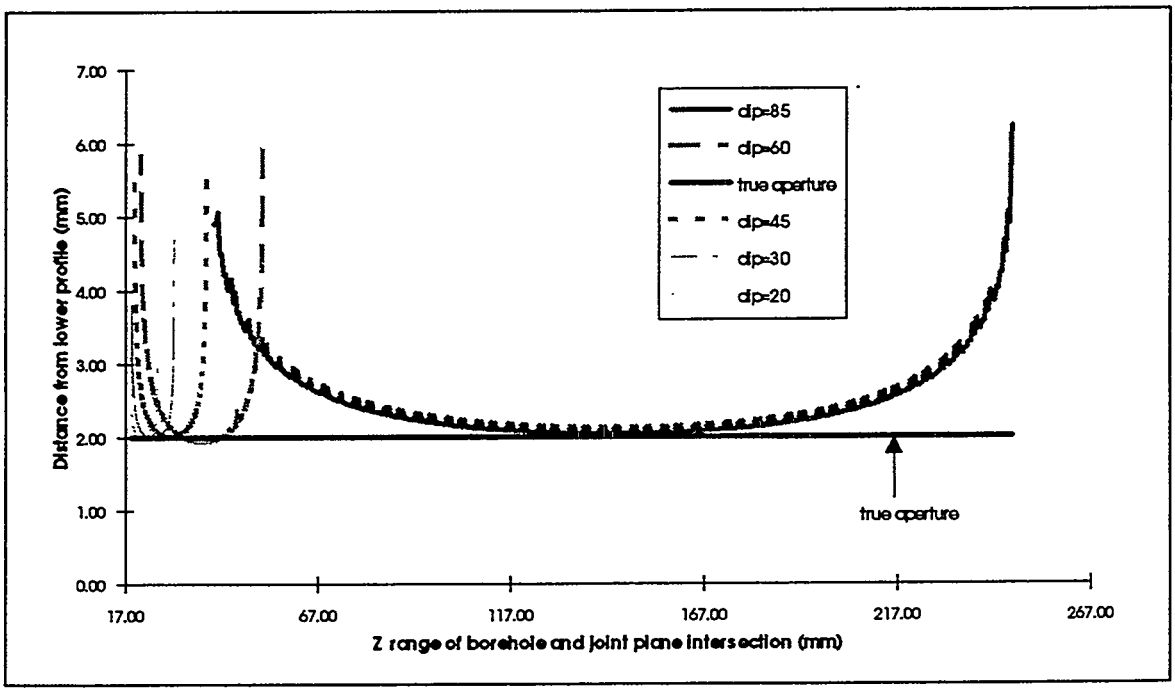

Figure 4.11: Synthetic aperture measurement errors for all dips

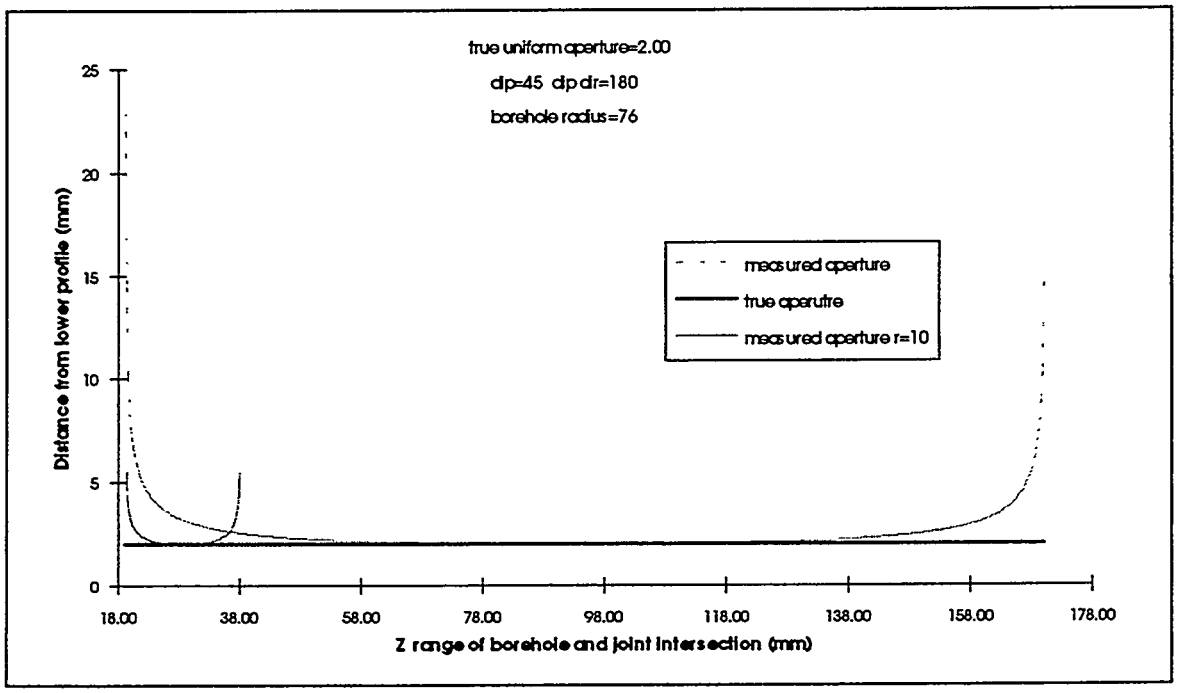

Figure 4.12: Synthetic aperture measurement errors for a large borehole

4.4.1.2 Apertures and measurement errors on joints in borehole 3-5

The method of pairing opposing profile points of the real joint profiles from BSS images is the same as the procedure described above for the synthetic experiment except for two differences. The first difference is that in the case of the real data, point p is found first using the intersection of plane G with the upper profile data. Plane G is found using Eqn. (4.3). Then point a is found using Eqn. (4.2), where the distance d is calculated as the distance between the mean orientation plane passing through point p and a parallel plane passing through point o. The other difference in the aperture analysis for the real data in comparison to the synthetic data is that the pairing is done for all lower profile points on both sides of the dip direction vector. This is because unlike the synthetic data, which was symmetric about the dip direction vector, the real data is generally not symmetric about the dip direction vector. Note that the computed error vector is only an estimate of the true error.

The procedure for pairing opposing profile points and finding apertures of real BSS profiles was coded in a program. Synthetic upper and lower profiles generated for smooth joints, separated by a constant true aperture of 3.54 mm, were piped to the program for verification. The smooth joint had a dip of 45^{o} towards 270^{o}. The aperture measurements produced by the program are given in Appendix H. As expected, the measurement errors are highest in the dip direction and lowest along the strike directions. When the error is close to zero, the measured aperture is very close to the true aperture.

Apertures of joint 13-1 from borehole 3-5 were analyzed using the program for pairing opposing profile points of real BSS data. Joint 13-1 dips 20^{o} towards 254^{o}. Figure 4.13 shows the result of this analysis. The estimated measurement errors are usually less than 2 mm and the apertures range from 1 mm to about 8 mm. As expected, the apertures and estimated measurement

errors in the dip and reverse directions are unusually high. The scanner resolution, about 0.5 mm here, can be used as the upper limit of acceptable error for aperture measurements. Examples of aperture measurements of other joints in borehole 3-5 are presented in Appendix I.

4.4.2 Unrolling procedure

As mentioned before, it is desirable to transform the BSS opposing profiles into a two dimensional sample for mechanical analysis of joint shearing strength. This transformation utilizes the pairing of opposing profile points described in the last section.

The transformation of the BSS profiles is done with respect to a reference datum plane placed below the lowest profile point on the lower profile. This datum plane has the same orientation as the mean orientation plane of the joints. Pairs of opposing profile points are projected onto the datum plane along the normal direction of the datum plane to find the ordinates of the unrolled opposing profiles:

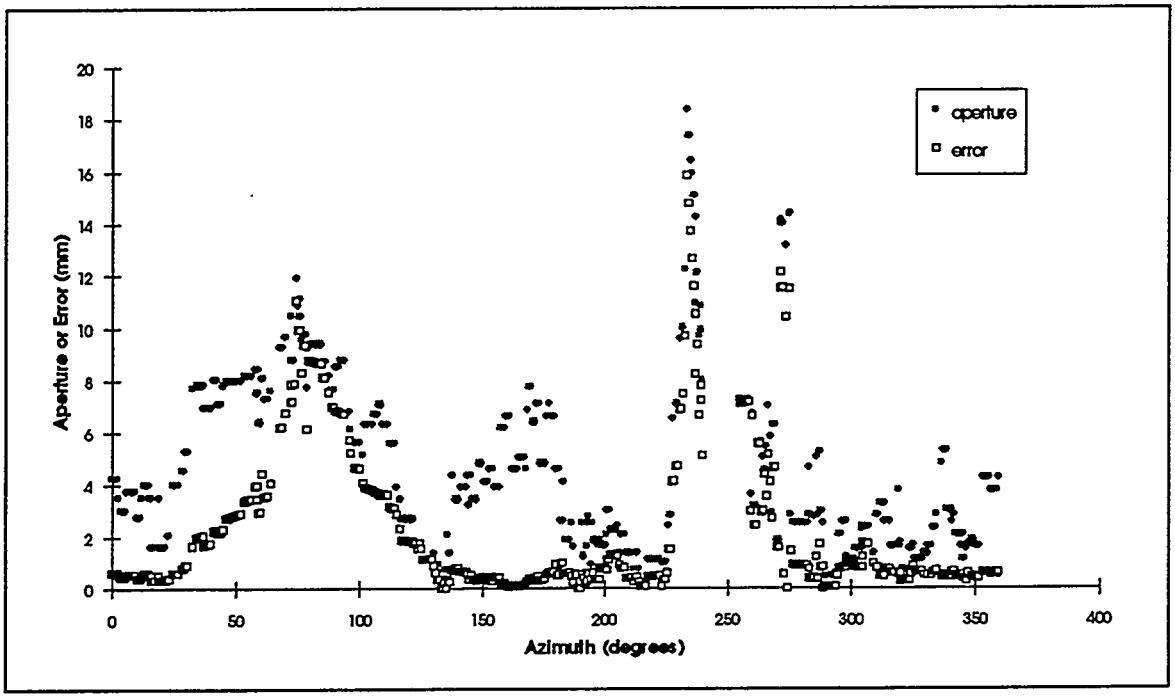

Figure 4.13: Apertures and measurement errors for joint 13-1

$$y_l = \frac{\left\| \bar{n} \bullet \bar{d} \right\|}{\left\| \bar{n} \right\|}$$

$$y_u = y_l + \left\| \bar{n} d \right\| \qquad (4.9)$$

where y_l and y_u are the upper and lower abcissa respectively, $\bar{n}$ is the joint normal, $\bar{n}_d$ is the aperture for the pair and $\bar{d}$ is a vector between the lower profile point of the pair and the lowest point on the lower profile

The location of the first opposing profile pair's projection on the datum plane defines the origin of the two dimensional sample. The distance between consecutive projection points on the datum plane is the increment along the abscissa:

$$\Delta x = \left\| \overline{d}_{ij} \right\| \qquad (4.10)$$

where Δx is the increment along the abcissa between two consecutive projection points i and j and $\overline{d}_{ij}$ is the vector between these points. Consecutive Δx increments are summed during each projection of opposing profile pairs to produce a series of triplets (x, y_l, y_u) that comprises the unrolled two dimensional sample of the joint. The estimated error from pairing opposing profiles can be used to decide to include only those pairs having errors less than a prescribed value in the unrolling. Any lower profile point can be chosen as the first point for unrolling. The lowest lower profile point in the decreasing azimuth direction having an acceptable pairing error is used as the initial point in the unrolling procedure here. Regardless of which point in the lower profile is chosen as the initial unrolled sample point, there will be at least one discontinuity in the unrolled sample. The first discontinuity occurs in the unrolling of opposing pairs towards the dip direction. As explained in Section 4.4.1.1, the aperture measurement error will be very high in the dip direction. Usually, this error will usually be larger than the tolerance used in accepting opposing pairs for the unrolling. Thus a series of consecutive opposing pairs will be skipped and the unrolled profile will have a large x increment. For instance, in a case where the mean plane dips 45^{o} towards 270^{o}, opposing pairs from 268^{o} to 272^{o} may be skipped and pairs from 267^{o} and 273^{o} may be connected as consecutive unrolled profile points. The second discontinuity in the unrolled profile occurs in the direction opposite to the dip direction for the same reason as in the case of the discontinuity in the dip direction. One of these two discontinuities can be avoided by starting the unrolling at either side of the dip direction vector. The unrolling is started so as avoid the first discontinuity here.

The procedure described above was coded in a program for pairing opposing profile points and unrolling the opposing profiles. The test joint dipping at 45^{o} towards 270^{o} described in Section 4.4.1.2 for verifying the aperture measurement part of this same program was used again to verify the unrolling part. The unrolled opposing profiles produced by this program are shown in Appendix H. As expected, the unrolled profiles are straight lines separated by a constant aperture of about 3.54 mm. The large gap in the data between 39 mm and 120 mm is due to the discontinuity discussed earlier in the direction opposite to the dip direction. The discontinuity is very large here because the dip of the test joint is fairly high.

The unrolling of opposing BSS derived roughness profiles is valid only at scales at which the roughness profile is isotropic. Since scale represents the displacement distance during shearing, unrolled roughness profiles provide a valid sample for shear displacement analysis up to a limiting displacement defined by the largest scale at which the joint is found to be isotropic. This limit has to be established using the anisotropy analysis program as discussed earlier.

4.4.3 Unrolled profiles for borehole 3-5 joints

Unrolled profiles for joints in borehole 3-5 were obtained using unroll.c. Figure 4.14 shows the unrolled profile for joint 13-1 at an acceptable aperture measurement error level of 2 mm. Decreasing the acceptable error leads to a smoother profile, as fewer opposing pairs are included in the unrolled profiles. The magnitude of the pairing errors are also shown below the profile points in Figure 4.14. The discontinuity in the direction opposite to the dip direction occurs around 160-225 mm along the abscissa. Examples of unrolled profiles for other joints from borehole 3-5 are presented in Appendix J. One of these unrolled profiles can be obtained using the program discussed above on a 486

compatible PC in about 10 minutes once the roughness profile discussed in Chapter 3 is available.

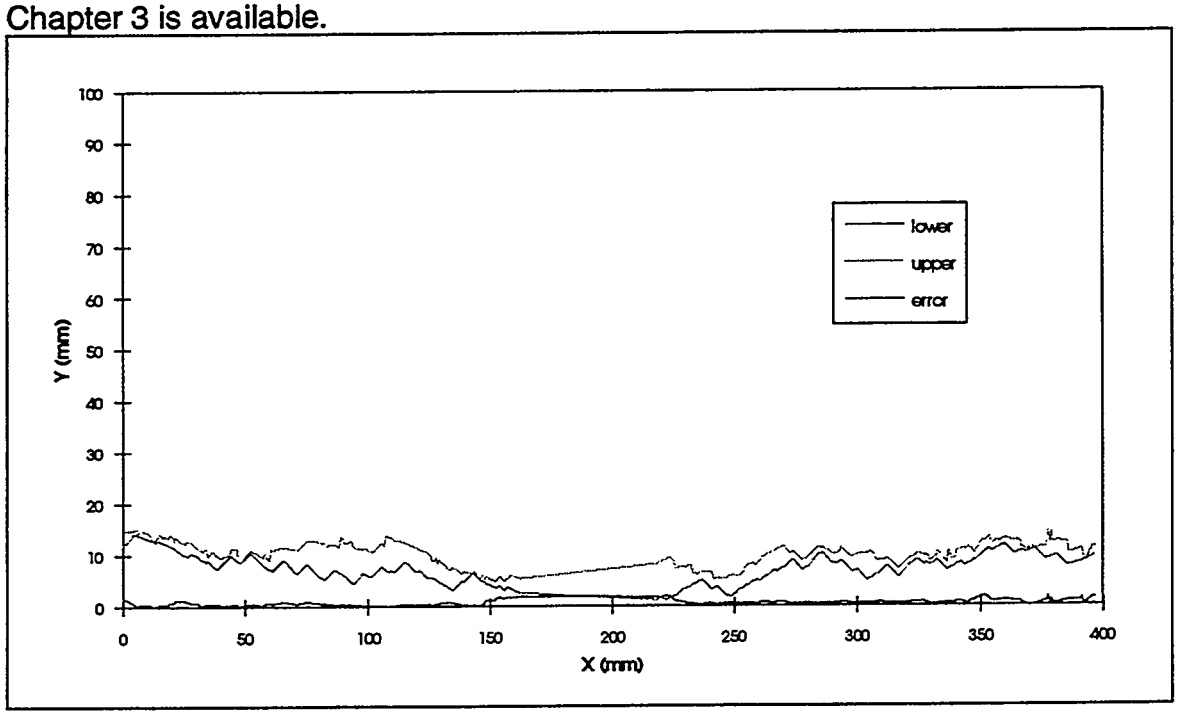

Figure 4.14: Unrolled opposing profiles for joint 13-1

CHAPTER 5

ANALYSIS OF SHEAR DISPLACEMENT BEHAVIOR

5.1 Kinematic displacement dilation analysis

As discussed in Section 4.2.1, joint roughness profiles control peak shear strength and volume change behavior during shear displacement under low normal stress conditions. A new analysis for these joint characteristics utilizing opposing joint profiles is described in this chapter. The new analysis is applied to in-situ BSS opposing joint profiles.

5.1.1 Background

A method of deriving the dilatancy and shear stress-shear deformation curves, using Rengers envelope, for a perfectly mated joint was described by Schneider (1976). Schneider's method is illustrated in Figure 5.1. The dilatancy curve locus is defined by

$$v = u * \tan i(u) \qquad (5.1)$$

where u is the displacement, $i(u)$ is the dilation angle at u, and v is the dilation at u.

The shear stress-shear deformation curve is constructed using

$$\tau(u) = \sigma \tan\left[\phi_r + i_{\tan}(u)\right] \qquad (5.2)$$

where $i_{\tan}(u)$ is the inclination of the tangent to the dilatancycurve at u, ϕ_r is the residual friction angle, σ is the normal stress across the joint and $\tau(u)$ is the shear stress at u.

In order to evaluate the accuracy of Schneider's method, an alternate dilatancy curve for the roughness profile of Figure 5.1 was constructed by hand, tracing the actual dilatancy of a plastic model of the upper block during right lateral shearing. The model used in this kinematic simulation of joint shearing consisted of blocks cut out of plastic separated by the roughness profile shown in Figure 5.1. Only displacements parallel and perpendicular to the mean joint plane were allowed during the simulated shearing process -- no rotation occurred. The results from this simulation are presented in Figure 5.2 and Figure 5.4 along with the results of Schneider's analysis.

Figure 5.2 shows that the dilatancy curve from Schneider's method agrees with the simulated dilatancy curve over most of the displacement range (i.e. from 0 to 15 mm). As long as the basic assumption that the maximum dilation angle (as given in Rengers envelope) at any displacement controls dilation is true, Schneider's method produces accurate results. This assumption holds when the opposing profiles are perfectly mated, but is generally violated when apertures are not zero along the entire length of the opposing profiles, regardless of whether the opposing profiles are mirror images of each other or not. The dilatancy curves for the non-mated upper profiles P_1, P_2 and P_3 in Figure 5.2 illustrate this fact. Figure 5.3 shows the upper profiles P_1, P_2 and P_3. The lower profiles for all the cases shown in Figure 5.2 are the same as the profiles of the perfectly mated case shown in Figure 5.1. The upper profiles P_1, P_2 and P_3 consist of two spikes each located at different spacings. By carrying out the kinematic shear displacement simulation for the three unmated cases of Figure 5.2, it was observed that the location and amplitude of the upper profile spikes determine which asperities of the lower profile may influence dilation as displacement proceeds. The resulting asperity sampling sequence is not constrained to follow the pattern of Rengers envelope with increasing

displacement increments and infact does not do so for the unmated cases plotted in Figure 5.2. Thus, Schneider's method is not able to account for the dilatancy of unmated opposing profiles.

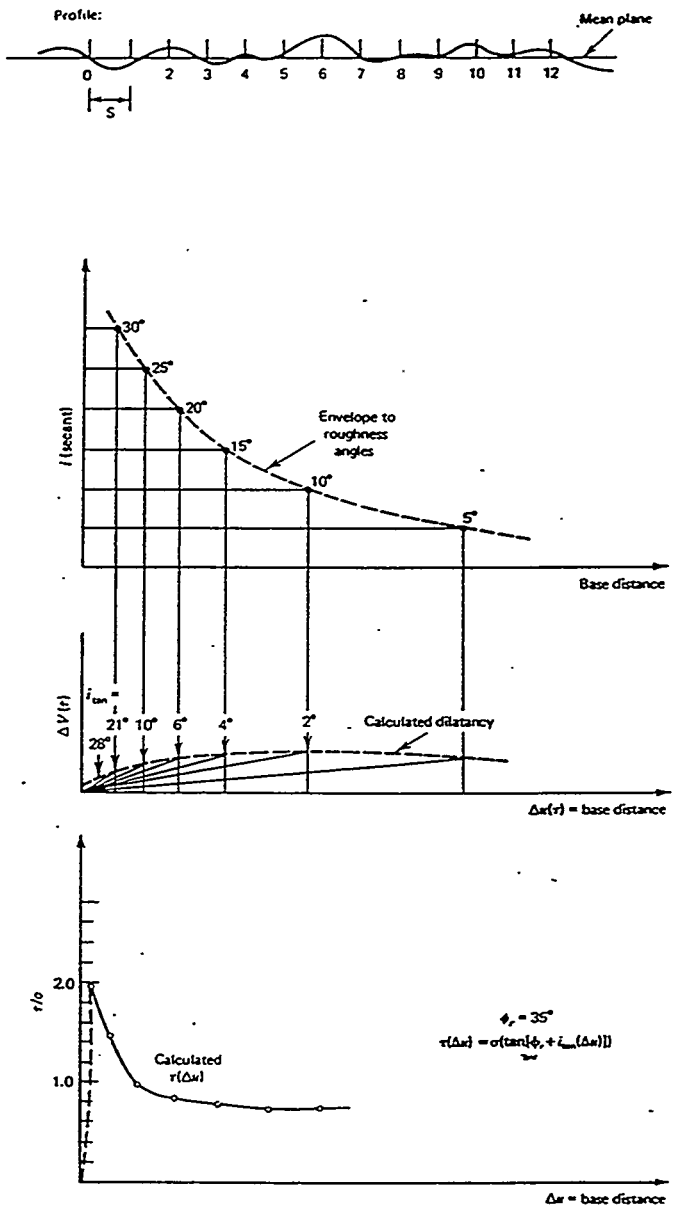

Figure 5.1: Schneider's method of constructing dilatancy and shear-stress shear deformation curves (after Goodman, 1989)

Figure 5.2: Comparison of simulated and calculated dilatancy curves

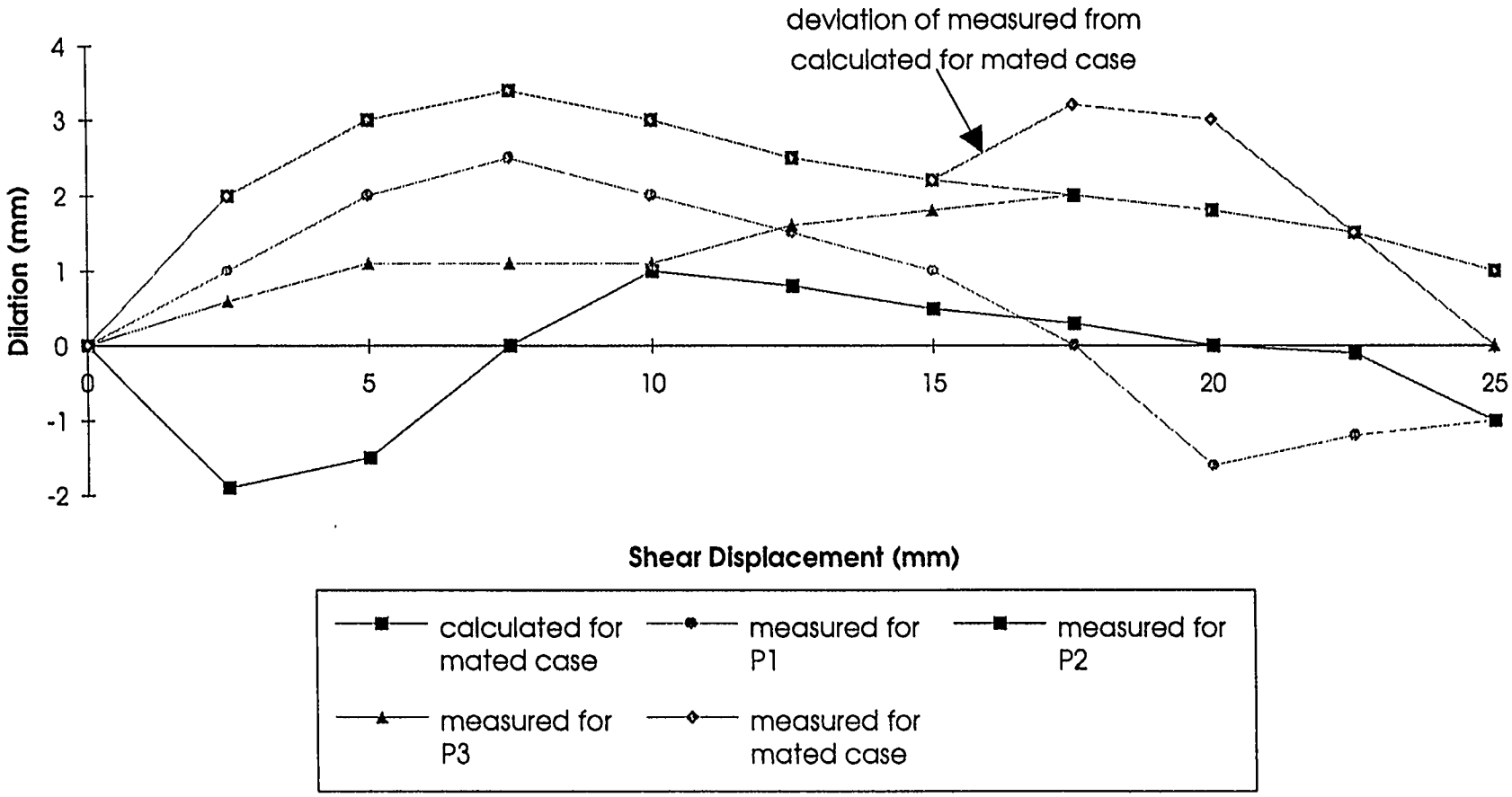

The sampling scheme that defines which lower profile points may influence the dilatancy over the next increment of displacement is determined by the geometry of the opposing profiles, i.e. the contact points. When the opposing profiles are perfectly mated, the upper profile samples all points on the lower profile. In this case, since the entire lower profile is available for sampling, the lower profile slope that determines the dilatancy rate over the next displacement increment will be the same as the roughness angle in Rengers envelope,

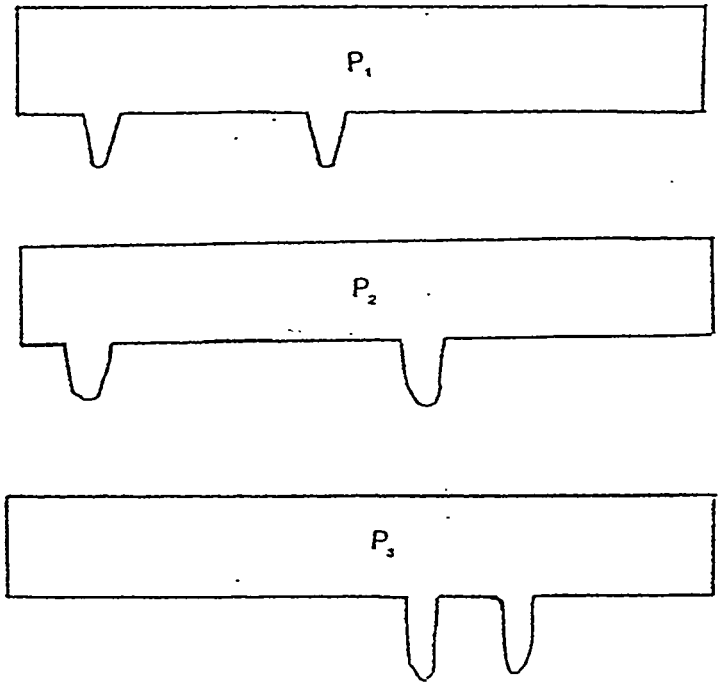

Figure 5.3: Unmated upper profiles

provided the displacement increment is small. In contrast to the perfectly mated case, if the upper profile consisted of only one spike, the dilatancy curve would be a reproduction of the roughness profile. Two spikes on the upper profile produce a dilatancy curve determined by the larger of the two asperity slopes sampled by the upper profile at successive displacements. Similarly, dilatancy in

real joints will be the result of samples of lower profile slopes at all contacting points at each displacement increment.

The kinematic simulation experiment using unmated profiles also showed that the rate of dilatancy at each increment of displacement (and hence the dilatancy curve as well) is equal to the steepest slope among slopes of lower profile points sampled by the upper profile at each increment of displacement. Thus, Eqns. (5.1) and (5.2) are replaced by the following expressions which work with mated and unmated opposing profiles:

$$i(u) = \max\left[\frac{dy}{dx}\right] \forall\, x \text{ where } a = 0 \qquad (5.3)$$

where $\frac{dy}{dx}$ is the slope of the lower profile and at x and a is the aperture at x. Note: the symbol $\forall$ means 'for all.'

$$v(u) = \max\left[\frac{dy}{dx}\right] du \qquad (5.4)$$

where $\max\left[\frac{dy}{dx}\right]$ is evaluated at all x where $a = 0$ and du is the displacement increment.

$$\tau(u) = \sigma\left\{\tan\phi_r + \max\left[\frac{dy}{dx}\right]\right\} \qquad (5.5)$$

where $\max\left[\frac{dy}{dx}\right]$ is evaluated at all x where $a = 0$.

Eqn. (5.3) disagrees with the comparison of Rengers dilation angles and the tangent to the dilation curve in Figure 5.1 since this figure shows these angles to be unequal. The reason for the disagreement is because the dilation angles

measured in constructing Rengers envelope are considered to apply at the end of the displacement distance connecting points on the concave roughness profile shown in Figure 5.1. The concavity of the roughness profile makes the actual dilation angle at the end of the displacement distance smaller than the calculated dilation angle. Thus the tangent to the dilation curve in Figure 5.1 is lower than the dilation angle shown in Rengers envelope for that displacement. At large displacements the disagreement is also influenced by the unmated dilatancy behavior described above.

The results shown in Figure 5.2 show that changes in the opposing profiles can cause changes in the amount of dilation and the displacement at which peak dilation occurs. For instance, in the case of upper profile P_2, the initial location of the spikes on parts of the lower profile having negative slopes results in contraction up to a displacement of 7.5 mm. The maximum dilation developed by P_2 is only 1 mm compared to the peak dilation of 3.4 mm in the case of the perfectly mated joints. Also, the peak dilation of P_2 occurs at a displacement of 10 mm while the perfectly mated joints show a peak dilation at 7.5 mm.

Figure 5.2 shows that the dilation curve for the perfectly mated case is an envelope to all other unmated cases. This follows from the preceding discussion of how the perfectly mated joint can take advantage of the highest roughness angle possible while unmated joints may not be able to do so. In other words, the perfectly mated upper profile utilizes the full dilation potential offered by the lower surface. The perfectly mated joint will always be the envelope to unmated joint dilation curves. Thus the perfectly mated joint is always the strongest in terms of strength due to dilatancy. Grouting an unmated joint such that apertures are reduced to zero raises joint strength by forcing maximum dilatancy from the joint. Alternately, if all apertures are not reduced to zero, the effectiveness of grouting

can be evaluated by analyzing the increase in dilatancy or shear strength caused by changes in the opposing profiles and apertures due to grouting. The analysis can be done using the method described in the next section.

The shear stress-shear displacement curves for the mated and unmated cases described above are shown in Figure 5.4. The curves in Figure 5.4 were constructed using Eqn. (5.3) with $\phi_r = 35^0$. The peak value of $i_{\tan}$ decreased, in comparison to the perfectly mated case, by 7% for P_1, by 0% for P_2 and by 60% for P_3. The reason P_2 had the same $i_{\tan}$ value as the perfectly mated case is that the location of the spikes in P_2 happened to sample the asperity on the lower profile having the largest slope. This did not happen in the other unmated cases and hence the loss in peak strength. Thus, the peak strength of unmated joints may be significantly lower than that predicted by Schneider's method using a single profile. Engineering design based on a peak shear strength given by Eqn. (4.1) should be based on $i(u)$ from Eqn. (5.3) instead of Rengers envelope to avoid overestimating the dilation angle.

5.1.2 Improved method using opposing joint roughness profiles

A new procedure of analyzing dilatancy and shear stress-shear deformation behavior can be developed utilizing the findings of the kinematic shearing experiment. This new procedure assumes there is no shearing through joints and that there is no rotation about the mean joint plane during shear displacement. The procedure is as follows:

(1) Find the aperture at all opposing profile points.
(2) At each opposing profile point where $a = 0$, find $i(\Delta u)$ using Eqn. (5.3) for the shearing direction of interest.
(3) Increment displacement by Δu and compute new coordinates of all upper profile points as

$$\left(x_i\right)_{u+\Delta u} = \left(x_i\right)_u + \Delta u \quad \forall \quad i = 1..n \qquad (5.6)$$

$$\left(y_i\right)_{u+\Delta u} = \left(y_i\right)_u + \Delta u * \tan i(u) \quad \forall \quad i = 1..n \qquad (5.7)$$

where $\left(x_i, y_i\right)$ is point i of the upper profile and n is the total number of upper profile points.

(4) Repeat steps 1-3 up to the desired displacement distance. The value of $i(\Delta u)$ used at each increment is stored for calculating the dilatancy curve using Eqn. (5.4) and the shear stress-shear deformation curve using Eqn. (5.5).

(5) If the aperture becomes greater than zero everywhere along the opposing profiles during any displacement increment, the upper profile is lowered parallel to the mean joint plane until atleast one point has an aperture of zero. This adjustment is realistic as the normal stress will almost always be large enough to make this happen in reality.

This new procedure was coded in a program. The procedure described above was modified slightly to minimize interpenetration errors caused by discretizing the analysis. Figure 5.5 shows a discrete representation of opposing profiles. The upper profile will dilate along the dilatancy path between lower profile points 4 and 5 during right lateral shearing as shown in Figure 5.5. All upper profile points follow this dilatancy path including the upper profile point 3. If the dilatancy path is followed over the entire increment of Δu by upper profile point 3, that point will cause an interpenetration error at the end of the Δu increment by intersecting the lower block below the location of lower profile point

Figure 5.4: Comparison of shear stress-shear deformation curves for mated and unmated opposing profiles

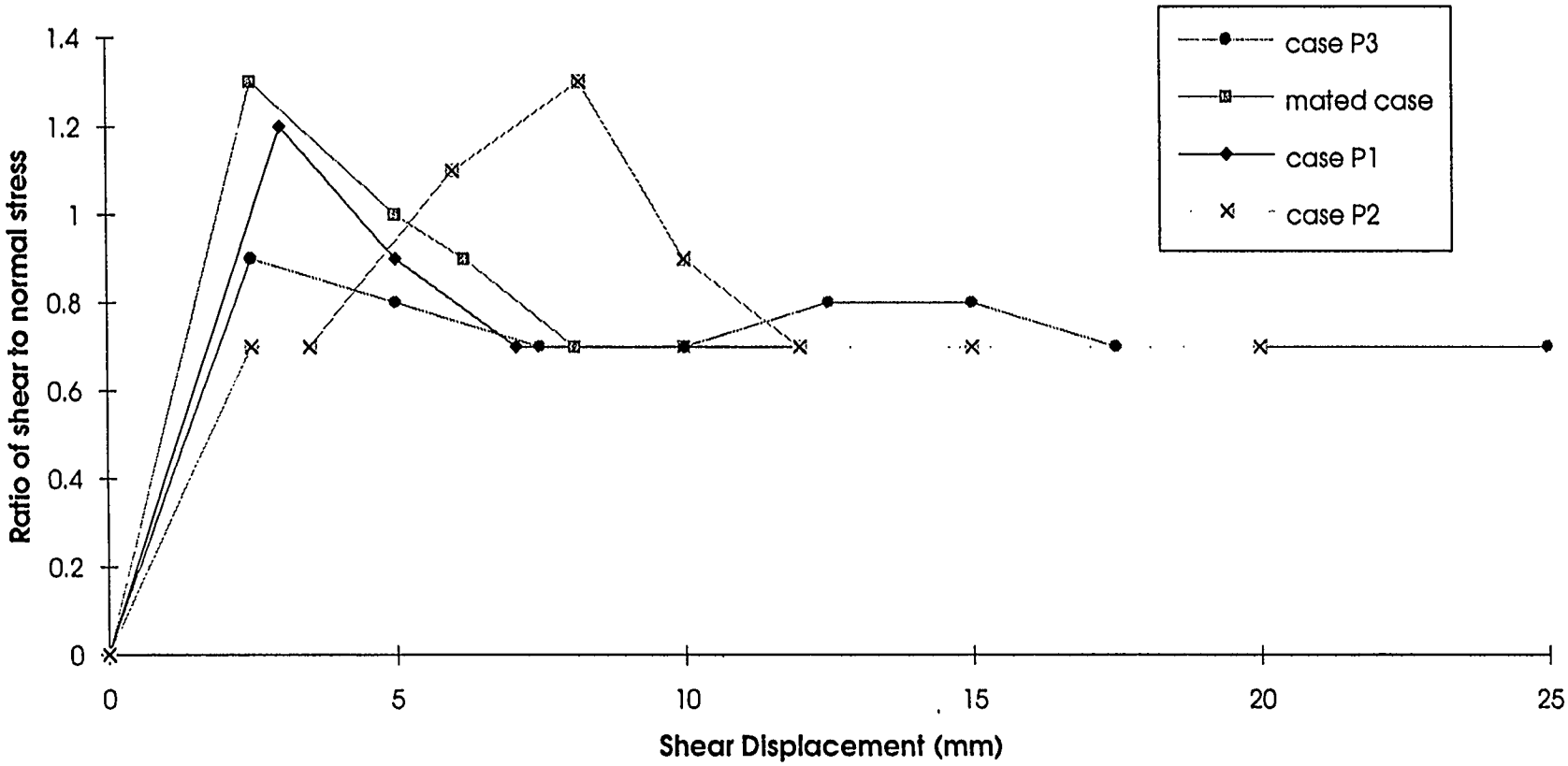

4 as shown in the figure. This interpenetration error is purely the consequence of discretizing the upper and lower joint walls into points separated by Δu. To avoid this error, the dilatancy path can be followed from point 3 up to point 'a' and then the path can be switched to the interpolated profile between lower profile points 3 and 4. Also, the discretization error can be reduced, and may be avoided altogether, by decreasing the size of the Δu increment. For instance, in Figure 5.5, if Δu were reduced to the distance between lower profile points 3 and 'a', there would be no interpenetration by upper profile point 3, if the finer lower profile followed the interpolation between lower profile points 3 and 4 shown in Figure 5.5.

The discretization error can be detected during any displacement increment by finding the distance to the intersection point ('a' in Figure 5.5) from where the interpenetration error starts to accumulate:

$$u_i = \frac{a_i}{m_{lp} - \tan i(\Delta u)} \qquad (5.8)$$

where u_i is the displacement distance from point i at which the interpenetration error begins to accumulate $\left(u_i \le \Delta u\right)$, a_i is the aperture at point i, and m_{lp} is the interpolated slope between point i and i+1.

If $u_i \ge \Delta u$ between any pair of consecutive points, the algorithm follows the procedure described previously. However, if an interpentration error is detected (i.e. if $u_i < \Delta u$ between any pair of consecutive points), the algorithm makes a correction to the usual procedure by using m_{lp} between u_i and Δu instead of $i(\Delta u)$. This correction is made using the m_{lp} corresponding to the smallest value of u_i, if more than one pair of consecutive profile points cause an interpenetration error during any increment of displacement.

The algorithm was tested using opposing profiles consisting of the lower profile of Figure 5.1 and the upper profile P_2 shown in Figure 5.3. These profiles were discretized using a sampling interval of 1 mm. Figure 5.6 shows the dilatancy curves computed using the algorithm and using a hand simulation of the shear displacement behavior. Figure 5.6 shows that the algorithm produces results which are very close to those from the physical simulation of dilatancy. Unlike the dilatancy curve obtained using Schneider's method, shown in Figure 5.2, the new algorithm described here captures the initial contractile behavior of this joint. The small discrepancies between the two curves are most likely due to the linear interpolations used in the new algorithm when correcting for discretization errors.

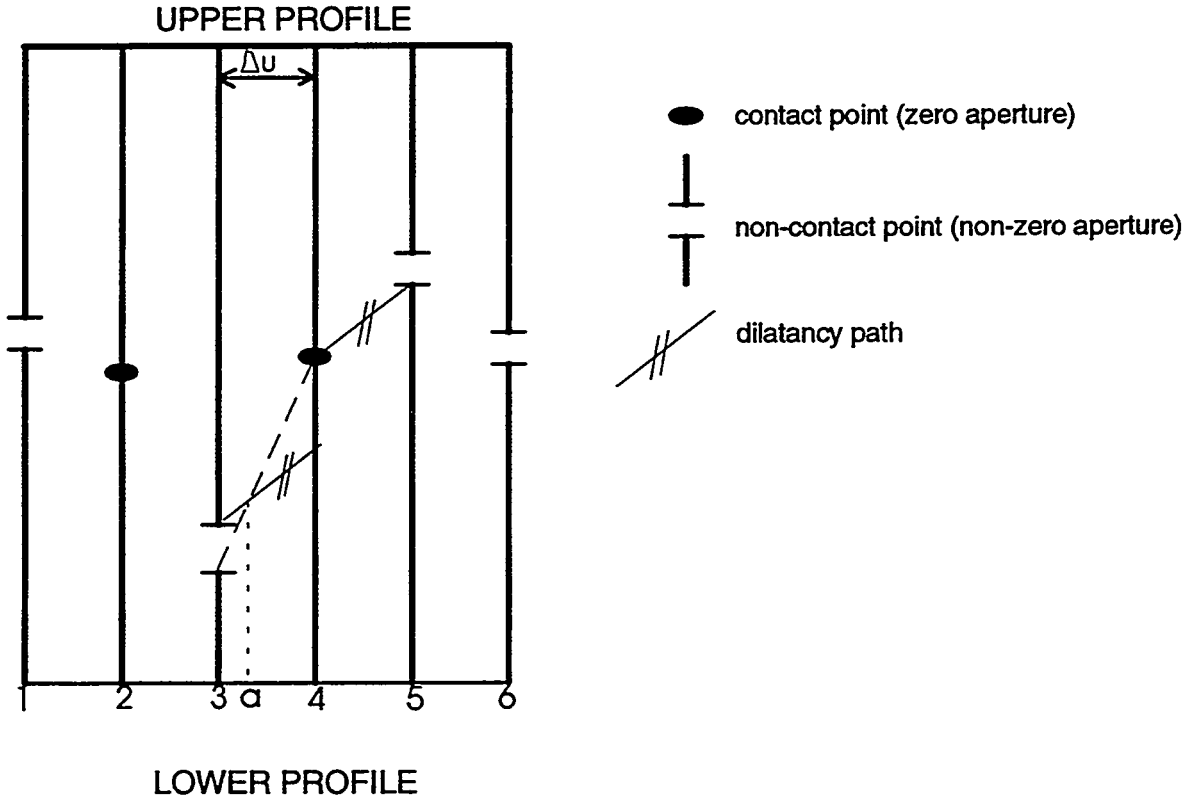

Figure 5.5: Discrete representation of opposing profiles

5.1.3 Application to borehole 3-5 joint 13-1

The program using the new algorithm described in the last section was applied to the unrolled opposing profiles obtained using the method described in Section 4.4.2 for joint 13-1 of borehole 3-5. Figure 5.7 shows the dilatancy curve and Figure 5.8 shows the shear stress-shear deformation curve produced by the program for a displacement distance of 23 mm. The dilatancy curve in Figure 5.7 has the characteristic concave shape with the rate of dilatancy decreasing as shear displacement proceeds. The shear stress-shear deformation curve of Figure 5.8 shows the ratio of shear stress to normal stress to be within a reasonable value of 1.4. The multiple peaks shown in Figure 5.8 are the result of the upper profile being dropped to meet the lower profile each time the opposing profiles loose contact and because asperity shearing is not accounted for.

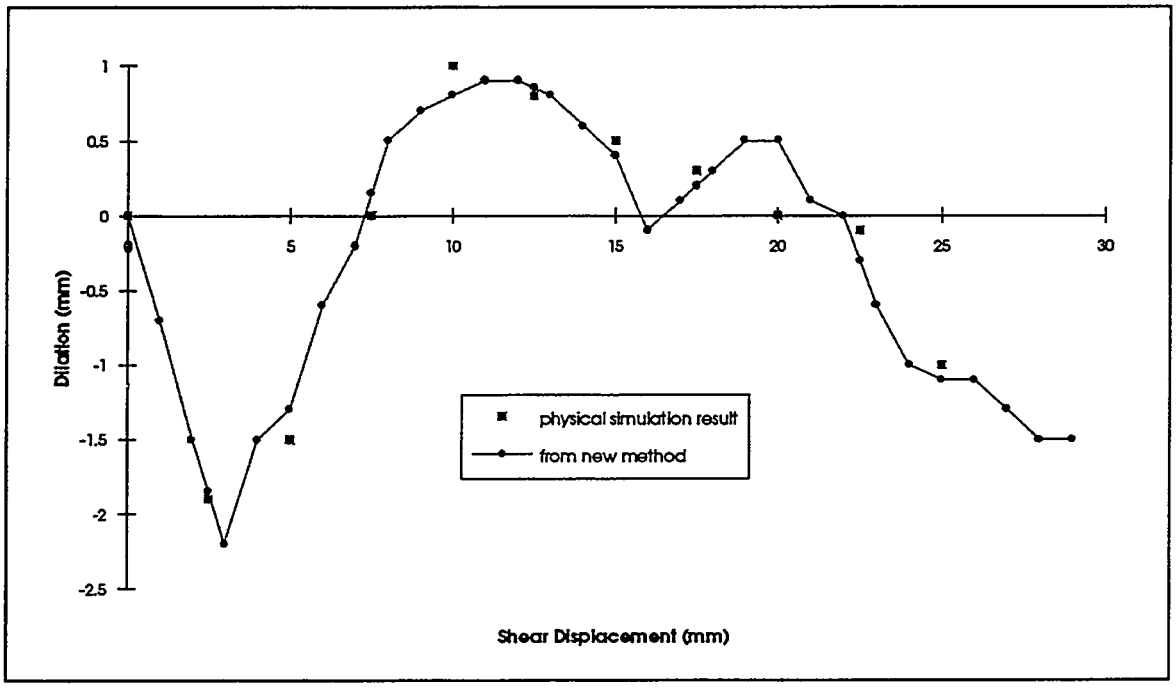

Figure 5.6: Comparison of dilatancy curves from new method and physical simulation

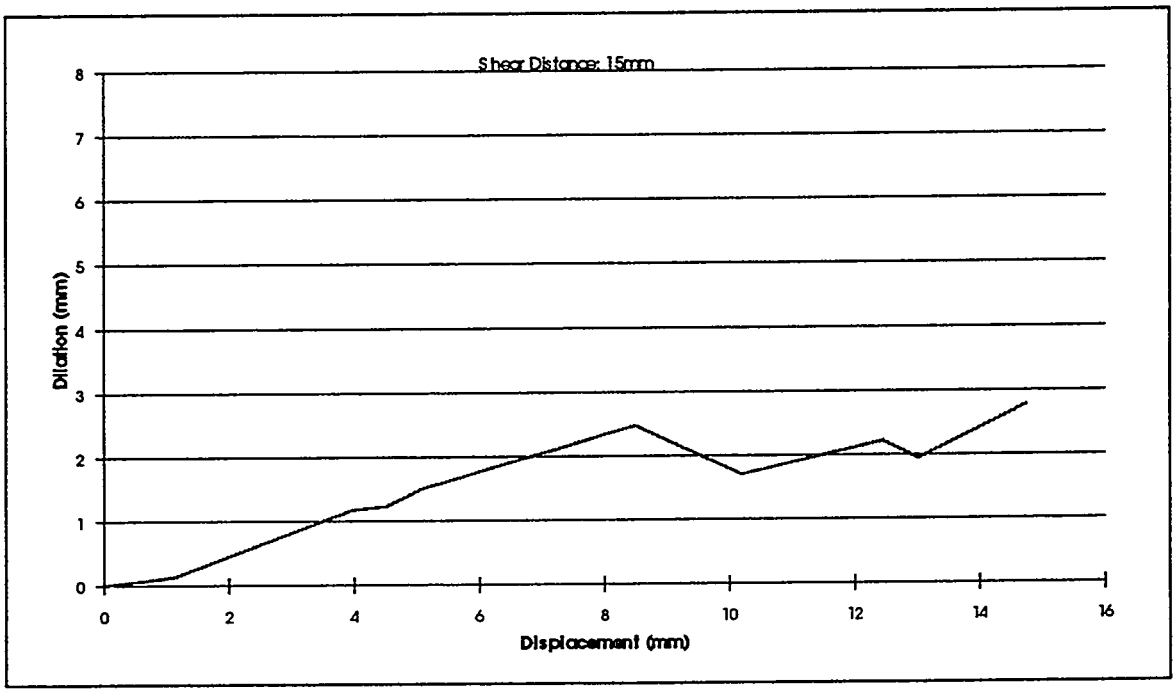

Figure 5.7: Dilatancy curve for joint 13-1 of borehole 3-5

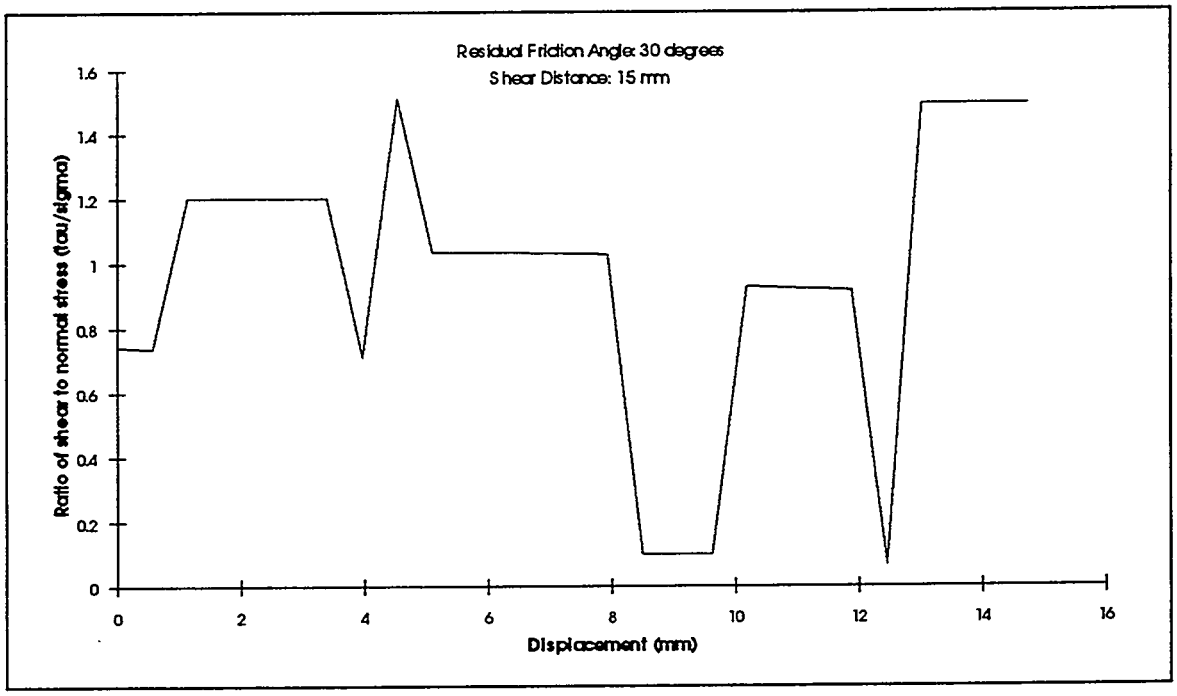

Figure 5.8: Shear stress-shear deformation curve for joint 13-1 of borehole 3-5

5.2 Numerical Simulation of a Direct Shear Test using Discontinuous Deformation Analysis

The kinematic shear deformation analysis described in the previous section cannot account for the mechanical interaction of the opposing profiles and shear displacement rate. This section describes a way to overcome these limitations of the kinematic analysis using Discontinuous Deformation Analysis (DDA).

5.2.1 Background on DDA

DDA is a numerical analysis for simulating the statics and dynamics of a two-dimensional rock block systems developed by Shi(1985). The displacement of a point (x,y) within a block are given by:

$$\begin{pmatrix} u \\ v \end{pmatrix} = \begin{pmatrix} 1 & 0 & -(y-y_o) & (x-x_o) & 0 & (y-y_o)/2 \\ 0 & 1 & (x-x_o) & 0 & (y-y_o) & (x-x_o)/2 \end{pmatrix} \begin{pmatrix} u_o \\ \upsilon_o \\ r_o \\ \varepsilon_x \\ \varepsilon_y \\ \gamma_{xy} \end{pmatrix} \qquad (5.9)$$

where (u,v) is the total displacement of point (x,y), (x_o,y_o) is the block centroid, (u_o,v_o) is the displacement of the centroid, r_o is the rotation about (x_o,y_o), and $\varepsilon_x,\varepsilon_y,\gamma_{xy}$ are the normal and shear strains of the block.

Equilibrium equations of a system of blocks are found by minimizing the total potential energy, Π

$$\frac{\partial \Pi}{\partial d_{ri}} = 0, \qquad r = 1,...,6 \qquad (5.10)$$

where d_{ri} is the deformation variable for block i.

The resulting system of equations have the form

$$\begin{pmatrix} K_{11} & K_{12} & K_{13} & .... & K_{1n} \\ K_{21} & K_{22} & K_{23} & .... & K_{2n} \\ . & . & . & . & . \\ . & . & . & . & . \\ K_{n1} & K_{n2} & K_{n3} & .... & K_{nn} \end{pmatrix} \begin{pmatrix} D_1 \\ D_2 \\ . \\ . \\ D_n \end{pmatrix} = \begin{pmatrix} F_1 \\ F_2 \\ . \\ . \\ F_n \end{pmatrix} \qquad (5.11)$$

Displacements and strains during each time step are found by solving the system **KD=F**. The FORTRAN version of DDA used here was developed by Ke (1993). The DDA formulation assumes the strains within each block are constant.

5.2.2 Description of the DDA direct shear test configuration

The unrolled opposing BSS profiles were used in a DDA direct shear simulation as shown in Figure 5.9. A block was attached to each opposing profile and the shear stress was measured at a point on the left side of the upper block. The direct shear simulation was displacement controlled, i.e. increments of displacement were prescribed and the resulting shear stress computed. The upper and lower blocks were given very high values of Young's modulus to prevent elastic deformations of the blocks from causing higher shear stress values than predicted by limit equilibrium analysis for rigid blocks. The lower block was constrained by a roller and two fixed points as shown in Figure 5.9. A constant normal load was applied at the center of the upper block during the simulated test.

The DDA shear test was performed on a test case consisting of a perfectly mated saw-tooth profile as shown in Figure 5.10. A normal load of 1000 kN was applied at the center of the upper block (point 6). The lower block was constrained by fixed points 1 and 2 and a roller just below point 4. The

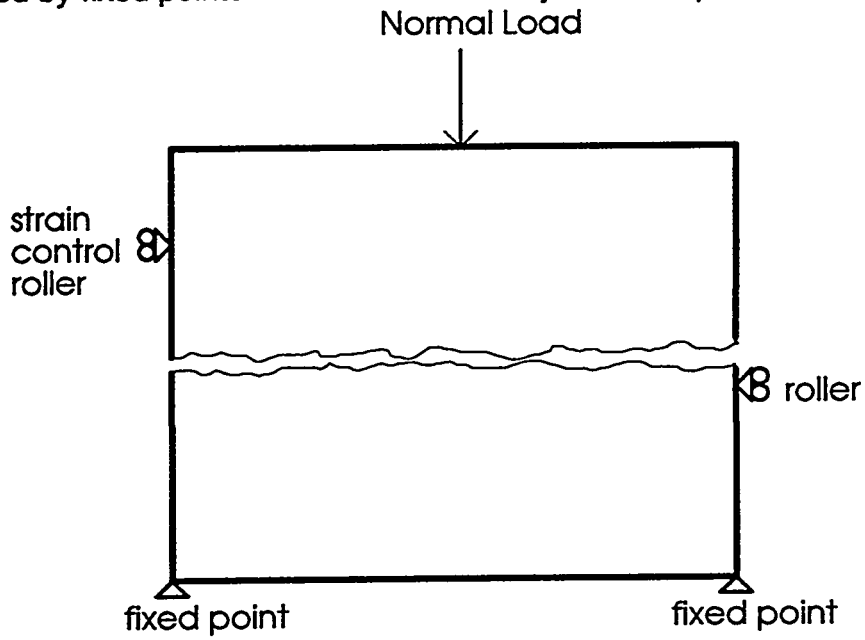

Figure 5.9: Configuration of DDA direct shear test

displacement of the upper block was measured by monitoring point 7 while the shear force was measured from the spring at point 3. The DDA result for this configuration was compared to limit equilibrium predictions based on Eqn. 4.1 as shown in Figure 5.11. The DDA result agrees with the limit equilibrium prediction except at a displacement of about 0.10 m. Here DDA's prediction of the shear force overshoots the limit equilibrium value, but soon drops down to the limit equilibrium value.

The DDA simulation was also performed assuming properties of joint 13-1 from borehole 3-5 and two additional joints from borehole 4-1. As reported in Table 4.1, the roughness of joint 13-1 is close to isotropic at small scales. Thus, the roughness profile of joint 13-1 may be unrolled to obtain a representative two

dimensional sample of the surface roughness. Table 5.1 shows the results of anisotropy analysis performed on the two joints 48-1 and 64-1 from borehole 4-1 used in the DDA direct shear simulation. Joints 48-1 and 64-1 can be expected to provide representative two dimensional surface roughness samples for the direct shear test simulation.

Table 5.1: Anisotropy of joints in borehole 4-1

Joint	Lower Profile Scales in mm			Upper Profile Scales in mm		
Label	2	8	14	2	8	14
48-1	I	NI	NI	I	NI	NI
64-1	I	NI	NI	I	NI	NI
A: anisotropic; I: isotropic; NI: nearly isotropic						

5.2.3 Test results and comparison to laboratory measurements

The configuration of the DDA direct shear test for joint 13-1 is shown in Figure 5.12. Only the unrolled profile of joint 13-1 from 150 mm to 396 mm was used in the test to avoid the high aperture measurement error segment as described in Section 3.4.2. A normal load on 1475 kN was applied at the center of the upper block. Figure 5.13 and 3.28 show the test results. Also shown in these figures are the results from laboratory direct shear testing of joint 13-1 in a core sample and results from the kinematic analysis described in Section 3.5. All three dilatancy curves in Figure 5.13 are close up to a shear displacement of about 2 mm. After that, the dilatancy curves from DDA and the kinematic analysis remain close to each other up to a displacement of 3.9 mm, but together diverge from the laboratory curve. This divergence is due to crushing of the asperities in the laboratory test. Neither DDA nor the kinematic analysis take asperity crushing into account and thus overestimate the dilatancy. As displacement proceeds, the kinematic analysis curve predicts a nearly constant

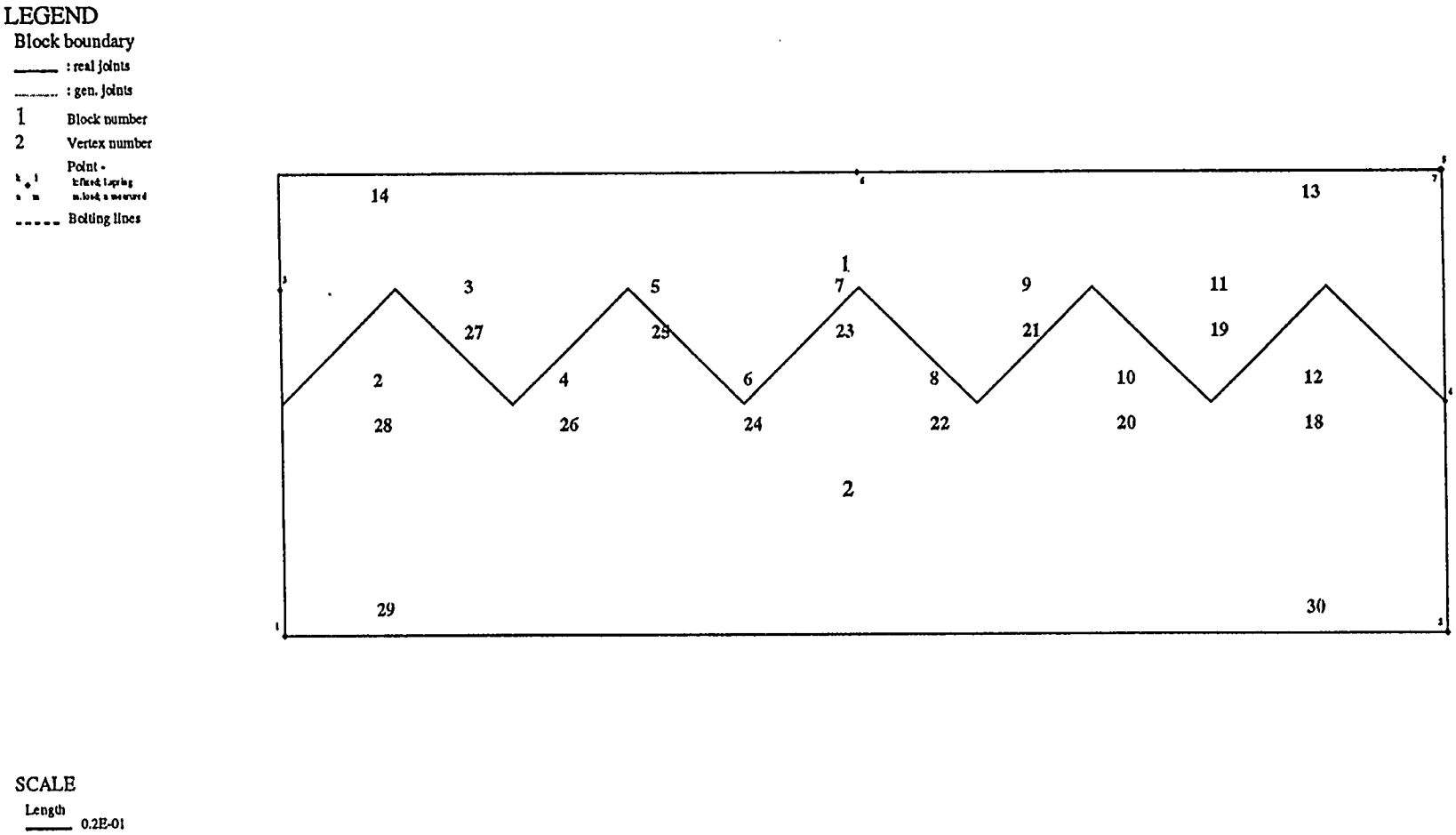

Figure 5.10: Configuration of DDA shear test case

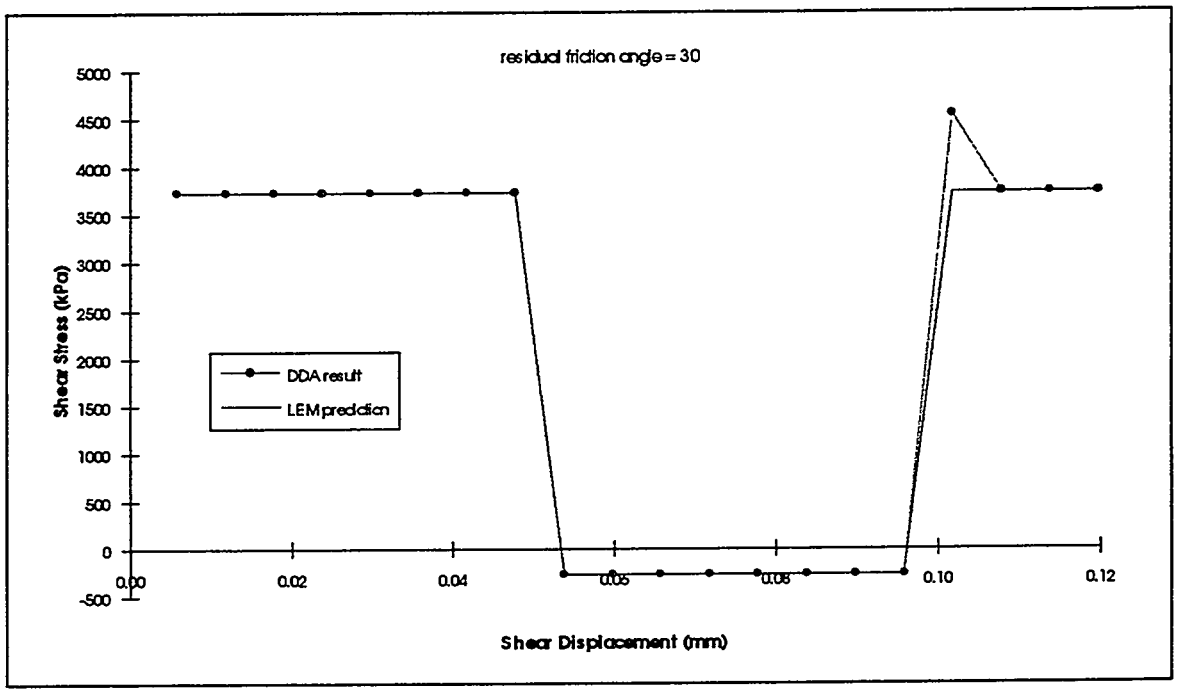

Figure 5.11: Results from DDA and Limit Equilibrium for test case

positive increment of dilation over that predicted by the DDA curve. This is because unlike DDA, the kinematic analysis does not take elastic deformations of the upper block and joint into account. The shapes of the DDA and kinematic analysis dilatancy curves are similar, but not identical. The similarity arises from the same peak dilation angles used at each increment of displacement in both methods. The discrepancy is due to the fact that the velocity acquired by the upper block in the DDA test may cause the upper joint profile to skip over parts of the lower profile. This skipping phenomena does not happen in the kinematic analysis. Figure 5.14 shows a comparison of the shear stresses from the three methods. The peak stress from the DDA simulation is close to but lower than the laboratory result. The residual shear stress values from DDA are a bit higher than the laboratory values. Around a displacement of 4 mm, the DDA shear stress value shows a high fluctuation. This fluctuation is due to a collision when a point on the upper profile first makes contact with a new segment of the

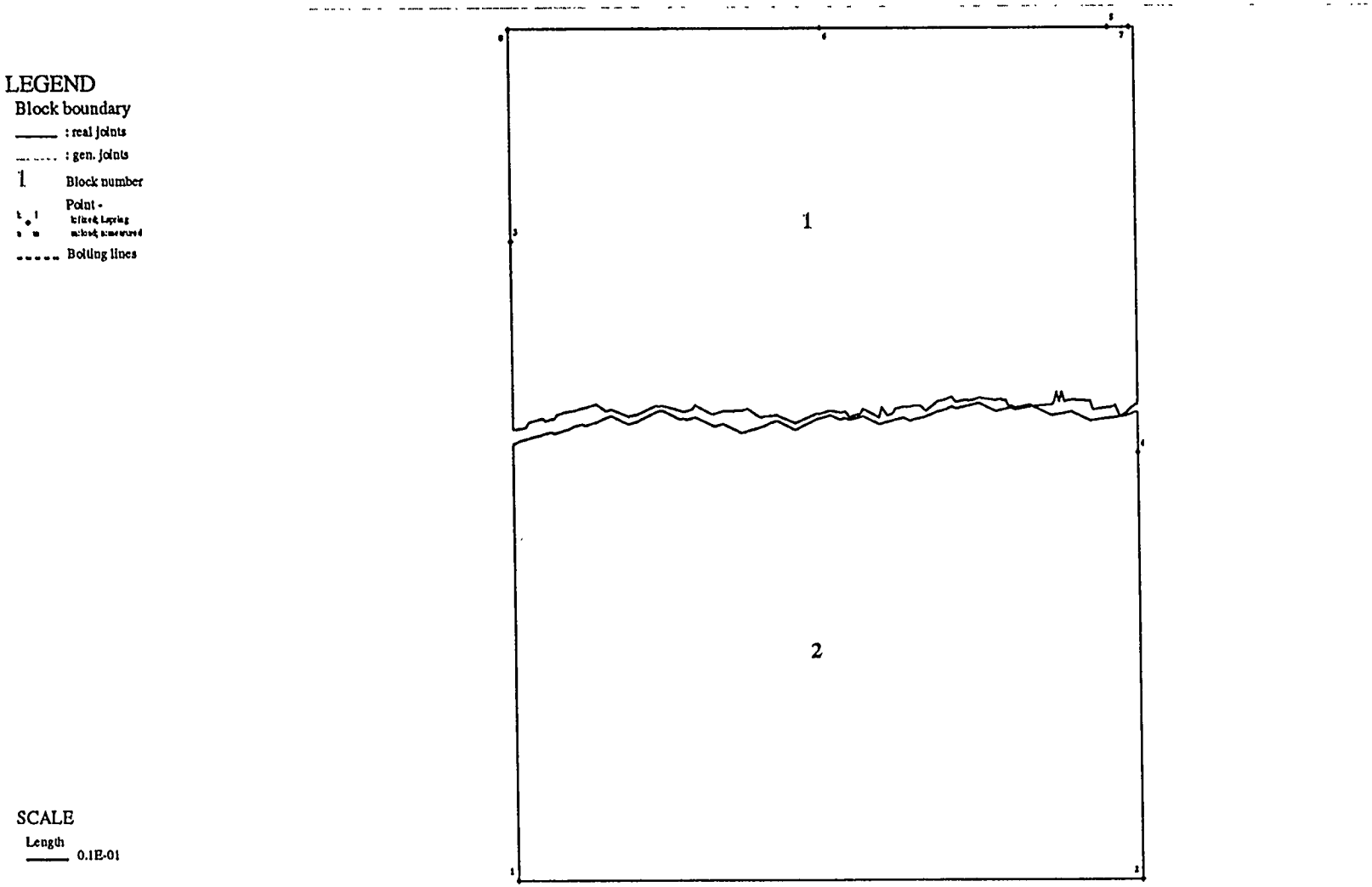

Figure 5.12: Direct shear test configuration for joint 13-1

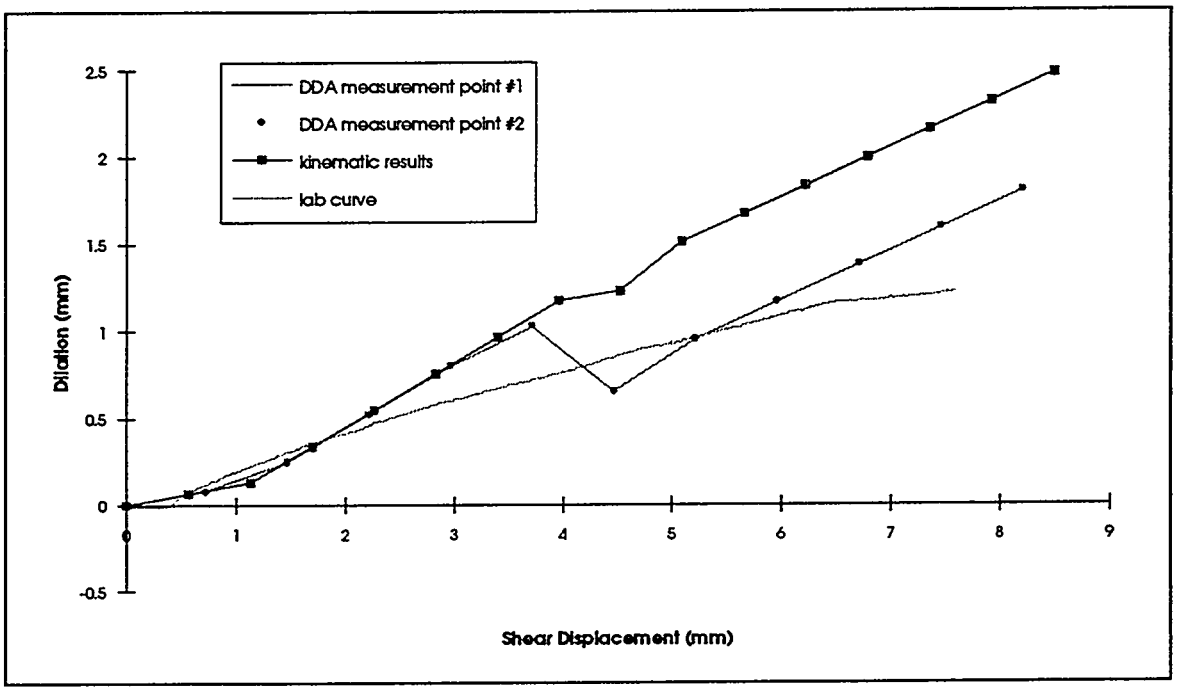

Figure 5.13: Dilatancy curves for joint 13-1

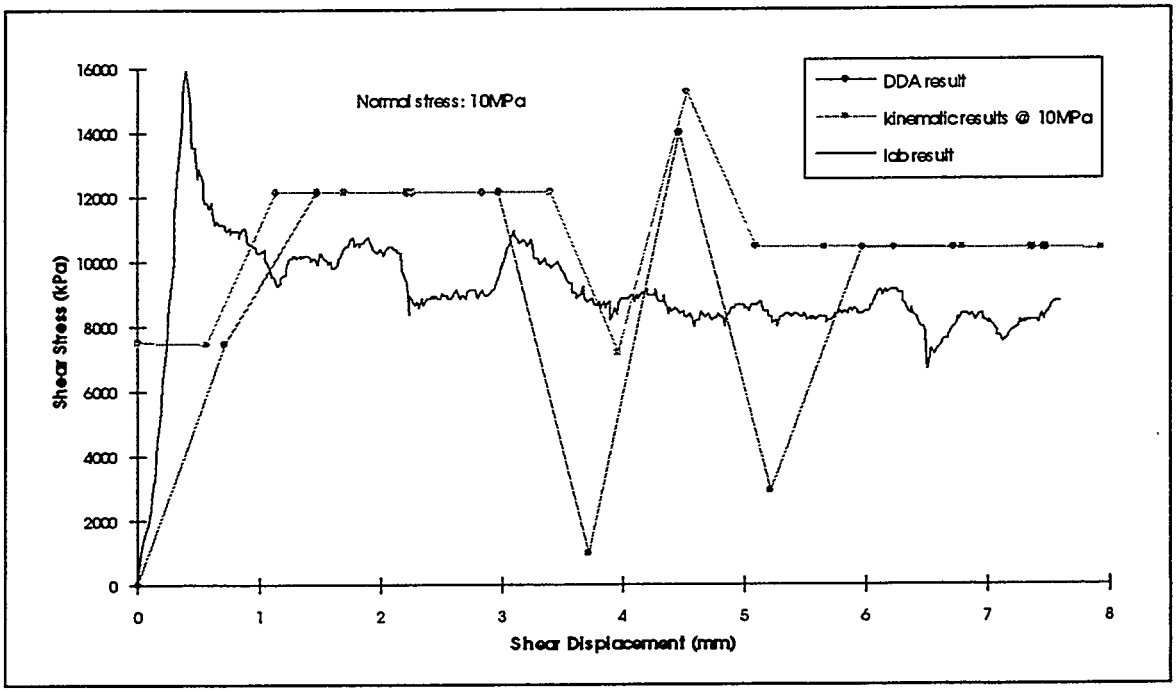

Figure 5.14: Shear stress-shear displacement curves for 13-1

lower profile. The collision causes a high shear stress values which reduces to the stable value as shown in the comparison of DDA and limit equilibrium results in Figure 5.11. The shear stress predicted by the kinematic analysis is very similar to the DDA result. The kinematic analysis prediction of shear stress also fluctuates at shear displacements of about 3.5 to 5 mm.

Figures 5.15 and 5.16 show comparisons of the DDA, kinematic analysis and laboratory results for joint 48-1. The tests on joint 48-1 were done at a much lower normal stress level (0.1 MPa) than joint 13-1. The lower normal stress level was expected to result in less asperity crushing in the laboratory test and thus give results closer to the DDA simulation values. However, Figure 5.15 shows the dilation predicted by DDA to be significantly higher than the measured laboratory values during the initial 5.5 mm of shear displacement. The discrepancy could be due to some surface roughness anisotropy, asperity crushing or both. The kinematic analysis dilatancy prediction is even higher than the DDA value, as expected, since the kinematic analysis does not take elastic deformation into account. The DDA and kinematic analysis predictions of shear strength are significantly lower than the laboratory measurement as shown in Figure 5.16. Unlike the clear peak strength seen in the laboratory test of joint 13-1, the low stress level used in the test results in a series of high shear stress values.

Figures 3.31 and 3.32 show the comparison of DDA, kinematic analysis and laboratory results for joint 64-1. As with joint 48-1, a low normal stress level was used in these tests (0.1 MPa). The dilatancy curves from DDA and the laboratory are fairly close up to a shear displacement of 4 mm while the kinematic analysis prediction is high, as expected. The shear stress predicted by DDA is again lower than the laboratory values. While the kinematic analysis shear stress prediction is closer to the laboratory measurement than the DDA

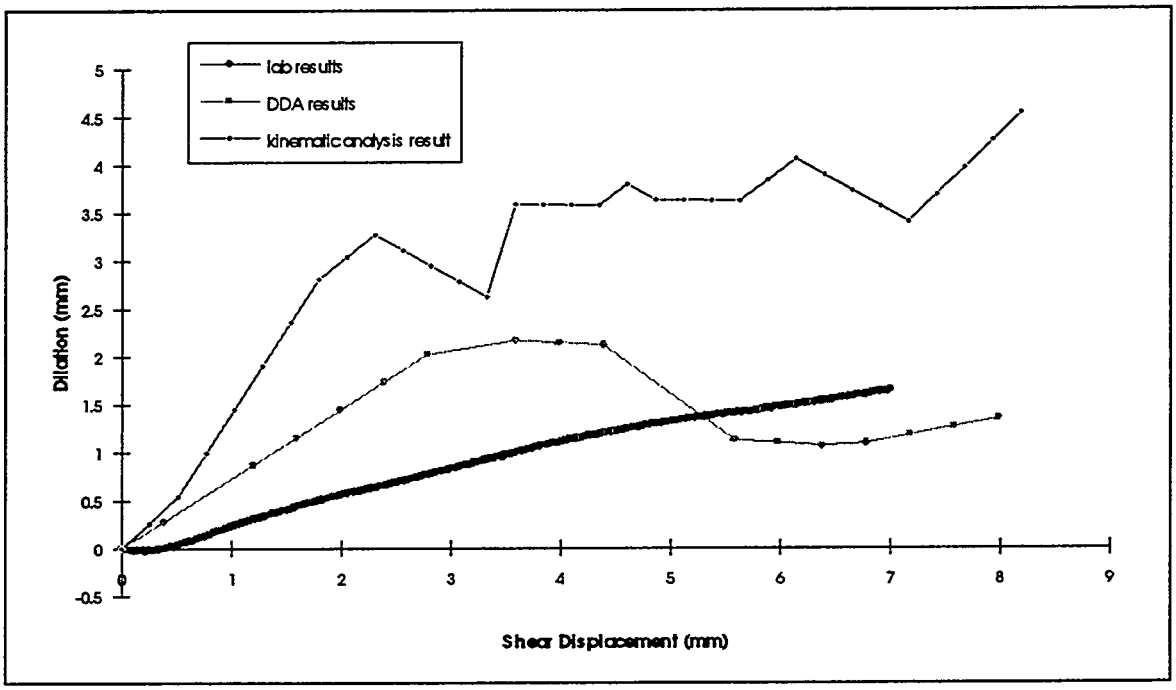

Figure 5.15: Dilation curves for joint 48-1

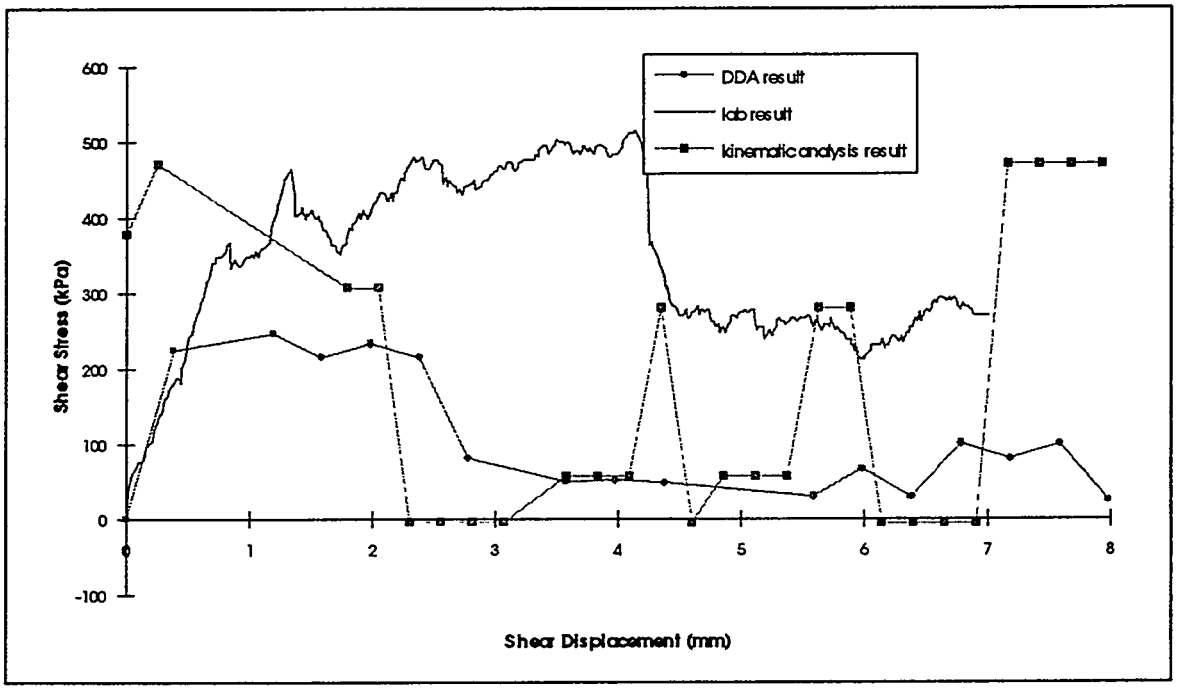

Figure 5.16: Shear stress-shear deformation curves for joint 48-1

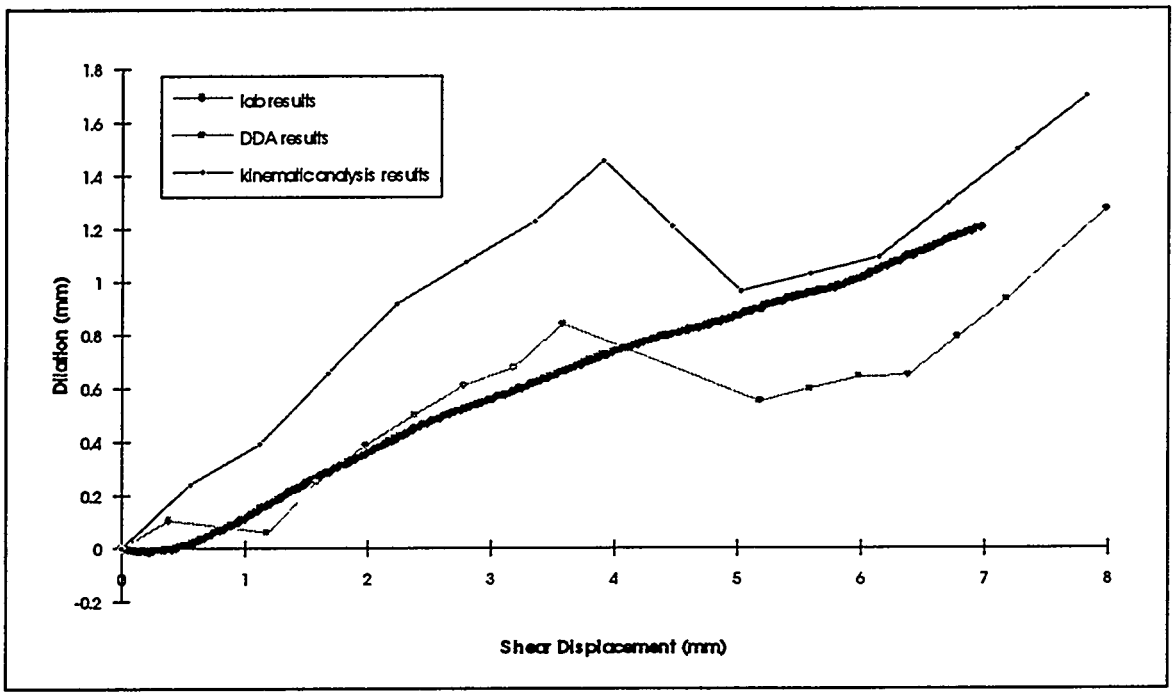

Figure 5.17: Dilation curves for joint 64-1

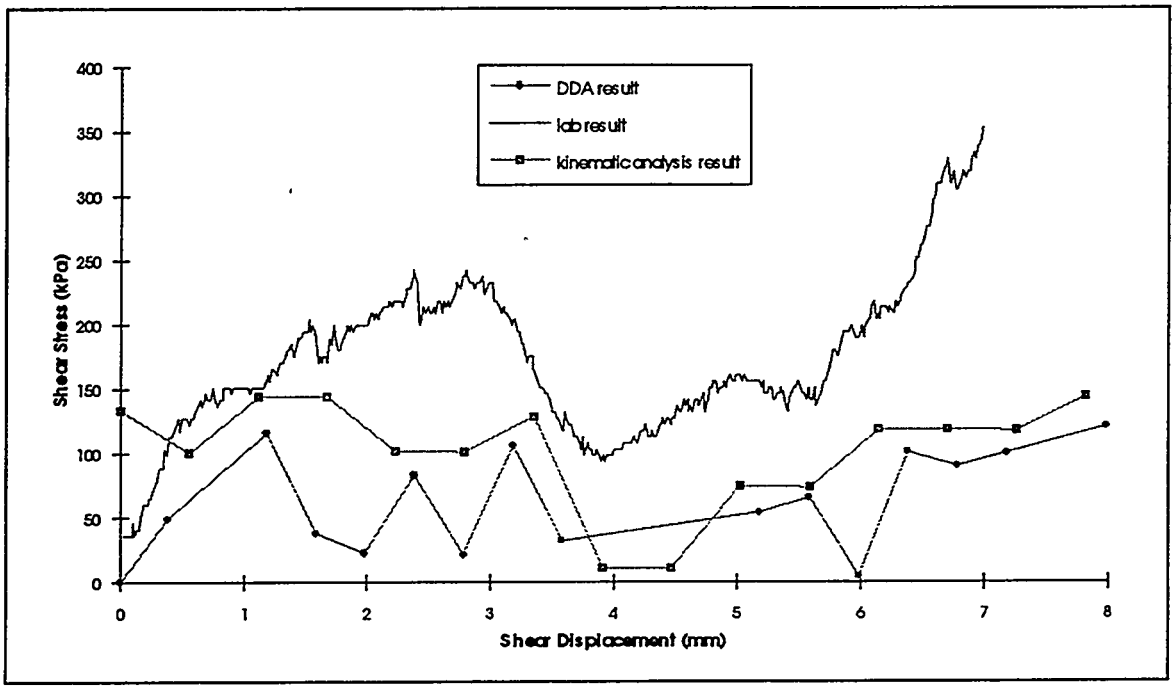

Figure 5.18: Shear stress-shear deformation curves for joint 64-1

results. Due to the low stress level, the laboratory curve in Figure 5.18 rises towards a second peak strength value, indicating little asperity crushing is being done during the shearing process.

Overall, the comparisons made here between the laboratory measurements, kinematic analysis and DDA simulations give mixed results. Results on joint 13-1 suggest BSS data can be analyzed for shear strength and dilatancy using the methods described here. The two joints in borehole 4-1 indicate the kinematic analysis and DDA simulation may underestimate the joint strength. One reason the kinematic analysis and DDA simulation did not work as well in the case of borehole 4-1 joints may be, that unlike the porphyritic granite of joint 13-1, the weaker rhyolite in the case of joints 48-1 and 64-1 may have led to more asperity crushing. If asperity crushing was extensive in the laboratory test, the kinematic analysis and DDA simulations can be expected to deviate from the lab result, as neither of the analysis take asperity crushing and subsequent influence of the broken asperities into account. More comparative studies in the future would lead to a better understanding of the conditions under which the shear strength analysis using the BSS data can provide reliable results.

CHAPTER 6
CONCLUSIONS AND RECOMMENDATIONS

Several new in-situ methods of joint characterization which can be performed using BSS data. Together, these methods provide a computer based approach for the assessment of in-situ joint strength and its spatial variability. Additionally, the methods developed in this thesis provide a starting point to pursue the development of various new methods of site characterization described in Section 2.3.2.

6.1 Current Limitations

The image processing method described in Chapter 3 to extract the joint roughness profile takes about one hour per joint to execute due to the need for extensive user interaction. This analysis rate needs to be improved to make it feasible to extract roughness profiles within the time and budget constraints of construction projects. In order to improve the extraction rate, the edge extraction method has to be automated as much as possible so that user interaction is minimized. Improvements in automation appear to be feasible using existing image processing methods.

The analysis of the roughness profile described in this thesis relies on the assumption that the orientation of the mean joint plane can be taken to be the orientation of a plane approximated by the BSS joint profile. Since the analysis results are sensitive to the value of the mean orientation used, any error in the mean orientation will result in errors in the analysis results. For instance, the assumption that the mean plane is equivalent to the BSS profile sample orientation could be wrong because of joint waviness. Averages over many joints from the same set should provide a more reliable mean orientation to use with the various analysis described in this thesis.

All of the joints seen in the BSS images were assumed to be real joints whose roughness profiles had not been altered during drilling. In fact, the drilling process may have created new fractures and changed the roughness profiles of some of the existing fractures. In some cases, a crystal separated by a joint shows the roughness profile to have been left unaltered by the drilling process. Portions of some joints show unusually sharp edges indicating recent fracturing during drilling. In general, it is difficult to judge if the drilling has significantly changed the natural condition.

6.2 Recommendations

The current BSS probe should be improved to include a sufficient number of bands of reflectance measurement so that mineralogy identification becomes possible. This would enable the BSS data to be used to completely characterize joint strength and also enhance the feasibility of other new analyses such as the technique for determining if a joint has conducted fluids in the past based on joint wall mineralogy.

The BSS probe needs to be fitted with a centering device. Without a centering device, the probe will generally not stay centered if there is a deviation of the borehole from vertical. When the probe is not centered, the pixels in the BSS image will not represent equal areas on the borehole wall and the interpretation of the data will be in error.

More comparisons of DDA direct shear tests and laboratory tests need to be made to understand the conditions under which the DDA test of BSS data may provide reliable results. Only the part of the unrolled profile which approximately corresponds to the direction of laboratory shear testing may be used in the DDA simulation if the joint roughness is even slightly anisotropic. The DDA model may also be improved by including artificial joints (Ke, 1993) at the base of the asperities. This would enable the DDA model to simulate the upper

profile shearing through lower profile asperities (or visa versa) instead of being constrained to dilate or contract only.

REFERENCES

Bandis, S., Lumsden, A.C. and Barton, N. (1983) Fundamentals of rock joint deformation, *International Journal of Rock Mechanics and Mining Sciences*, Vol 20, pp. 249-268

Bandis, S. (1994) Rock mass and site characterization, In Hudson, J. (ed.) *Comprehensive Rock Engineering*, Pergamon Press, New York, V.1, pp.155-183

Barton, C. (1988) *Development of in-situ stress measurement techniques for deep drillholes*, PhD Thesis, Stanford University

Barton, N. (1974) A review of the shear strength of filled discontinuities in rock, In *Proc. Bergmekanikk*, Oslo, Norway, pp. 19.1-19.38, Tapir, Oslo

Barton, N. and Choubey, V. (1977) The shear strength of rocks in theory and practice, *Rock Mechanics*, V.10, pp. 1-54

Barton, N.R. and Bandis, S.C. (1980) Some scale effects on the shear strength of joints, *International Journal of Rock Mechanics and Mining Sciences*, Vol 17, pp. 69-73

Barton, N., Bandis, S. and Bakhtar, K. (1985) Strength, deformation and conductivity coupling of rock joints, *International Journal of Rock Mechanics and Mining Sciences*, Vol 22, pp. 121-140

Bieniawski, Z.T. (1989) *Engineering rock mass classifications*, Wiley, New York

Borchers, J.W., Morin, R.H. and Hickman, S. (1993) Characterization of fractures in granitic rocks at Wawona, Yosemite National Park, California, *Trans. 1993 Fall Meeting*, American Geophysical Union, San Francisco

Boyle, W.J. (1986) *The influence of initial stresses on the movement of rock blocks around underground openings*, PhD Thesis, University of California at Berkeley

Brekke, T.L. and Howard, T.R. (1973) *Functional classification of gouge materials from seams and faults in relation to stability problems in underground openings*, Geotechnical Engineering Report, University of California, Berkeley

Briggs, R.O. (1964), Development of a Downhole Television Camera, *Fifth Annual SPWLA Logging Symposium*, Midland, Texas, pp. 13-15

Brown, S.R. and Scholz, C.H. (1985) Broad bandwidth study of the topography of natural joints, *Journal of Geophysical Research*, 90,12, pp.575-12,582

Brown, S.R., Kranz, R.L., and Bonner, B.P. (1986) Correlation between the surfaces of natural rock joints, *Geophysical Research Letters*, V.13, No. 12, pp. 1430-1433

Cluff, L.S. (1966), *Borehole Cameras*, Report to the American Society for Testing and Materials, Committee D-18, Section E, Subcommittee 1

Cook, N.G.W. (1992), Natural joints in rocks, *International Journal for Numerical and Analytical Methods in Geomechanics*, Vol. 29, pp.198-223

Dershowitz, W.S. and Einstein, H.H. (1988) Characterizing rock joint geometry with joint system models, Rock Mechanics and Rock Engineeing, V.21, No.1, pp.21-52

Fabbri, A.G. (1984) *Image processing of geological data*, Van Nostrand Reinhold Co., New York

Einstein, H. (1993) Modern developments in discontinuity analysis - the persistence-connectivity problem. In Hudson, J. (ed.) *Comprehensive Rock Engineering*,Pergamon Press, New York, V.3, pp.193-213

Fecker, E. and Rengers, N. (1971) Measurement of large scale roughness of rock planes by means of profilograph and geologic compass, *Proceedings, International Symposium on Rock Fracture*, Nancy (ISRM), paper 1-18

Goodman, R.E. (1976), *Methods of Geological Engineering in Discontinuous Rocks*, West Publishing Co., St. Paul

Goodman, R.E. and Shi, G.H (1985), *Block Theory and its Application to Rock Engineering*, Prentice-Hall, Inc. Englewood Cliffs, New Jersey

Gonzalez, R.C. and Woods, R.E. (1992) *Digital Image Processing*, Addison Wesley, New York

Harrison, J.P. and Goodfellow, R.J.F. (1993) Effect of scale on roughness anisotropy and magnitude, In *Scale effects in rock masses*, Cunha, A.P. (ed), Balkema

Hatzor, Y. (1992), *Validation of Block Theory Using Field Case Histories*, Ph.D. Thesis, University of California at Berkeley

Heuze, F.E. (1979) Dilatant effects of rock joints, *Proc. Fourth Congress International Society of Rock Mechanics*, Montreux, Balkema, Rotterdam, pp.169-175

Huang, T.H. and Doong, Y.S. (1990) Anisotropic shear strength of rock joints, *Proc. International Symposium on Rock Joints*, Loen, Norway, Balkema, Rotterdam

Hudson, J.A. (1994) Rock properties, testing methods and site characterization, In Hudson, J. (ed.) *Comprehensive Rock Engineering*, Pergamon Press, New York, V.3, pp.1-40

Ladanyi, B. and Archambault, G. (1970) Simulation of shear behavior of a jointed rockmass, In *Proc. 11th U.S. Symp. Rock Mech.*, Berkeley, CA (Edited by W.H. Somerton), pp. 105-125

Lee, J.W. (1982), *Well Testing*, Society of Petroleum Engineers of AIME, New York

Long, J.C.S (1994) Construction of equivalent discontinuum models for fracture hydrology, In Hudson, J. (ed.) *Comprehensive Rock Engineering*, Pergamon Press, New York, V.3, pp.241-296

Makurat, A., Barton, N., Rad, N.S. and Bandis, S.C. (1990) Joint conductivity variation due to normal and shear deformation. In *Proc. Int. Conf. Rock Joints*, Loen, Norway (edited by N. Barton and O. Stephansson), pp. 534-540

Patton, F.D. (1966) Multiple modes of shear failure in rock, *Proc. 1st Cong. ISRM* (Lisbon), Vol. 1, pp.509-513

Pointe, P.R. La (1994) Pattern analysis and simulation of joints in rock enginereing, In Hudson, J. (ed.) *Comprehensive Rock Engineering*, Pergamon Press, New York, V.3, pp.215-240

Priest, S.D. and Hudson, J.A. (1976) Discontinuity spacings in rock, *International Journal of Rock Mechanics and Mining Sciences*, Vol 13, pp. 135-148

Ramsay, J.G. and Huber, M.I. (1983) *The techniques of modern structural geology, volume 1: strain analysis*, Academic Press, San Diego

Rengers, N. (1970) Influence of surface roughness on the friction properties of rock planes, *Proc. 2nd Congress ISRM (Belgrade)*, V.1, pp. 229-234

Schneider, H.J. (1976) Comments in *Proceedings of International Symposium on Numerical Methods in Soil Mechanics and Rock Mechanics*, G. Borm and H. Meissner, Eds., pp. 220-223 (Inst. fur Bodenmechanik und Felsmechanik of Karlsruhe University, D-7500, Karlsruhe 1, Germany)

Schneider, H.J. (1976) The friction and deformation behavior of rock joints, Rock Mechanics and Rock Engineeing, V.8, No.3, pp.169-184

Selby, M.J. (1982), *Hillslope Materials and Processes*, Oxford University Press, New York

Shi, G.H. (1985) *Discontinuous deformation analysis: a new approach to the statics and dynamics of block systems*, PhD Thesis, University of California at Berkeley

Shi, G.H. and Goodman, R.E. (1989*), The key blocks of unrolled joint traces in developed maps of tunnel walls, International Journal for Numerical and Analytical Methods in Geomechanics*, Vol. 13, pp.131-158

Snow, D.T. (1970) The frequency and apertures of fractures in rocks, *International Journal of Rock Mechanics and Mining Sciences*, Vol. 7, pp.23-40

Suppe, J. (1985), *Principles of Structural Geology*, Prentice-Hall, Inc. Englewood Cliffs, New Jersey

Tang, W., Quek, S.T. (1986) Statistical model of boulder size and fraction, *Journal of Geotechnical Engineering*, ASCE, V. 112, No. 1, pp.79-90

Tanimoto, C., Murai, S., Matsumoto, T., Kishida, K. and Ando, T. (1992) Immediate Image and its Analysis of Fractured and Jointed Rock Mass through the Borehole Scanner in *Proceedings of Fractured and Jointed Rock Masses*, Lake Tahoe, California

Tanimoto, C., Kishida, K., Yoshizu, Y. and Kunii, K. (1994) Siesmic attenuation geotomographic technique in designing a large underground cavern, *Proc. ISRM Symposium*, Santiago, Chile

Telford, W.M., Geldart, L.P. and Sheriff, R.E. (1990), *Applied Geophysics*, Cambridge University Press, Cambridge

Thapa, B.B. and Goodman, R.E. (1994), The Induced Wedge Test, *International Journal of Rock Mechanics and Mining Sciences*

Trantina, J.A. and Cluff, L.S. (1963), *NX Bore-Hole Camera*, American Society for Testing and Materials, Special Technical Publication No. 351

Zemanek, J., Glenn, E.E., Norton, L.J. and Caldwell, R.L. (1970), *Formation evaluation by inspection with the borehole televiewer*, Geophysics, Vol. 35, pp. 254-269

APPENDIX

A. Roughness profile points extracted from BSS image for joint 13-1

Table A.1: Roughness profile points of joint 13-1

<----------	Upper	Profile	---------->	<----------	Lower	Profile	---------->
rotation	depth data	azimuth	depth	rotation	depth data	azimuth	depth
data	in image y	in degrees	in mm	data	in image y	in degrees	in mm
1	650	180.720001	13428.25	1	655	180.720001	13434.5
2	650	181.440002	13428.25	2	655	181.440002	13434.5
3	650	182.160004	13428.25	3	656	182.160004	13432.25
4	650	182.880005	13428.25	4	656	182.880005	13432.25
4	651	182.880005	13430.25	4	655	182.880005	13434.5
5	651	183.600006	13430.25	5	655	183.600006	13434.5
6	651	184.320007	13430.25	6	655	184.320007	13434.5
7	651	185.039993	13430.25	7	655	185.039993	13434.5
7	652	185.039993	13430.75	8	655	185.759995	13434.5
8	652	185.759995	13430.75	9	655	186.479996	13434.5
8	653	185.759995	13433	10	655	187.199997	13434.5
9	653	186.479996	13433	11	656	187.919998	13432.25
10	653	187.199997	13433	12	656	188.639999	13432.25
11	653	187.919998	13433	13	657	189.360001	13434.5
11	654	187.919998	13432.25	14	657	190.080002	13434.5
12	654	188.639999	13432.25	15	657	190.800003	13434.5
13	654	189.360001	13432.25	16	658	191.520004	13433.5
13	655	189.360001	13434.5	17	659	192.240005	13434
14	655	190.080002	13434.5	18	660	192.960007	13436
14	656	190.080002	13432.25	18	661	192.960007	13436.75
15	656	190.800003	13432.25	19	662	193.679993	13436
16	656	191.520004	13432.25	20	663	194.399994	13435.25
17	656	192.240005	13432.25	21	664	195.119995	13435.75
17	657	192.240005	13434.5	22	664	195.839996	13435.75
18	657	192.960007	13434.5	23	664	196.559998	13435.75
19	657	193.679993	13434.5	24	664	197.279999	13435.75
20	657	194.399994	13434.5	25	664	198	13435.75
21	657	195.119995	13434.5	25	663	198	13435.25
21	658	195.119995	13433.5	26	663	198.720001	13435.25
22	658	195.839996	13433.5	27	663	199.440002	13435.25
23	658	196.559998	13433.5	28	663	200.160004	13435.25
23	659	196.559998	13434	29	663	200.880005	13435.25
24	659	197.279999	13434	29	662	200.880005	13436
25	659	198	13434	30	662	201.600006	13436
26	659	198.720001	13434	31	662	202.320007	13436
27	659	199.440002	13434	32	662	203.039993	13436
28	659	200.160004	13434	33	662	203.759995	13436
29	659	200.880005	13434	34	662	204.479996	13436
30	659	201.600006	13434	35	663	205.199997	13435.25
31	658	202.320007	13433.5	36	663	205.919998	13435.25

32	658	203.039993	13433.5	37	663	206.639999	13435.25
33	658	203.759995	13433.5	38	663	207.360001	13435.25
34	657	204.479996	13434.5	39	663	208.080002	13435.25
35	657	205.199997	13434.5	40	663	208.800003	13435.25
36	657	205.919998	13434.5	41	663	209.520004	13435.25
37	657	206.639999	13434.5	42	663	210.240005	13435.25
38	657	207.360001	13434.5	43	663	210.960007	13435.25
38	658	207.360001	13433.5	44	663	211.679993	13435.25
39	658	208.080002	13433.5	45	663	212.399994	13435.25
40	658	208.800003	13433.5	46	663	213.119995	13435.25
41	658	209.520004	13433.5	47	663	213.839996	13435.25
41	659	209.520004	13434	48	664	214.559998	13435.75
42	659	210.240005	13434	49	664	215.279999	13435.75
43	659	210.960007	13434	50	664	216	13435.75
44	659	211.679993	13434	51	664	216.720001	13435.75
44	660	211.679993	13436	52	664	217.440002	13435.75
45	660	212.399994	13436	53	664	218.160004	13435.75
46	659	213.119995	13434	54	664	218.880005	13435.75
47	659	213.839996	13434	55	664	219.600006	13435.75
47	660	213.839996	13436	56	664	220.320007	13435.75
48	660	214.559998	13436	57	664	221.039993	13435.75
49	660	215.279999	13436	58	664	221.759995	13435.75
50	660	216	13436	59	664	222.479996	13435.75
51	660	216.720001	13436	60	664	223.199997	13435.75
51	661	216.720001	13436.75	61	664	223.919998	13435.75
52	661	217.440002	13436.75	62	664	224.639999	13435.75
53	661	218.160004	13436.75	63	664	225.360001	13435.75
54	661	218.880005	13436.75	64	665	226.080002	13437.75
55	661	219.600006	13436.75	65	666	226.800003	13438.25
56	661	220.320007	13436.75	66	667	227.520004	13440.5
57	661	221.039993	13436.75	67	667	228.240005	13440.5
58	661	221.759995	13436.75	68	668	228.960007	13442.75
58	662	221.759995	13436	69	668	229.679993	13442.75
59	662	222.479996	13436	70	669	230.399994	13442
60	662	223.199997	13436	71	669	231.119995	13442
61	661	223.919998	13436.75	72	669	231.839996	13442
62	661	224.639999	13436.75	73	670	232.559998	13442.75
63	661	225.360001	13436.75	74	671	233.279999	13444.75
64	661	226.080002	13436.75	75	671	234	13444.75
64	662	226.080002	13436	76	671	234.720001	13444.75
65	662	226.800003	13436	77	671	235.440002	13444.75
66	662	227.520004	13436	78	671	236.160004	13444.75
67	662	228.240005	13436	79	671	236.880005	13444.75
68	662	228.960007	13436	79	670	236.880005	13442.75
69	662	229.679993	13436	80	670	237.600006	13442.75
70	662	230.399994	13436	81	670	238.320007	13442.75
71	662	231.119995	13436	82	670	239.039993	13442.75
71	663	231.119995	13435.25	82	669	239.039993	13442
72	663	231.839996	13435.25	83	669	239.759995	13442
73	663	232.559998	13435.25	84	669	240.479996	13442

73	664	232.559998	13435.75	85	669	241.199997	13442
74	664	233.279999	13435.75	86	669	241.919998	13442
75	664	234	13435.75	87	669	242.639999	13442
75	665	234	13437.75	88	669	243.360001	13442
76	665	234.720001	13437.75	89	669	244.080002	13442
77	665	235.440002	13437.75	90	669	244.800003	13442
78	665	236.160004	13437.75	91	669	245.520004	13442
79	665	236.880005	13437.75	92	669	246.240005	13442
80	665	237.600006	13437.75	93	669	246.960007	13442
81	665	238.320007	13437.75	94	669	247.679993	13442
82	665	239.039993	13437.75	95	669	248.399994	13442
83	664	239.759995	13435.75	95	668	248.399994	13442.75
84	664	240.479996	13435.75	96	668	249.119995	13442.75
85	664	241.199997	13435.75	97	668	249.839996	13442.75
86	664	241.919998	13435.75	98	668	250.559998	13442.75
87	664	242.639999	13435.75	99	668	251.279999	13442.75
88	664	243.360001	13435.75	100	668	252	13442.75
89	664	244.080002	13435.75	101	668	252.720001	13442.75
90	664	244.800003	13435.75	102	668	253.440002	13442.75
91	664	245.520004	13435.75	103	668	254.160004	13442.75
92	664	246.240005	13435.75	104	668	254.880005	13442.75
93	664	246.960007	13435.75	105	668	255.600006	13442.75
94	664	247.679993	13435.75	106	668	256.320007	13442.75
95	663	248.399994	13435.25	107	668	257.040009	13442.75
96	663	249.119995	13435.25	108	668	257.76001	13442.75
97	663	249.839996	13435.25	109	668	258.480011	13442.75
98	663	250.559998	13435.25	110	668	259.200012	13442.75
99	663	251.279999	13435.25	111	668	259.920013	13442.75
100	663	252	13435.25	112	668	260.640015	13442.75
101	662	252.720001	13436	113	668	261.359985	13442.75
102	662	253.440002	13436	114	668	262.079987	13442.75
103	662	254.160004	13436	115	668	262.799988	13442.75
104	662	254.880005	13436	116	668	263.519989	13442.75
105	662	255.600006	13436	117	669	264.23999	13442
106	662	256.320007	13436	118	669	264.959991	13442
106	663	256.320007	13435.25	119	669	265.679993	13442
107	663	257.040009	13435.25	120	669	266.399994	13442
108	663	257.76001	13435.25	121	669	267.119995	13442
109	663	258.480011	13435.25	122	669	267.839996	13442
110	663	259.200012	13435.25	123	669	268.559998	13442
110	664	259.200012	13435.75	124	669	269.279999	13442
110	665	259.200012	13437.75	125	669	270	13442
110	666	259.200012	13438.25	126	669	270.720001	13442
111	666	259.920013	13438.25	127	669	271.440002	13442
112	666	260.640015	13438.25	127	668	271.440002	13442.75
113	666	261.359985	13438.25	128	668	272.160004	13442.75
114	666	262.079987	13438.25	129	668	272.880005	13442.75
115	666	262.799988	13438.25	130	668	273.600006	13442.75
115	667	262.799988	13440.5	131	668	274.320007	13442.75
116	667	263.519989	13440.5	132	668	275.040009	13442.75

117	667	264.23999	13440.5	133	668	275.76001	13442.75
117	668	264.23999	13442.75	134	668	276.480011	13442.75
118	668	264.959991	13442.75	135	668	277.200012	13442.75
119	668	265.679993	13442.75	136	668	277.920013	13442.75
120	668	266.399994	13442.75	137	668	278.640015	13442.75
121	668	267.119995	13442.75	138	668	279.359985	13442.75
122	668	267.839996	13442.75	139	668	280.079987	13442.75
123	668	268.559998	13442.75	140	668	280.799988	13442.75
124	668	269.279999	13442.75	141	668	281.519989	13442.75
125	668	270	13442.75	142	668	282.23999	13442.75
126	668	270.720001	13442.75	143	668	282.959991	13442.75
127	668	271.440002	13442.75	143	667	282.959991	13440.5
128	668	272.160004	13442.75	144	667	283.679993	13440.5
129	668	272.880005	13442.75	145	667	284.399994	13440.5
130	667	273.600006	13440.5	146	667	285.119995	13440.5
130	668	273.600006	13442.75	147	667	285.839996	13440.5
131	668	274.320007	13442.75	148	667	286.559998	13440.5
132	667	275.040009	13440.5	149	667	287.279999	13440.5
133	667	275.76001	13440.5	150	667	288	13440.5
134	667	276.480011	13440.5	151	667	288.720001	13440.5
135	667	277.200012	13440.5	151	666	288.720001	13438.25
136	667	277.920013	13440.5	152	666	289.440002	13438.25
137	667	278.640015	13440.5	153	666	290.160004	13438.25
138	667	279.359985	13440.5	154	666	290.880005	13438.25
139	667	280.079987	13440.5	155	666	291.600006	13438.25
140	667	280.799988	13440.5	156	666	292.320007	13438.25
141	666	281.519989	13438.25	157	666	293.040009	13438.25
142	665	282.23999	13437.75	158	666	293.76001	13438.25
143	665	282.959991	13437.75	158	665	293.76001	13437.75
144	664	283.679993	13435.75	159	665	294.480011	13437.75
145	664	284.399994	13435.75	160	665	295.200012	13437.75
145	665	284.399994	13437.75	161	665	295.920013	13437.75
146	665	285.119995	13437.75	162	665	296.640015	13437.75
147	665	285.839996	13437.75	163	665	297.359985	13437.75
148	665	286.559998	13437.75	164	665	298.079987	13437.75
149	665	287.279999	13437.75	164	664	298.079987	13435.75
149	666	287.279999	13438.25	165	664	298.799988	13435.75
150	666	288	13438.25	166	664	299.519989	13435.75
151	666	288.720001	13438.25	167	664	300.23999	13435.75
152	665	289.440002	13437.75	168	664	300.959991	13435.75
153	665	290.160004	13437.75	169	664	301.679993	13435.75
154	665	290.880005	13437.75	170	664	302.399994	13435.75
155	665	291.600006	13437.75	171	664	303.119995	13435.75
156	665	292.320007	13437.75	172	664	303.839996	13435.75
157	665	293.040009	13437.75	173	664	304.559998	13435.75
158	665	293.76001	13437.75	173	663	304.559998	13435.25
159	665	294.480011	13437.75	173	662	304.559998	13436
160	665	295.200012	13437.75	174	662	305.279999	13436
161	664	295.920013	13435.75	175	662	306	13436
162	664	296.640015	13435.75	176	662	306.720001	13436

163	663	297.359985	13435.25	177	662	307.440002	13436
164	663	298.079987	13435.25	177	661	307.440002	13436.75
165	663	298.799988	13435.25	178	661	308.160004	13436.75
166	663	299.519989	13435.25	179	661	308.880005	13436.75
167	662	300.23999	13436	180	661	309.600006	13436.75
168	662	300.959991	13436	181	661	310.320007	13436.75
169	662	301.679993	13436	182	661	311.040009	13436.75
170	662	302.399994	13436	183	661	311.76001	13436.75
171	661	303.119995	13436.75	184	661	312.480011	13436.75
172	661	303.839996	13436.75	185	661	313.200012	13436.75
173	661	304.559998	13436.75	185	660	313.200012	13436
174	661	305.279999	13436.75	186	660	313.920013	13436
175	661	306	13436.75	187	660	314.640015	13436
176	661	306.720001	13436.75	188	660	315.359985	13436
177	661	307.440002	13436.75	189	660	316.079987	13436
178	661	308.160004	13436.75	190	660	316.799988	13436
179	661	308.880005	13436.75	191	660	317.519989	13436
180	661	309.600006	13436.75	192	660	318.23999	13436
181	660	310.320007	13436	193	660	318.959991	13436
182	659	311.040009	13434	194	660	319.679993	13436
183	658	311.76001	13433.5	194	659	319.679993	13434
184	658	312.480011	13433.5	195	659	320.399994	13434
185	658	313.200012	13433.5	196	659	321.119995	13434
186	658	313.920013	13433.5	197	659	321.839996	13434
187	658	314.640015	13433.5	198	659	322.559998	13434
188	658	315.359985	13433.5	199	659	323.279999	13434
189	658	316.079987	13433.5	199	658	323.279999	13433.5
190	657	316.799988	13434.5	200	658	324	13433.5
191	657	317.519989	13434.5	201	658	324.720001	13433.5
192	657	318.23999	13434.5	201	657	324.720001	13434.5
193	656	318.959991	13432.25	202	657	325.440002	13434.5
194	656	319.679993	13432.25	202	656	325.440002	13432.25
195	655	320.399994	13434.5	203	656	326.160004	13432.25
196	655	321.119995	13434.5	204	656	326.880005	13432.25
197	655	321.839996	13434.5	205	656	327.600006	13432.25
198	655	322.559998	13434.5	206	656	328.320007	13432.25
199	655	323.279999	13434.5	207	656	329.040009	13432.25
200	655	324	13434.5	207	655	329.040009	13434.5
201	655	324.720001	13434.5	208	655	329.76001	13434.5
202	655	325.440002	13434.5	209	655	330.480011	13434.5
203	654	326.160004	13432.25	209	654	330.480011	13432.25
204	654	326.880005	13432.25	210	654	331.200012	13432.25
205	654	327.600006	13432.25	211	654	331.920013	13432.25
206	654	328.320007	13432.25	211	653	331.920013	13433
207	654	329.040009	13432.25	212	653	332.640015	13433
208	654	329.76001	13432.25	213	653	333.359985	13433
209	653	330.480011	13433	214	653	334.079987	13433
210	653	331.200012	13433	215	653	334.799988	13433
211	653	331.920013	13433	216	653	335.519989	13433
212	652	332.640015	13430.75	217	653	336.23999	13433

213	652	333.359985	13430.75	218	653	336.959991	13433
214	652	334.079987	13430.75	219	653	337.679993	13433
215	651	334.799988	13430.25	220	653	338.399994	13433
216	650	335.519989	13428.25	220	652	338.399994	13430.75
217	649	336.23999	13427.75	221	652	339.119995	13430.75
218	649	336.959991	13427.75	222	652	339.839996	13430.75
219	649	337.679993	13427.75	223	652	340.559998	13430.75
220	649	338.399994	13427.75	223	651	340.559998	13430.25
221	649	339.119995	13427.75	224	651	341.279999	13430.25
222	649	339.839996	13427.75	224	650	341.279999	13428.25
223	649	340.559998	13427.75	225	650	342	13428.25
224	649	341.279999	13427.75	226	650	342.720001	13428.25
225	648	342	13425.5	227	650	343.440002	13428.25
226	647	342.720001	13426.25	227	649	343.440002	13427.75
227	647	343.440002	13426.25	228	649	344.160004	13427.75
228	647	344.160004	13426.25	229	649	344.880005	13427.75
229	647	344.880005	13426.25	229	648	344.880005	13425.5
230	646	345.600006	13425.75	230	648	345.600006	13425.5
231	646	346.320007	13425.75	231	648	346.320007	13425.5
232	646	347.040009	13425.75	232	649	347.040009	13427.75
233	645	347.76001	13426.5	233	649	347.76001	13427.75
234	645	348.480011	13426.5	234	649	348.480011	13427.75
235	644	349.200012	13426	235	649	349.200012	13427.75
236	644	349.920013	13426	236	649	349.920013	13427.75
237	643	350.640015	13424	236	648	349.920013	13425.5
238	643	351.359985	13424	237	648	350.640015	13425.5
239	643	352.079987	13424	238	648	351.359985	13425.5
240	642	352.799988	13422	239	648	352.079987	13425.5
241	642	353.519989	13422	239	647	352.079987	13426.25
242	642	354.23999	13422	240	647	352.799988	13426.25
243	642	354.959991	13422	241	647	353.519989	13426.25
244	642	355.679993	13422	242	647	354.23999	13426.25
245	642	356.399994	13422	243	647	354.959991	13426.25
246	642	357.119995	13422	244	647	355.679993	13426.25
247	642	357.839996	13422	244	646	355.679993	13425.75
248	642	358.559998	13422	245	646	356.399994	13425.75
249	642	359.279999	13422	246	646	357.119995	13425.75
250	642	0	13422	247	646	357.839996	13425.75
251	642	0.72	13422	248	646	358.559998	13425.75
252	642	1.44	13422	249	647	359.279999	13426.25
253	642	2.16	13422	250	647	0	13426.25
254	641	2.88	13422.75	251	647	0.72	13426.25
255	641	3.6	13422.75	252	647	1.44	13426.25
256	641	4.32	13422.75	253	647	2.16	13426.25
257	641	5.04	13422.75	254	647	2.88	13426.25
258	640	5.76	13422	254	646	2.88	13425.75
259	640	6.48	13422	255	646	3.6	13425.75
260	640	7.2	13422	256	646	4.32	13425.75
261	640	7.92	13422	257	646	5.04	13425.75
262	640	8.64	13422	258	646	5.76	13425.75

263	640	9.36	13422	259	646	6.48	13425.75
264	639	10.08	13423	260	646	7.2	13425.75
265	639	10.8	13423	261	646	7.92	13425.75
266	639	11.52	13423	262	646	8.64	13425.75
267	639	12.24	13423	263	646	9.36	13425.75
268	638	12.96	13422.5	264	646	10.08	13425.75
269	638	13.68	13422.5	265	646	10.8	13425.75
270	638	14.4	13422.5	266	646	11.52	13425.75
271	638	15.12	13422.5	266	645	11.52	13426.5
272	638	15.84	13422.5	267	645	12.24	13426.5
273	638	16.559999	13422.5	268	645	12.96	13426.5
274	638	17.280001	13422.5	269	645	13.68	13426.5
275	638	18	13422.5	270	645	14.4	13426.5
276	637	18.719999	13420.5	270	644	14.4	13426
277	637	19.440001	13420.5	271	644	15.12	13426
278	637	20.16	13420.5	272	644	15.84	13426
279	637	20.879999	13420.5	272	643	15.84	13424
280	637	21.6	13420.5	273	643	16.559999	13424
281	637	22.32	13420.5	274	643	17.280001	13424
282	636	23.040001	13420	275	643	18	13424
283	636	23.76	13420	276	643	18.719999	13424
284	635	24.48	13418	276	642	18.719999	13422
285	635	25.200001	13418	277	642	19.440001	13422
286	635	25.92	13418	278	642	20.16	13422
287	635	26.639999	13418	279	642	20.879999	13422
288	634	27.360001	13417.5	280	642	21.6	13422
289	634	28.08	13417.5	281	642	22.32	13422
290	634	28.799999	13417.5	282	642	23.040001	13422
291	634	29.52	13417.5	283	642	23.76	13422
292	633	30.24	13415.25	284	642	24.48	13422
293	633	30.959999	13415.25	285	642	25.200001	13422
294	633	31.68	13415.25	286	642	25.92	13422
295	633	32.400002	13415.25	287	642	26.639999	13422
296	633	33.119999	13415.25	288	642	27.360001	13422
297	633	33.84	13415.25	289	642	28.08	13422
298	633	34.560001	13415.25	290	642	28.799999	13422
299	633	35.279999	13415.25	290	641	28.799999	13422.75
300	633	36	13415.25	291	641	29.52	13422.75
301	633	36.720001	13415.25	292	641	30.24	13422.75
302	633	37.439999	13415.25	293	641	30.959999	13422.75
303	633	38.16	13415.25	294	641	31.68	13422.75
304	633	38.880001	13415.25	295	641	32.400002	13422.75
305	633	39.599998	13415.25	296	641	33.119999	13422.75
306	633	40.32	13415.25	297	641	33.84	13422.75
307	633	41.040001	13415.25	298	641	34.560001	13422.75
308	633	41.759998	13415.25	299	641	35.279999	13422.75
309	633	42.48	13415.25	300	641	36	13422.75
310	633	43.200001	13415.25	301	641	36.720001	13422.75
311	633	43.919998	13415.25	301	640	36.720001	13422
312	633	44.639999	13415.25	302	640	37.439999	13422

313	633	45.360001	13415.25	303	640	38.16	13422
314	633	46.080002	13415.25	304	640	38.880001	13422
315	633	46.799999	13415.25	305	640	39.599998	13422
316	633	47.52	13415.25	305	639	39.599998	13423
317	633	48.240002	13415.25	306	639	40.32	13423
318	633	48.959999	13415.25	307	639	41.040001	13423
319	633	49.68	13415.25	308	639	41.759998	13423
320	633	50.400002	13415.25	309	640	42.48	13422
321	633	51.119999	13415.25	310	640	43.200001	13422
322	633	51.84	13415.25	311	640	43.919998	13422
323	633	52.560001	13415.25	312	641	44.639999	13422.75
324	633	53.279999	13415.25	313	641	45.360001	13422.75
325	633	54	13415.25	314	641	46.080002	13422.75
326	633	54.720001	13415.25	315	641	46.799999	13422.75
327	632	55.439999	13416.25	316	641	47.52	13422.75
328	632	56.16	13416.25	317	641	48.240002	13422.75
329	631	56.880001	13415.5	318	641	48.959999	13422.75
330	631	57.599998	13415.5	319	641	49.68	13422.75
331	631	58.32	13415.5	320	641	50.400002	13422.75
332	631	59.040001	13415.5	321	641	51.119999	13422.75
333	631	59.759998	13415.5	322	641	51.84	13422.75
334	631	60.48	13415.5	323	641	52.560001	13422.75
335	631	61.200001	13415.5	324	641	53.279999	13422.75
336	631	61.919998	13415.5	325	641	54	13422.75
337	631	62.639999	13415.5	326	641	54.720001	13422.75
338	631	63.360001	13415.5	327	641	55.439999	13422.75
339	631	64.080002	13415.5	328	641	56.16	13422.75
340	631	64.800003	13415.5	329	641	56.880001	13422.75
341	631	65.519997	13415.5	330	641	57.599998	13422.75
342	631	66.239998	13415.5	331	641	58.32	13422.75
343	630	66.959999	13416.25	331	640	58.32	13422
343	631	66.959999	13415.5	332	640	59.040001	13422
344	631	67.68	13415.5	333	640	59.759998	13422
345	631	68.400002	13415.5	334	640	60.48	13422
346	631	69.120003	13415.5	335	640	61.200001	13422
347	631	69.839996	13415.5	336	640	61.919998	13422
348	631	70.559998	13415.5	337	640	62.639999	13422
349	631	71.279999	13415.5	338	640	63.360001	13422
350	631	72	13415.5	339	640	64.080002	13422
351	631	72.720001	13415.5	339	639	64.080002	13423
352	631	73.440002	13415.5	340	639	64.800003	13423
353	631	74.160004	13415.5	341	639	65.519997	13423
354	631	74.879997	13415.5	342	639	66.239998	13423
355	631	75.599998	13415.5	343	639	66.959999	13423
356	631	76.32	13415.5	344	639	67.68	13423
357	631	77.040001	13415.5	344	638	67.68	13422.5
358	631	77.760002	13415.5	345	638	68.400002	13422.5
359	631	78.480003	13415.5	346	638	69.120003	13422.5
360	631	79.199997	13415.5	347	638	69.839996	13422.5
361	631	79.919998	13415.5	348	638	70.559998	13422.5

362	631	80.639999	13415.5	349	638	71.279999	13422.5
362	632	80.639999	13416.25	350	638	72	13422.5
363	632	81.360001	13416.25	350	637	72	13420.5
363	633	81.360001	13415.25	351	637	72.720001	13420.5
364	633	82.080002	13415.25	352	637	73.440002	13420.5
365	633	82.800003	13415.25	353	637	74.160004	13420.5
366	633	83.519997	13415.25	354	637	74.879997	13420.5
367	633	84.239998	13415.25	355	637	75.599998	13420.5
368	633	84.959999	13415.25	355	636	75.599998	13420
369	633	85.68	13415.25	356	636	76.32	13420
370	633	86.400002	13415.25	357	636	77.040001	13420
371	633	87.120003	13415.25	358	636	77.760002	13420
372	632	87.839996	13416.25	359	636	78.480003	13420
373	632	88.559998	13416.25	360	636	79.199997	13420
373	633	88.559998	13415.25	361	637	79.919998	13420.5
373	634	88.559998	13417.5	362	637	80.639999	13420.5
374	634	89.279999	13417.5	363	637	81.360001	13420.5
375	634	90	13417.5	364	637	82.080002	13420.5
376	634	90.720001	13417.5	365	637	82.800003	13420.5
377	634	91.440002	13417.5	366	637	83.519997	13420.5
378	634	92.160004	13417.5	367	637	84.239998	13420.5
379	634	92.879997	13417.5	368	637	84.959999	13420.5
380	634	93.599998	13417.5	369	637	85.68	13420.5
381	634	94.32	13417.5	370	637	86.400002	13420.5
382	634	95.040001	13417.5	371	637	87.120003	13420.5
383	634	95.760002	13417.5	372	637	87.839996	13420.5
383	635	95.760002	13418	373	637	88.559998	13420.5
384	635	96.480003	13418	374	637	89.279999	13420.5
385	635	97.199997	13418	375	638	90	13422.5
386	635	97.919998	13418	376	638	90.720001	13422.5
387	635	98.639999	13418	377	638	91.440002	13422.5
388	635	99.360001	13418	378	638	92.160004	13422.5
389	635	100.080002	13418	379	638	92.879997	13422.5
390	635	100.800003	13418	380	638	93.599998	13422.5
391	634	101.519997	13417.5	380	637	93.599998	13420.5
392	634	102.239998	13417.5	381	637	94.32	13420.5
393	634	102.959999	13417.5	382	637	95.040001	13420.5
394	634	103.68	13417.5	383	637	95.760002	13420.5
394	635	103.68	13418	384	637	96.480003	13420.5
395	635	104.400002	13418	385	637	97.199997	13420.5
396	635	105.120003	13418	386	637	97.919998	13420.5
397	635	105.839996	13418	387	637	98.639999	13420.5
398	635	106.559998	13418	388	637	99.360001	13420.5
399	635	107.279999	13418	389	637	100.080002	13420.5
400	635	108	13418	390	637	100.800003	13420.5
401	635	108.720001	13418	391	637	101.519997	13420.5
402	635	109.440002	13418	392	638	102.239998	13422.5
403	635	110.160004	13418	393	638	102.959999	13422.5
404	635	110.879997	13418	394	638	103.68	13422.5
405	635	111.599998	13418	395	638	104.400002	13422.5

406	635	112.32	13418	396	638	105.120003	13422.5
407	635	113.040001	13418	397	639	105.839996	13423
408	634	113.760002	13417.5	398	639	106.559998	13423
409	634	114.480003	13417.5	399	639	107.279999	13423
410	634	115.199997	13417.5	400	639	108	13423
411	634	115.919998	13417.5	401	639	108.720001	13423
412	634	116.639999	13417.5	402	640	109.440002	13422
413	634	117.360001	13417.5	403	640	110.160004	13422
413	635	117.360001	13418	404	640	110.879997	13422
414	635	118.080002	13418	405	640	111.599998	13422
415	635	118.800003	13418	406	640	112.32	13422
416	635	119.519997	13418	407	640	113.040001	13422
416	636	119.519997	13420	408	640	113.760002	13422
417	636	120.239998	13420	409	640	114.480003	13422
417	637	120.239998	13420.5	410	640	115.199997	13422
418	637	120.959999	13420.5	411	640	115.919998	13422
419	637	121.68	13420.5	412	640	116.639999	13422
420	637	122.400002	13420.5	413	640	117.360001	13422
421	637	123.120003	13420.5	414	640	118.080002	13422
422	637	123.839996	13420.5	415	640	118.800003	13422
423	637	124.559998	13420.5	416	640	119.519997	13422
423	638	124.559998	13422.5	417	640	120.239998	13422
424	638	125.279999	13422.5	418	640	120.959999	13422
425	638	126	13422.5	419	640	121.68	13422
426	638	126.720001	13422.5	420	640	122.400002	13422
427	638	127.440002	13422.5	421	640	123.120003	13422
427	639	127.440002	13423	422	641	123.839996	13422.75
428	639	128.160004	13423	422	642	123.839996	13422
429	639	128.880005	13423	423	642	124.559998	13422
430	639	129.600006	13423	423	641	124.559998	13422.75
431	639	130.320007	13423	424	641	125.279999	13422.75
432	639	131.039993	13423	425	641	126	13422.75
433	639	131.759995	13423	426	641	126.720001	13422.75
433	640	131.759995	13422	427	641	127.440002	13422.75
434	640	132.479996	13422	428	641	128.160004	13422.75
435	640	133.199997	13422	429	641	128.880005	13422.75
435	641	133.199997	13422.75	430	641	129.600006	13422.75
436	641	133.919998	13422.75	431	641	130.320007	13422.75
437	641	134.639999	13422.75	432	641	131.039993	13422.75
438	641	135.360001	13422.75	433	641	131.759995	13422.75
438	642	135.360001	13422	434	641	132.479996	13422.75
439	642	136.080002	13422	435	641	133.199997	13422.75
440	642	136.800003	13422	436	641	133.919998	13422.75
441	641	137.520004	13422.75	437	642	134.639999	13422
442	641	138.240005	13422.75	438	642	135.360001	13422
443	641	138.960007	13422.75	439	643	136.080002	13424
444	640	139.679993	13422	440	643	136.800003	13424
445	640	140.399994	13422	441	644	137.520004	13426
446	639	141.119995	13423	442	644	138.240005	13426
447	639	141.839996	13423	443	644	138.960007	13426

448	639	142.559998	13423	444	644	139.679993	13426
449	638	143.279999	13422.5	445	644	140.399994	13426
450	638	144	13422.5	446	644	141.119995	13426
451	638	144.720001	13422.5	447	644	141.839996	13426
452	638	145.440002	13422.5	448	644	142.559998	13426
453	638	146.160004	13422.5	449	644	143.279999	13426
453	639	146.160004	13423	450	644	144	13426
453	640	146.160004	13422	451	644	144.720001	13426
454	640	146.880005	13422	452	644	145.440002	13426
455	640	147.600006	13422	453	644	146.160004	13426
455	641	147.600006	13422.75	454	644	146.880005	13426
456	641	148.320007	13422.75	455	644	147.600006	13426
457	641	149.039993	13422.75	456	645	148.320007	13426.5
457	642	149.039993	13422	457	645	149.039993	13426.5
458	642	149.759995	13422	458	645	149.759995	13426.5
459	642	150.479996	13422	459	646	150.479996	13425.75
460	642	151.199997	13422	460	646	151.199997	13425.75
461	642	151.919998	13422	461	646	151.919998	13425.75
462	642	152.639999	13422	462	647	152.639999	13426.25
463	642	153.360001	13422	463	647	153.360001	13426.25
464	642	154.080002	13422	464	647	154.080002	13426.25
465	642	154.800003	13422	465	648	154.800003	13425.5
466	642	155.520004	13422	466	648	155.520004	13425.5
467	642	156.240005	13422	467	648	156.240005	13425.5
468	642	156.960007	13422	468	648	156.960007	13425.5
469	642	157.679993	13422	469	649	157.679993	13427.75
470	642	158.399994	13422	470	649	158.399994	13427.75
471	642	159.119995	13422	471	649	159.119995	13427.75
472	642	159.839996	13422	472	650	159.839996	13428.25
473	642	160.559998	13422	473	650	160.559998	13428.25
474	642	161.279999	13422	474	650	161.279999	13428.25
475	642	162	13422	475	650	162	13428.25
476	642	162.720001	13422	476	650	162.720001	13428.25
477	642	163.440002	13422	477	650	163.440002	13428.25
478	642	164.160004	13422	478	651	164.160004	13430.25
478	643	164.160004	13424	479	652	164.880005	13430.75
479	643	164.880005	13424	480	652	165.600006	13430.75
480	643	165.600006	13424	481	652	166.320007	13430.75
481	643	166.320007	13424	482	652	167.039993	13430.75
481	644	166.320007	13426	483	652	167.759995	13430.75
482	644	167.039993	13426	484	653	168.479996	13433
483	644	167.759995	13426	485	653	169.199997	13433
484	644	168.479996	13426	486	653	169.919998	13433
485	644	169.199997	13426	487	654	170.639999	13432.25
485	645	169.199997	13426.5	488	654	171.360001	13432.25
486	645	169.919998	13426.5	489	654	172.080002	13432.25
487	645	170.639999	13426.5	490	654	172.800003	13432.25
488	645	171.360001	13426.5	491	654	173.520004	13432.25
489	645	172.080002	13426.5	492	654	174.240005	13432.25
490	645	172.800003	13426.5	493	654	174.960007	13432.25

490	646	172.800003	13425.75	494	654	175.679993	13432.25
491	646	173.520004	13425.75	495	655	176.399994	13434.5
491	647	173.520004	13426.25	496	655	177.119995	13434.5
492	647	174.240005	13426.25	497	655	177.839996	13434.5
492	648	174.240005	13425.5	498	655	178.559998	13434.5
493	648	174.960007	13425.5	499	655	179.279999	13434.5
494	648	175.679993	13425.5	500	656	180	13432.25
494	649	175.679993	13427.75				
495	649	176.399994	13427.75				
496	649	177.119995	13427.75				
497	649	177.839996	13427.75				
498	649	178.559998	13427.75				
498	650	178.559998	13428.25				
499	650	179.279999	13428.25				
500	649	180	13427.75				

B. Unrolled BSS images from boreholes 3-5 and 4-1

Table B.1 lists the orientations and joint set memberships of all of the joints from boreholes 3-5 and 4-1 which were used in this thesis. The joints are identified in images of the unrolled borehole walls.

Table B.1: List of joints

Joint Name	From Borehole	Dip & Dip Dir.	Joint Set	Joint Name	From Borehole	Dip & Dip Dir.	Joint Set
9-1	3-5	27/330	7	17-1	3-5	18/345	1
10-1	3-5	16/340	1	17-2	3-5	28/311	9
10-2	3-5	18/343	1	18-1	3-5	25/282	5
10-3	3-5	24/21	2	19-1	3-5	14/277	4
10-4	3-5	27/21	2	19-2	3-5	22/266	14
11-1	3-5	14/2	8	19-3	3-5	21/275	4
13-1	3-5	20/254	3	19-4	3-5	23/241	6
13-2	3-5	24/275	4	20-1	3-5	20/270	4
14-1	3-5	16/250	3	20-2	3-5	8/146	10
14-2	3-5	19/323	7	20-3	3-5	20/285	5
14-3	3-5	27/275	4	21-1	3-5	40/116	11
14-4	3-5	33/244	6	21-2	3-5	13/164	12
15-1	3-5	17/244	6	21-3	3-5	7/246	13
15-2	3-5	22/272	4	10-1	4-1	38/244	-
15-3	3-5	47/320	7	42-1	4-1	22/120	-
15-4	3-5	16/256	15	48-1	4-1	42/325	-
15-5	3-5	33/345	1	64-1	4-1	35/336	-

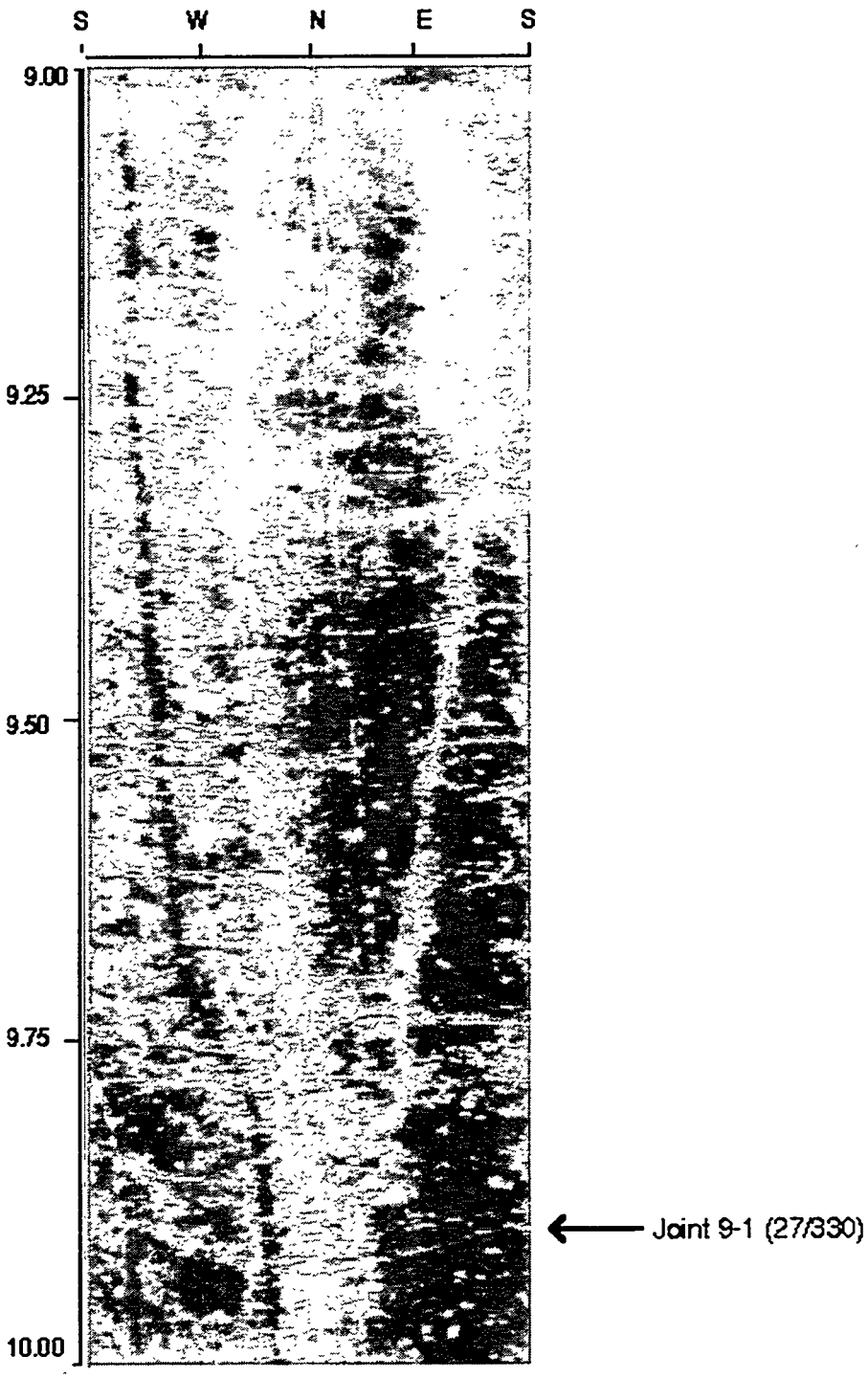

Figure B.1: Joints in unrolled image of 9 m. interval

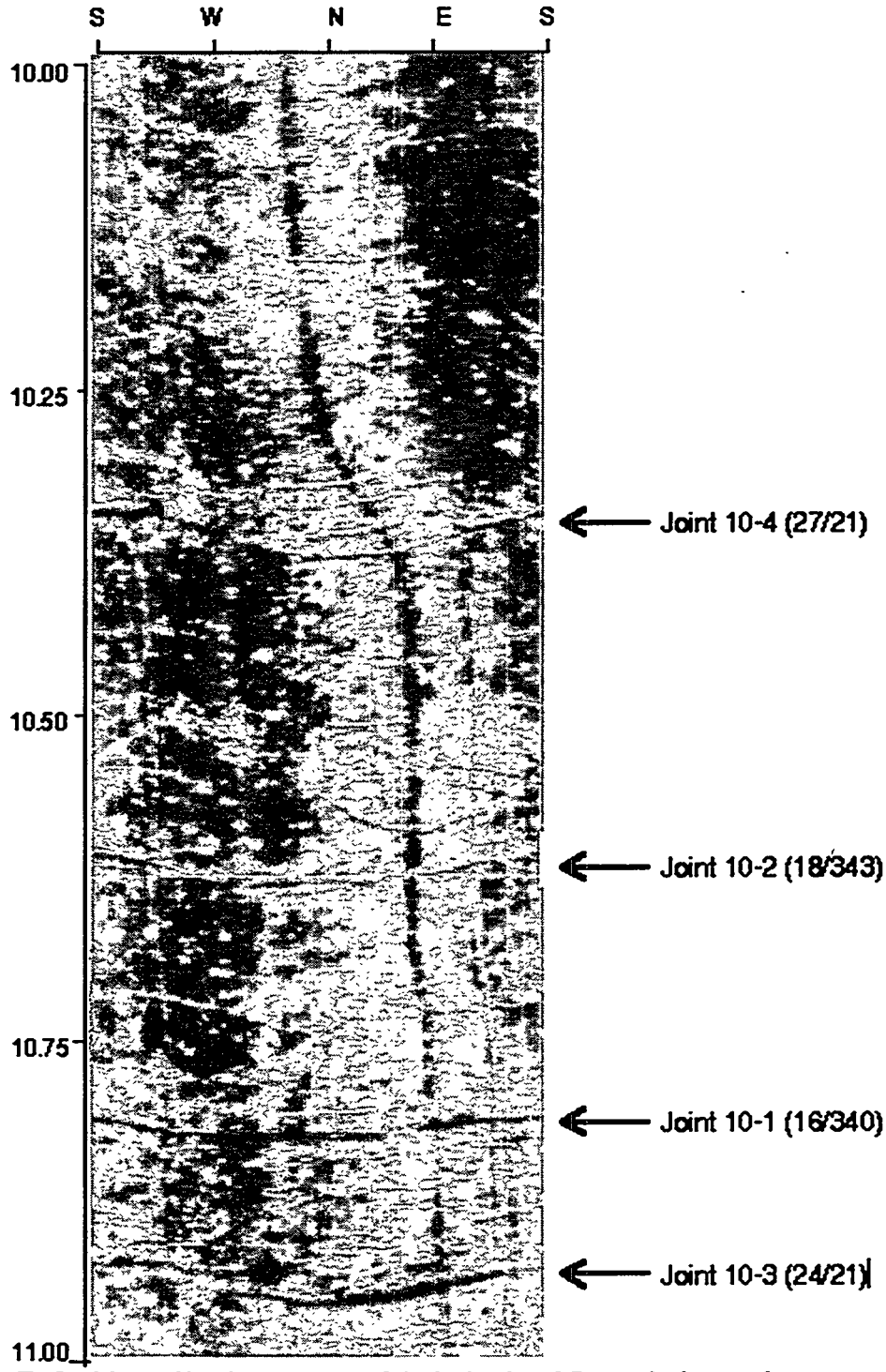

Figure B.2: Unrolled image of joints in 10 m. interval

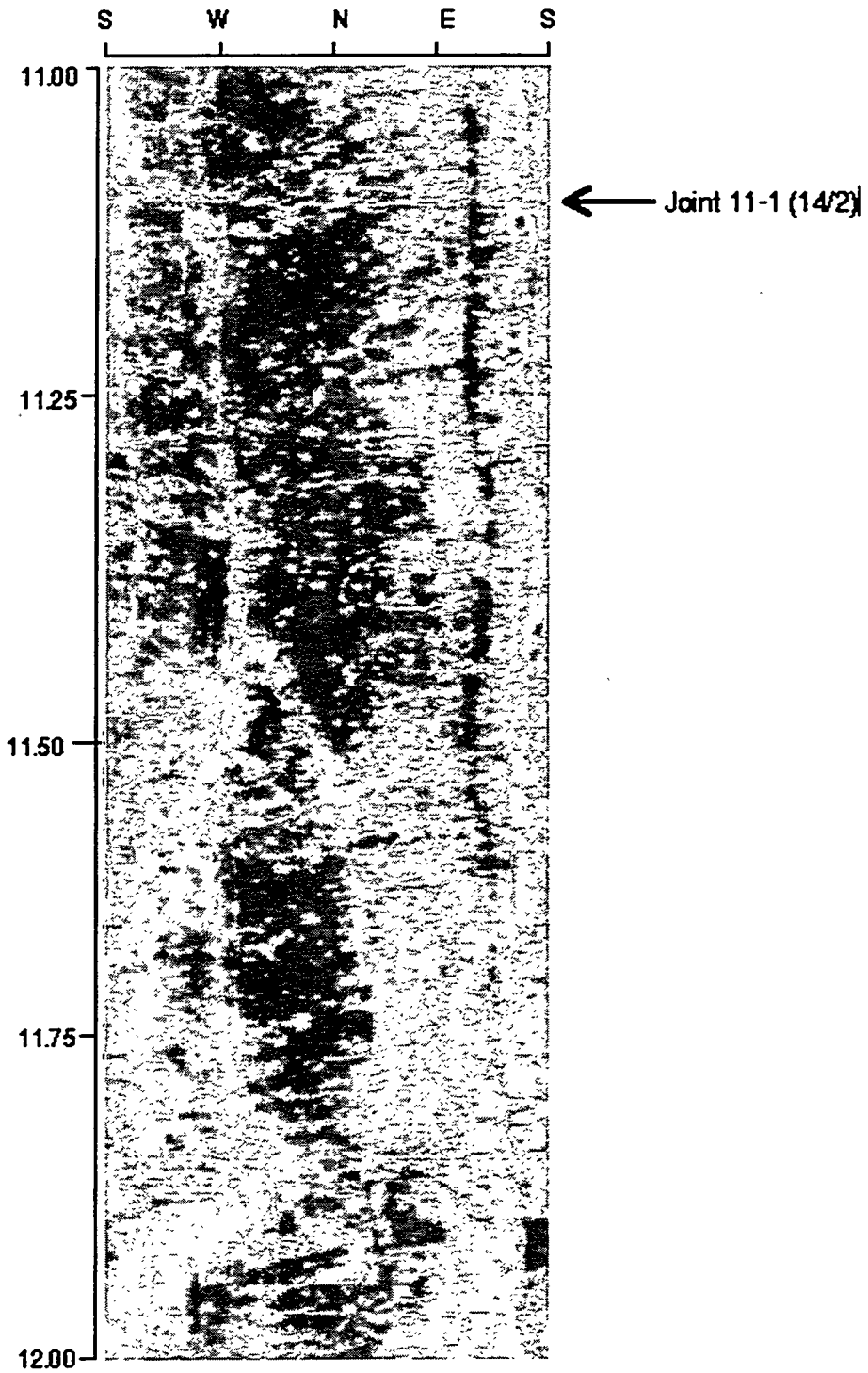

Figure B.3: Joints in unrolled image of 11 m. interval

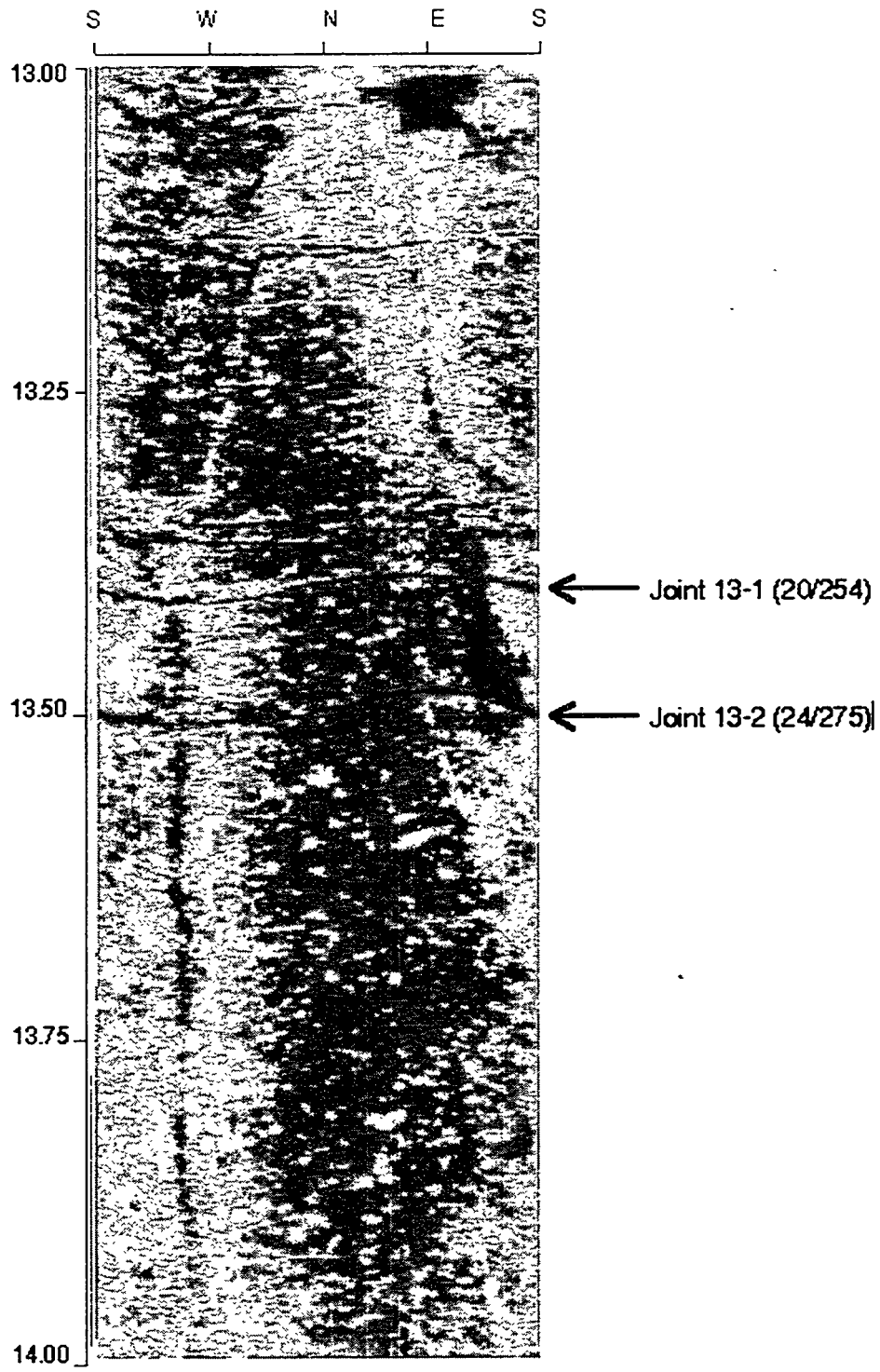

Figure B.4: Joints in unrolled image of 13 m. interval

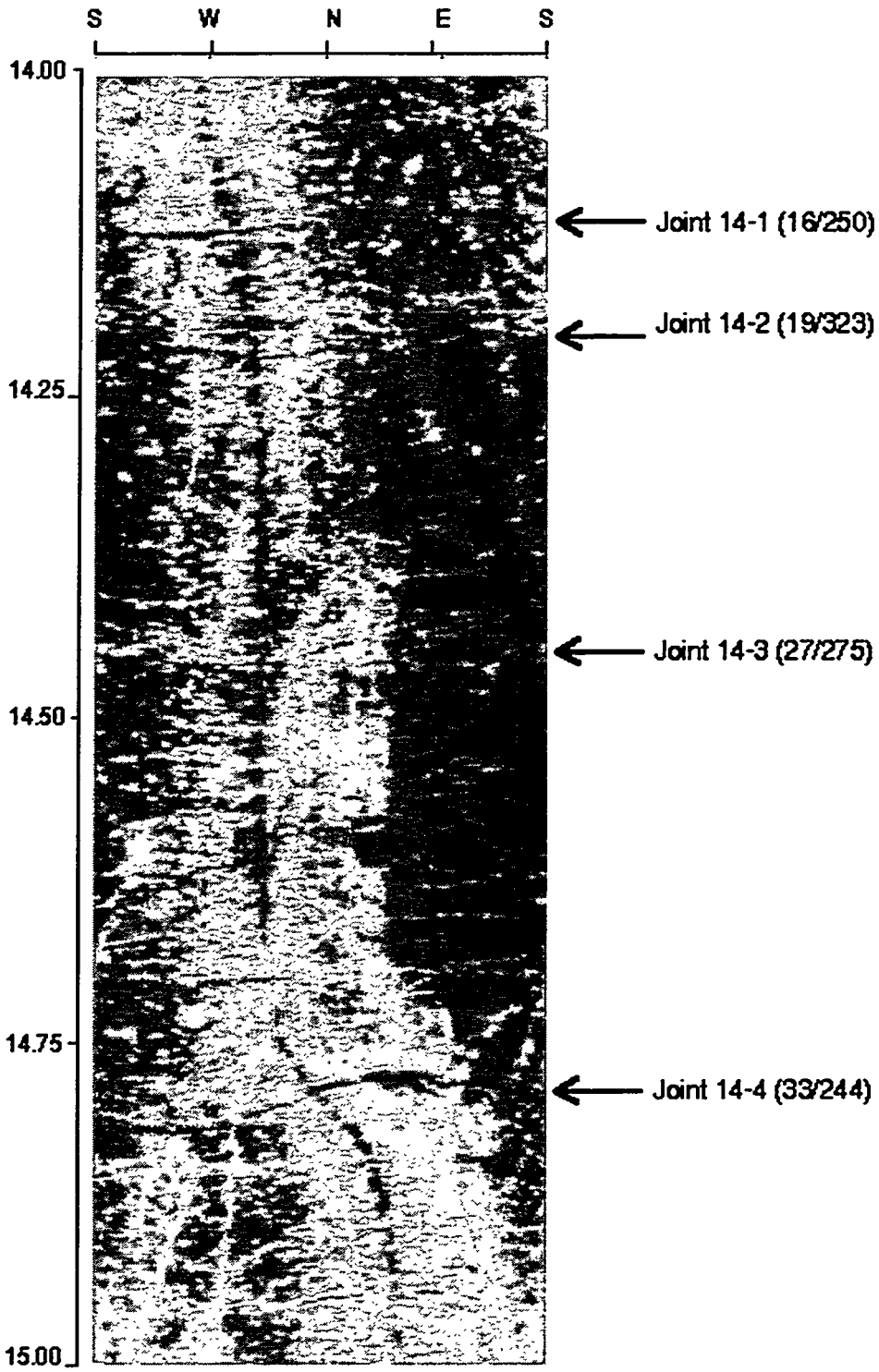

Figure B.5: Joints in unrolled image of 14 m. interval

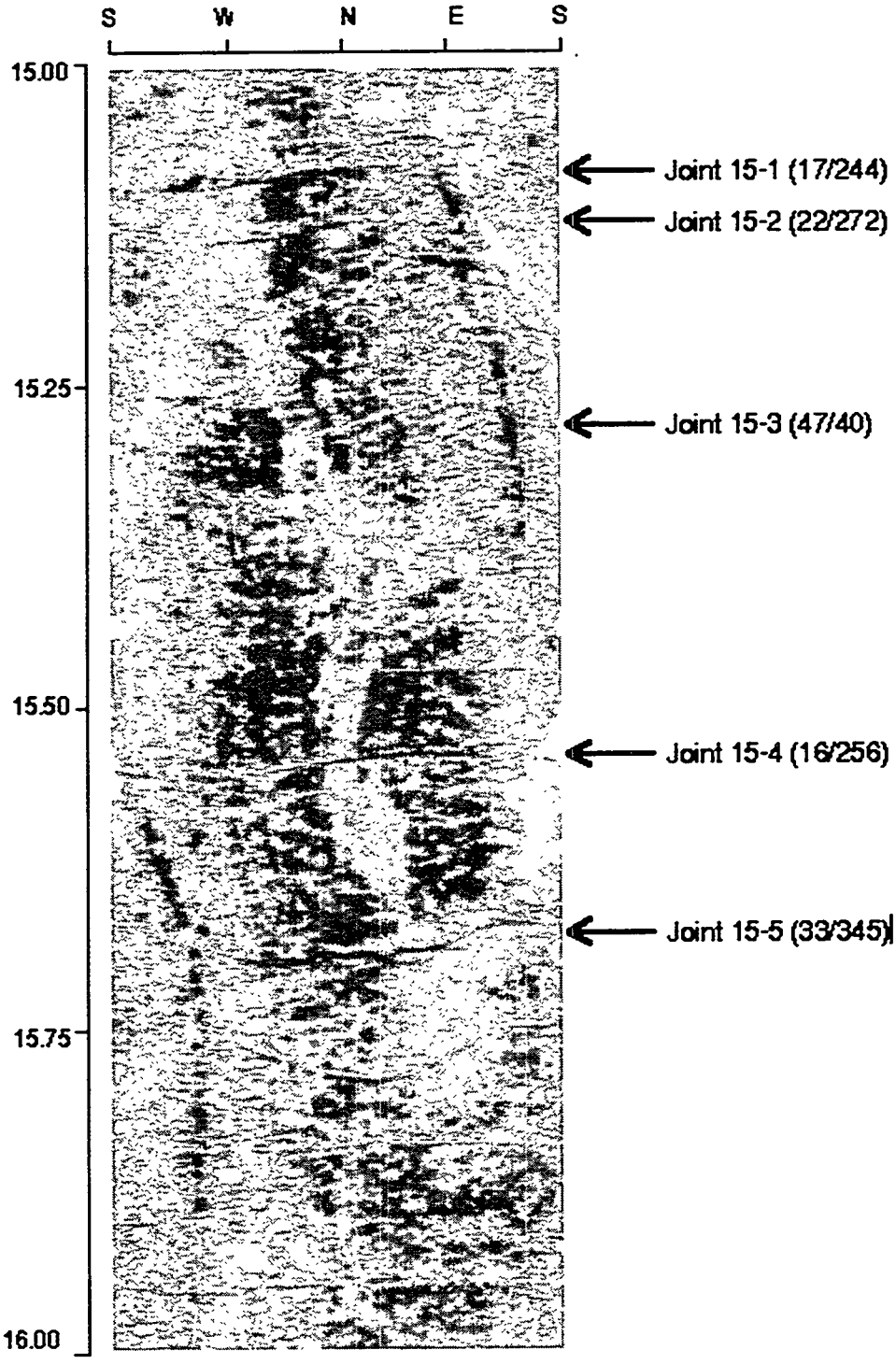

Figure B.6: Joints in unrolled image of 15 m. interval

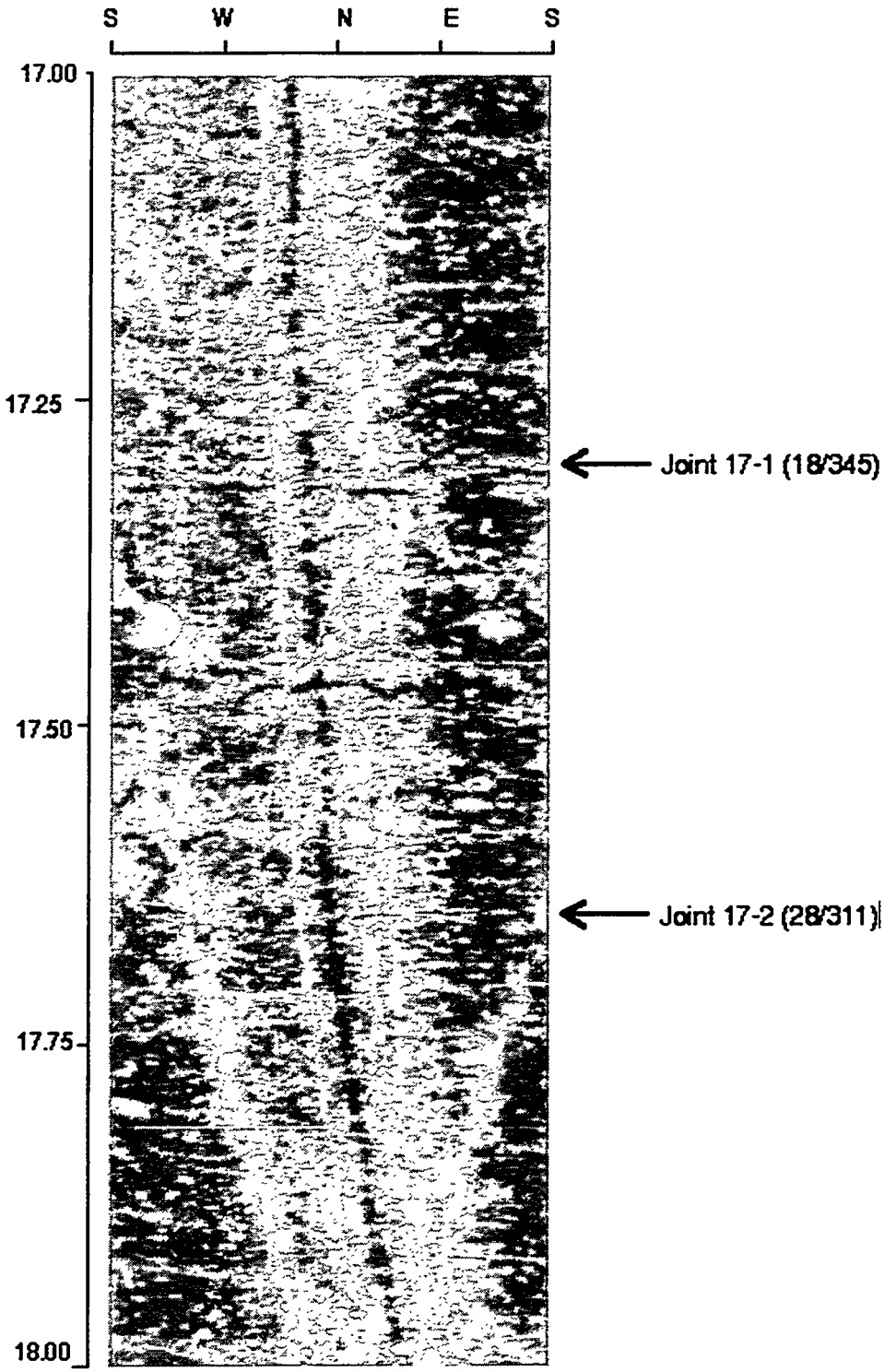

Figure B.7: Joints in unrolled image of 17 m. interval

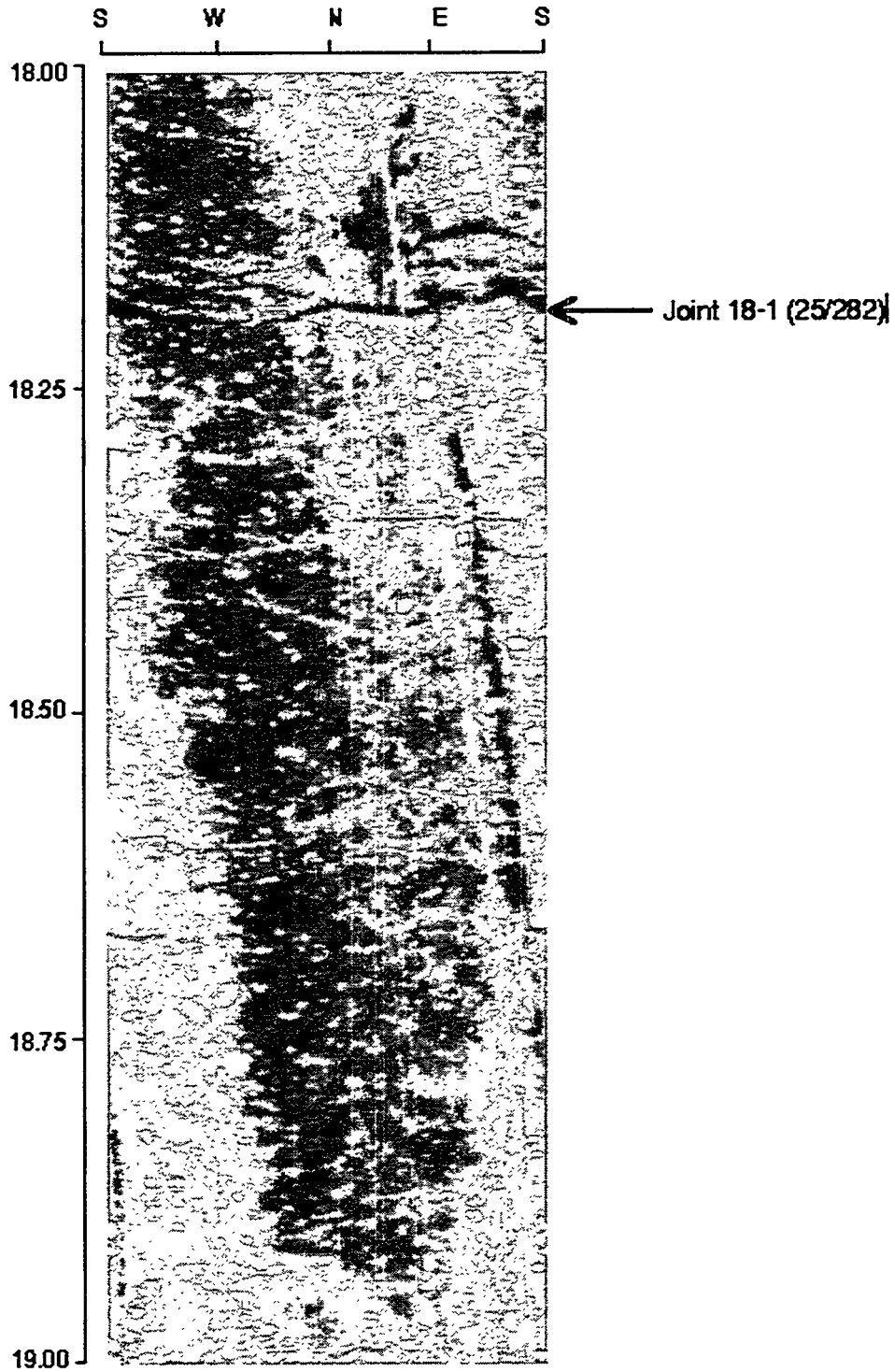

Figure B.8: Joints in unrolled image of 18 m. interval

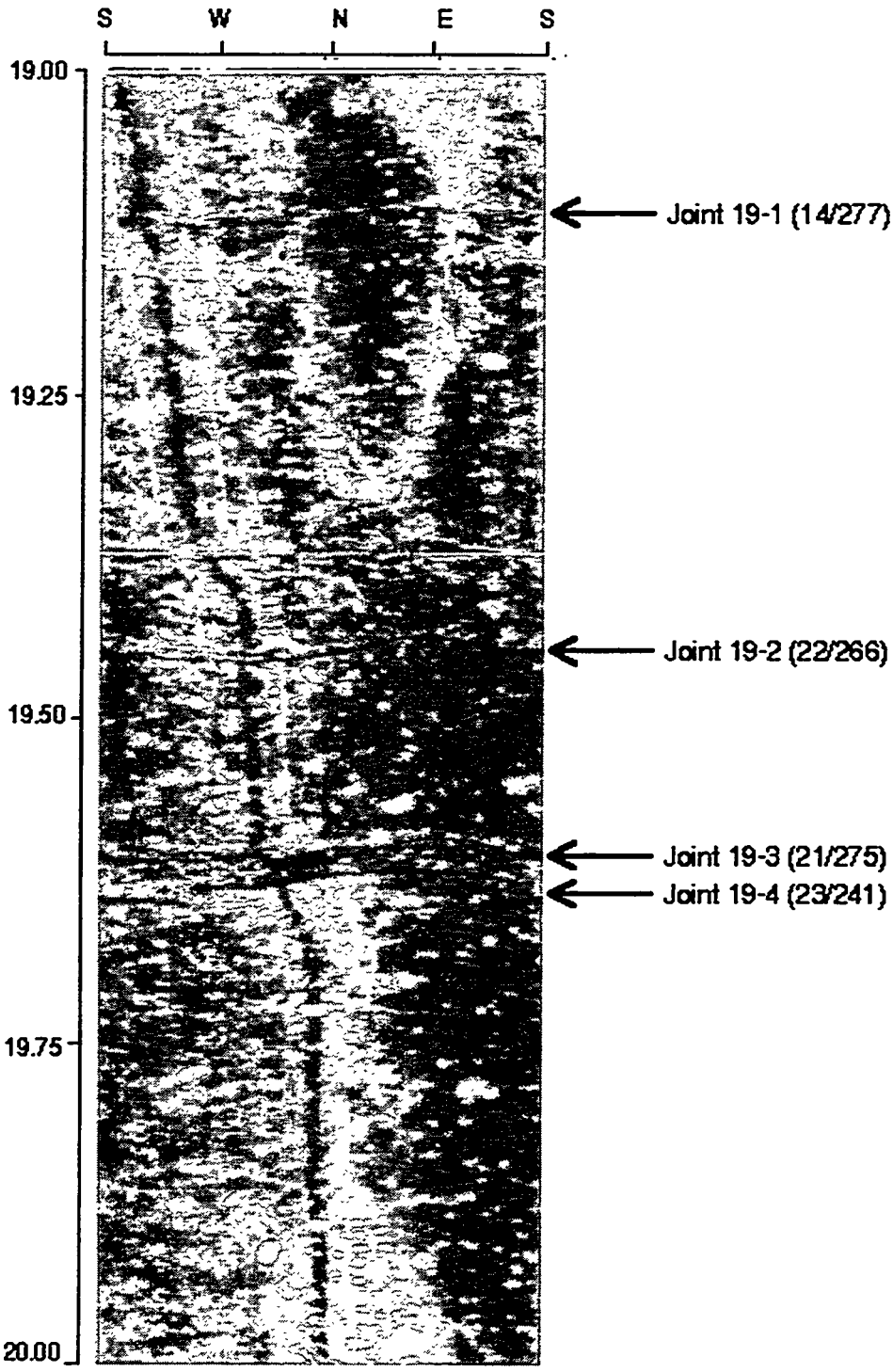

Figure B.9: Joints in unrolled image of 19 m. interval

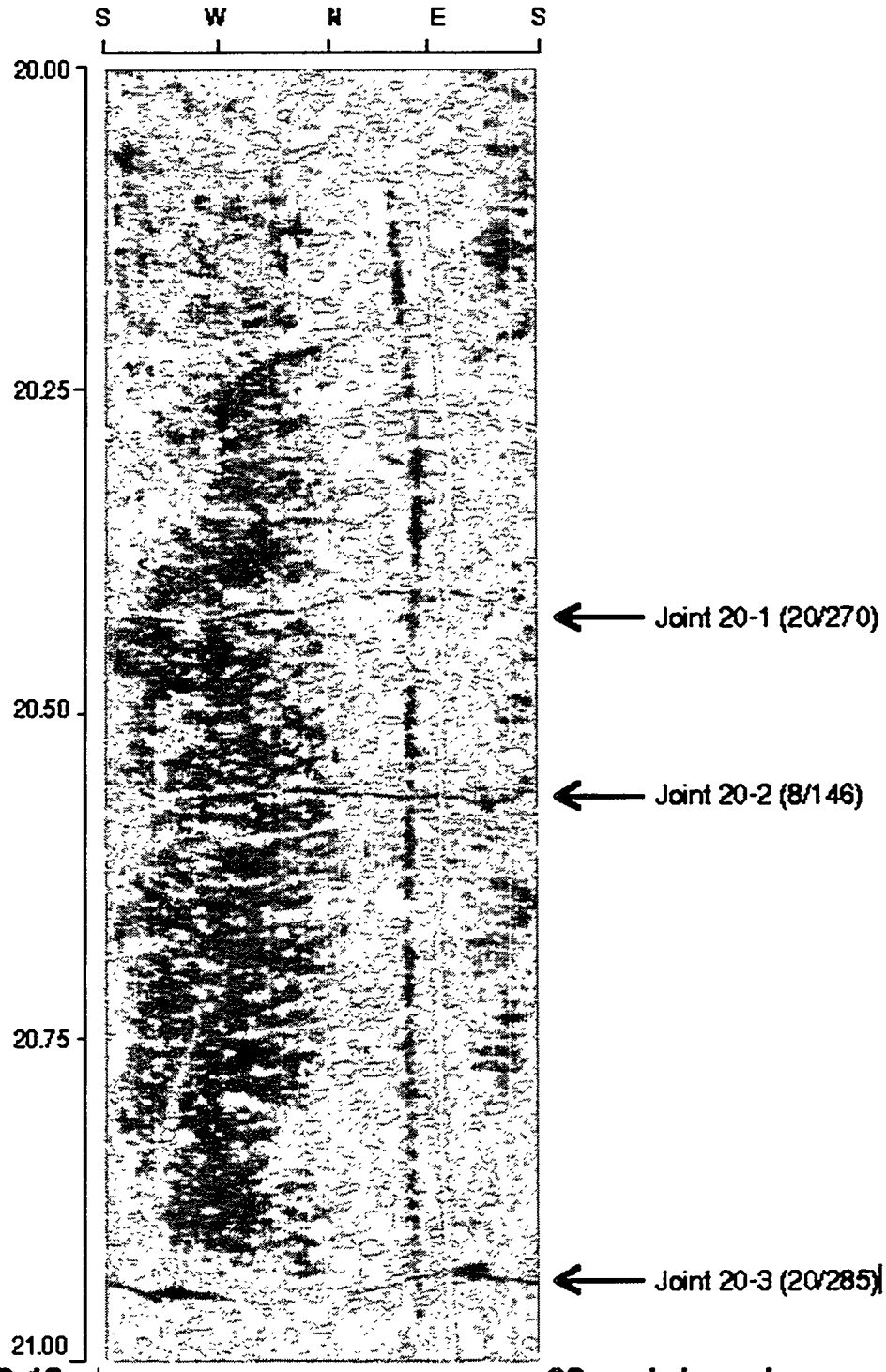

Figure B.10: Joints in unrolled image of 20 m. interval

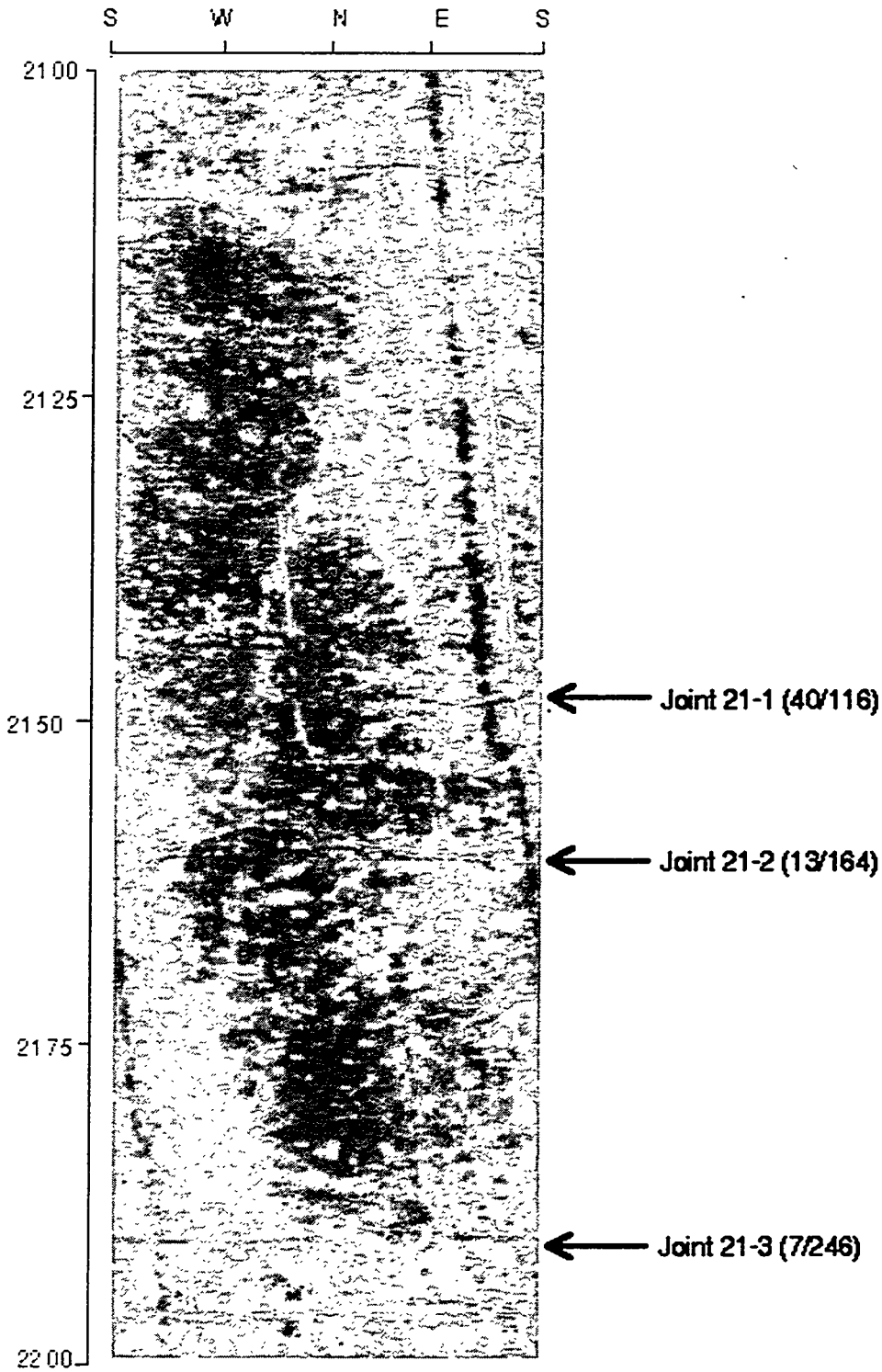

Figure B.11: Joints in unrolled image of 21 m. interval

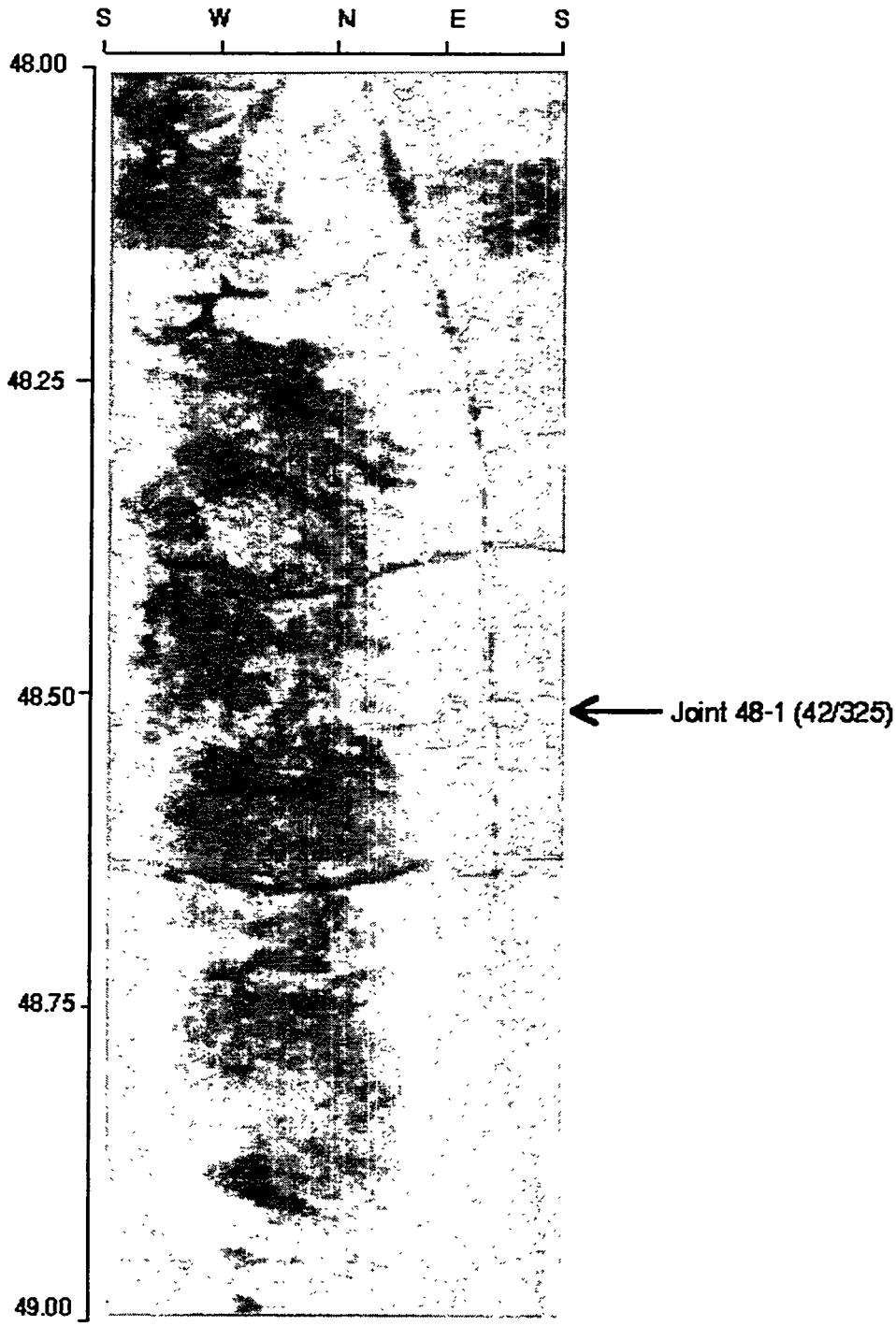

Figure B.12: Unrolled borehole wall image of 48 m. interval

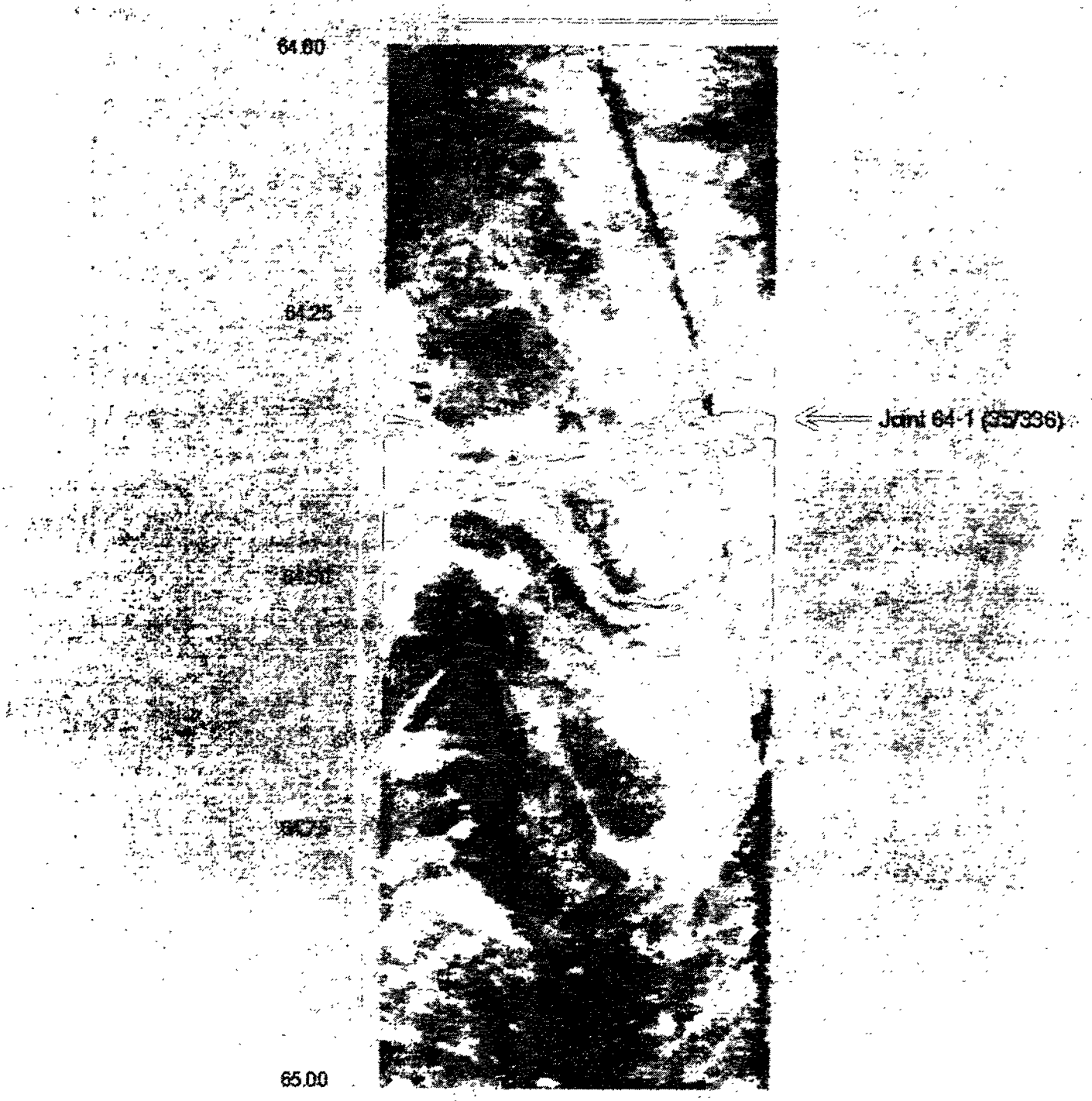

Figure B.13: Unrolled borehole wall image of 64 m. interval

C. Verification of Renger's envelope algorithm

Results from the analysis of the profile of a smooth plane intersected by a vertical borehole using envelope.c are presented in Figure C.1 below.

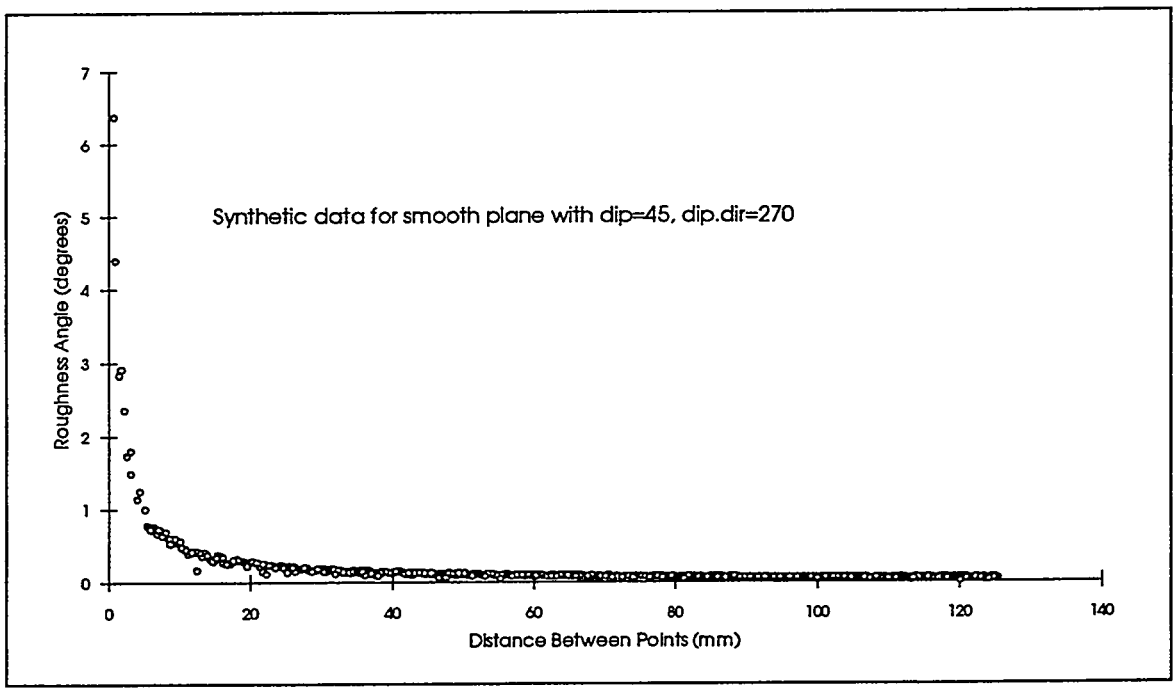

Figure C.1: Verification of Renger's envelope algorithm

D. Examples of Rengers envelopes of joints in borehole 3-5

Examples of Rengers envelopes for joints in borehole 3-5 which were computed using envelope.c are presented below.

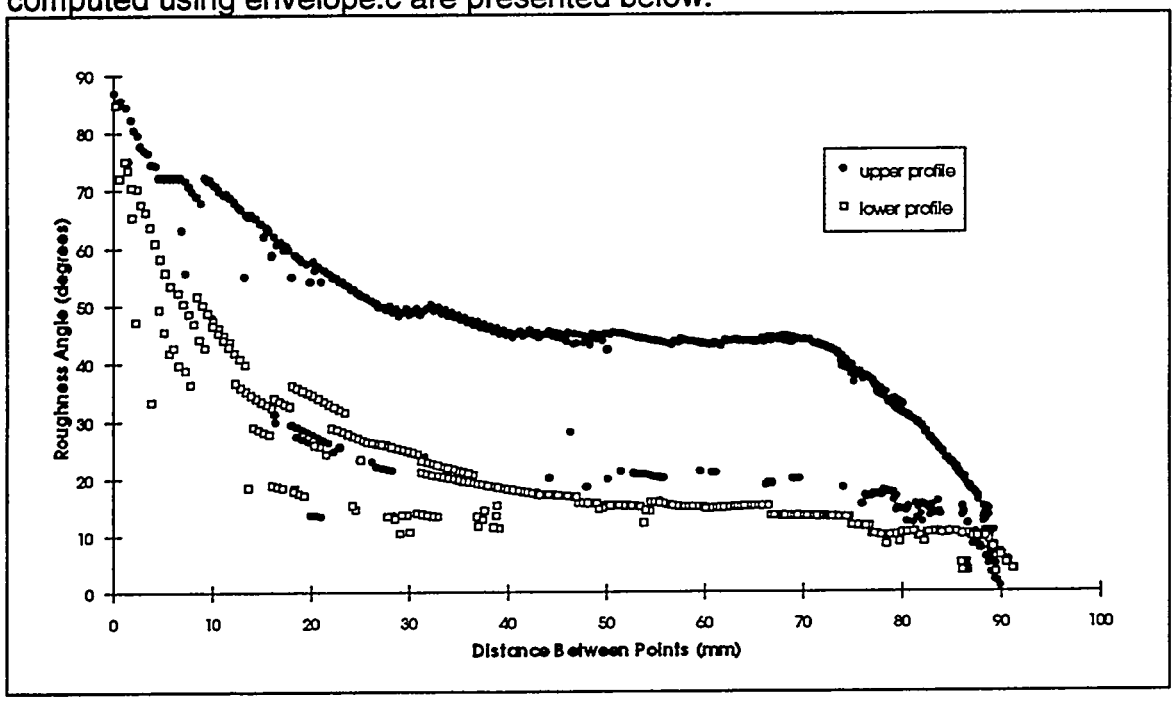

Figure D.1: Rengers envelopes for joint 10-2

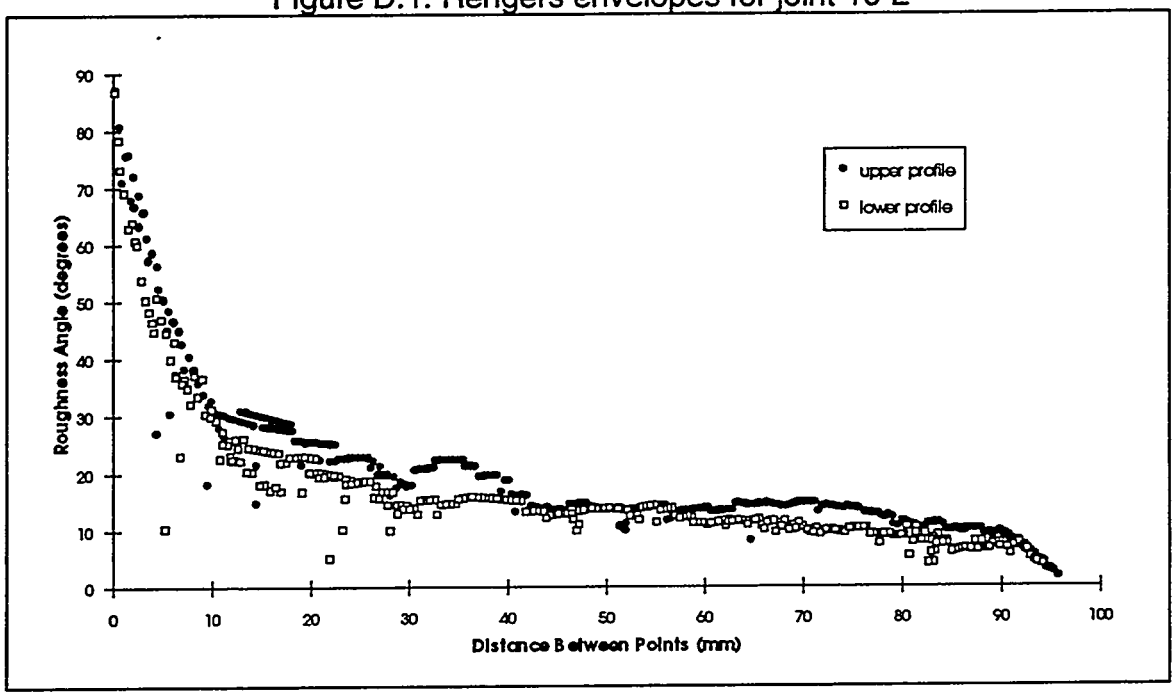

Figure D.2: Rengers envelopes for joint 10-3

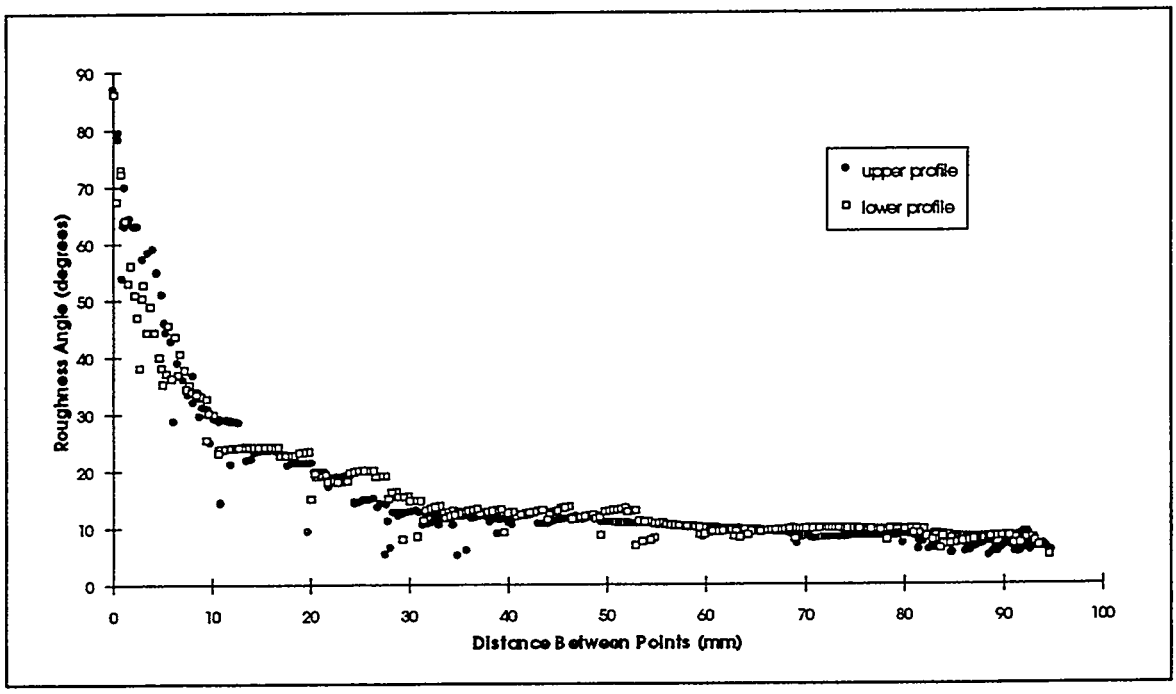

Figure D.3: Rengers envelopes for joint 10-4

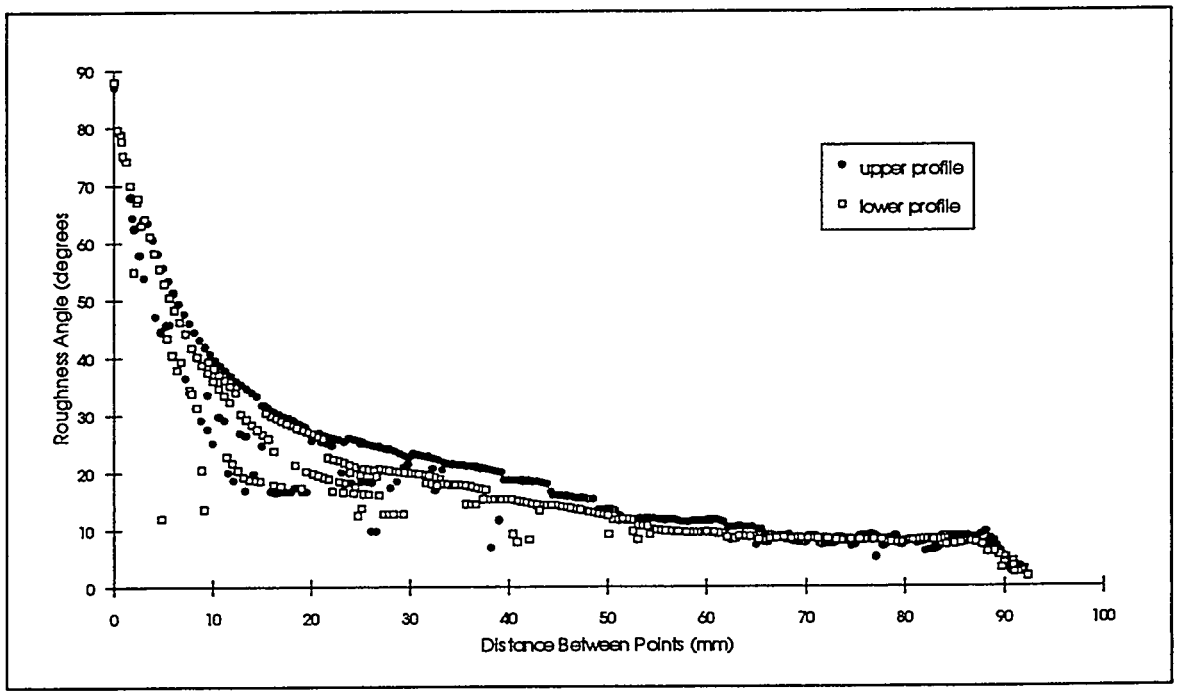

Figure D.4: Rengers envelopes for joint 14-1

E. Verification of anisotropy analysis algorithm

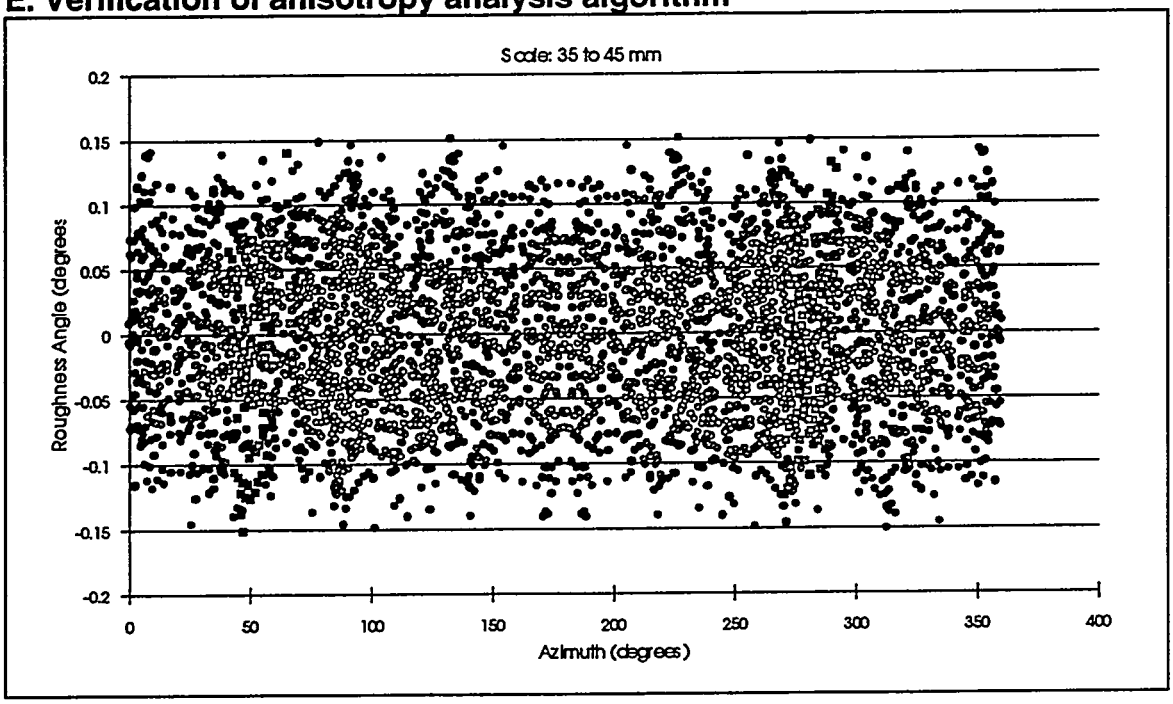

Figure E.1: Verification of anisotropy analysis algorithm for test case 1

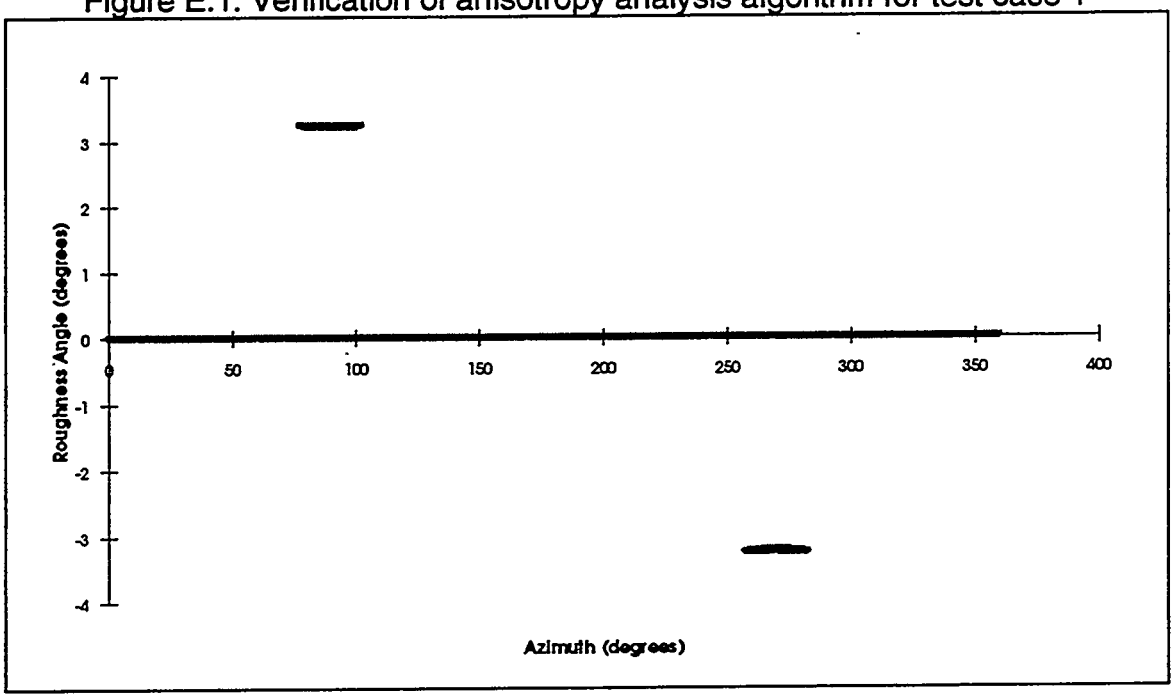

Figure E.2: Verification of anisotropy analysis algorithm for test case 2

F. Examples of anisotropy curves for borehole 3-5

Fig. F.1: Anisotropy curve for joint 9-1 upper profile

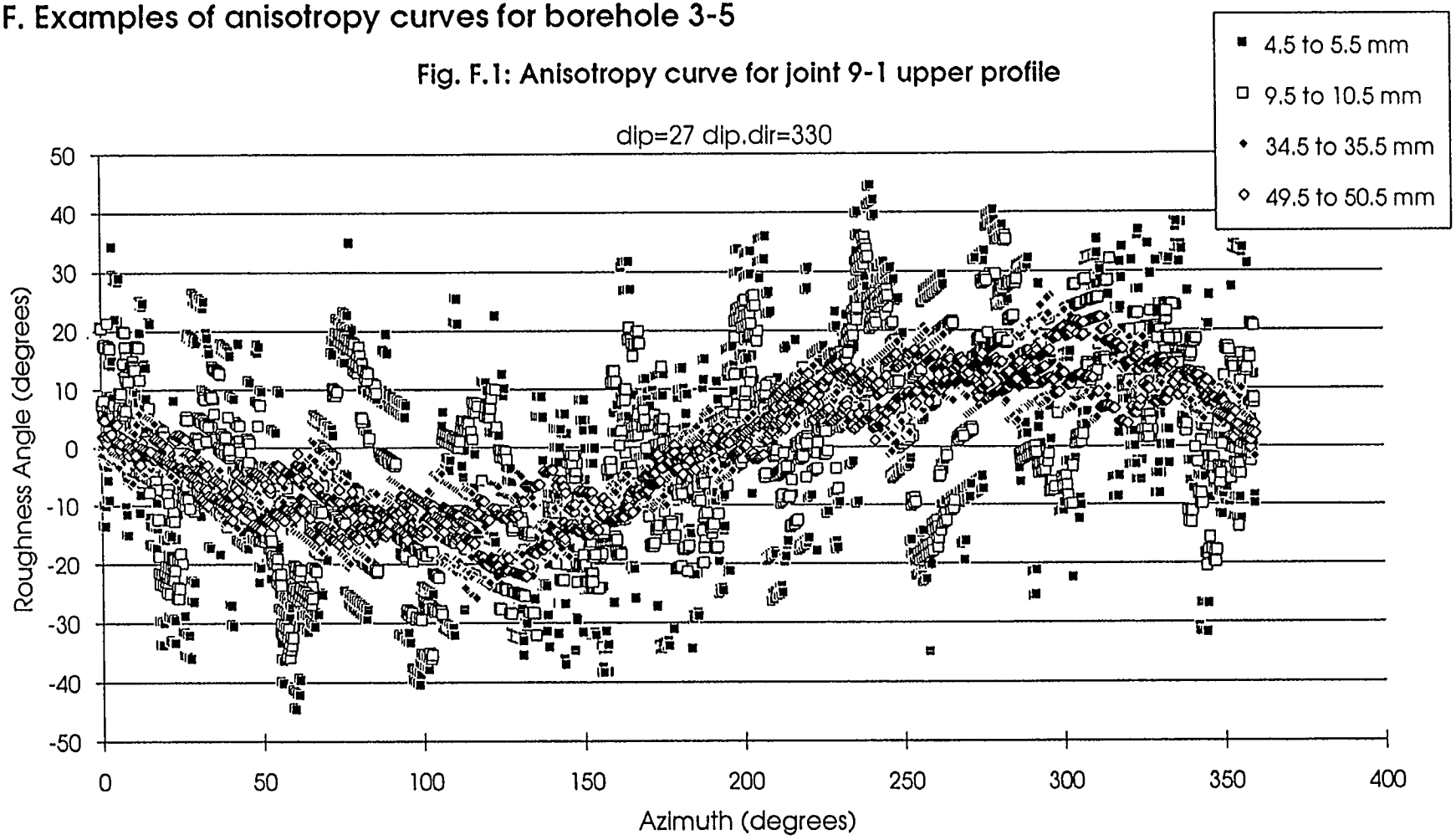

Fig. F.2: Anisotropy curve for joint 9-1 lower profile

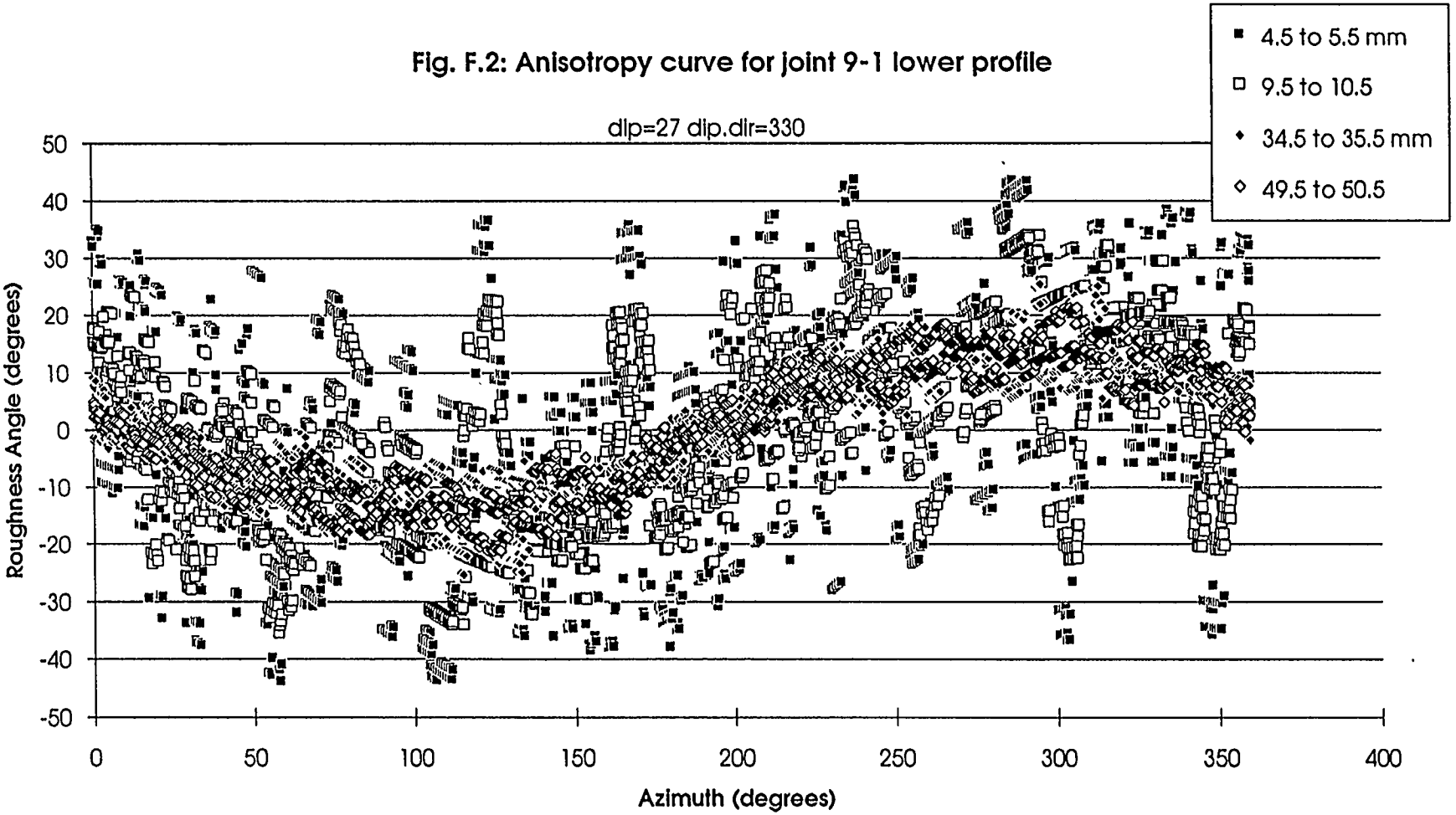

Fig. F.3: Anisotropy curve for joint 10-2 upper profile

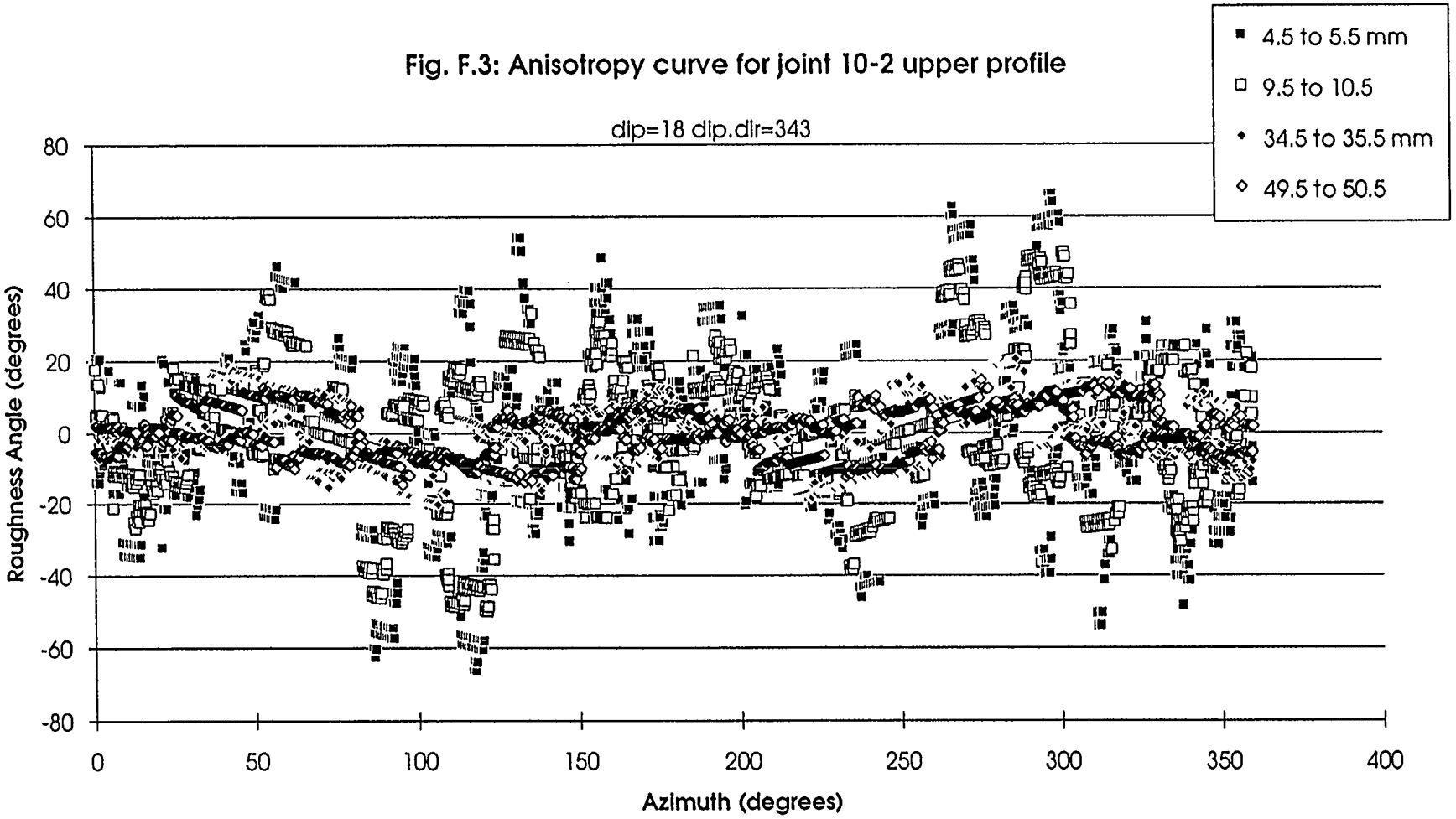

Fig. F.4: Anisotropy curve for joint 10-2 lower profile

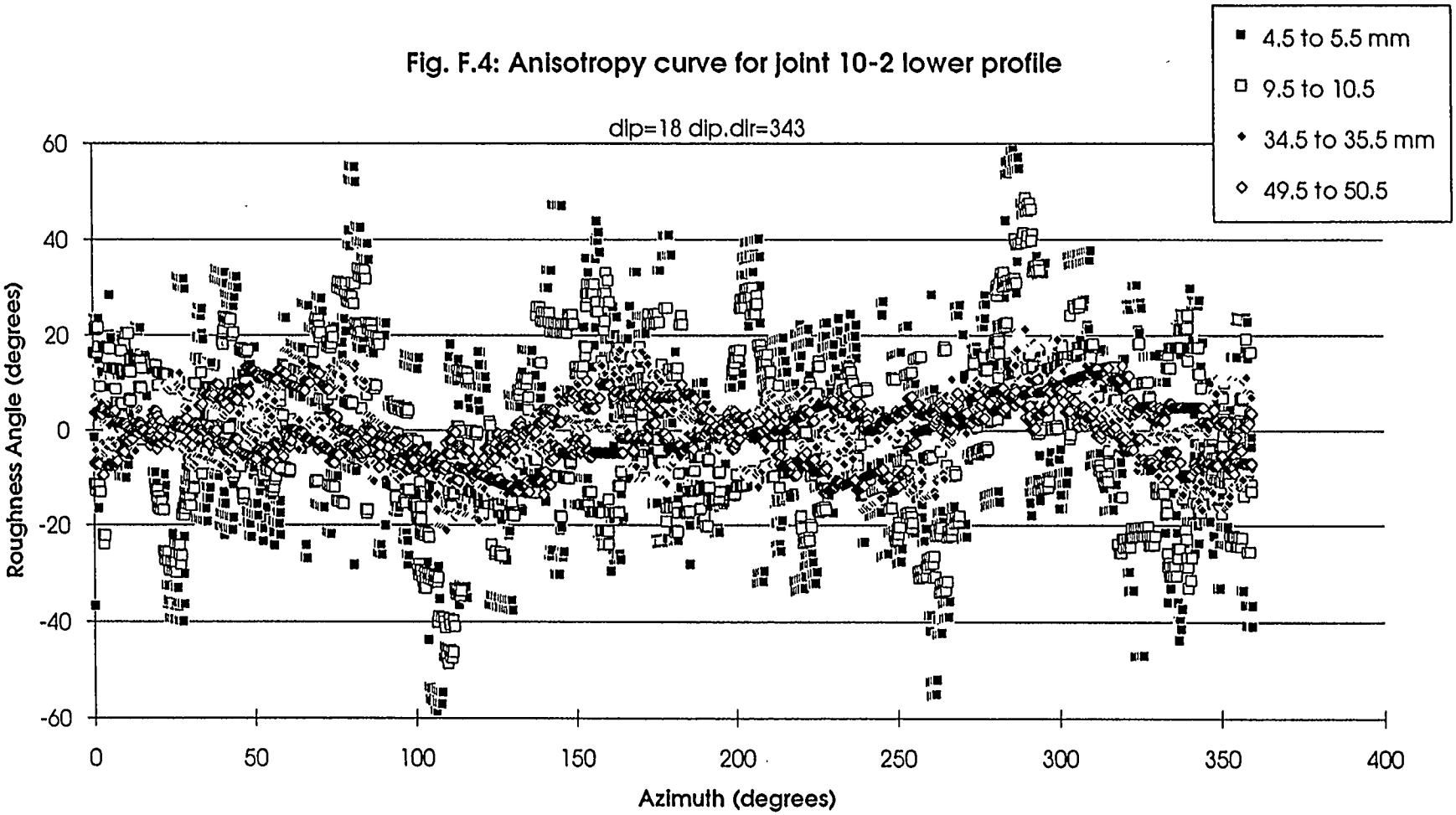

Fig. F.5: Anisotropy curve for joint 10-3 upper profile

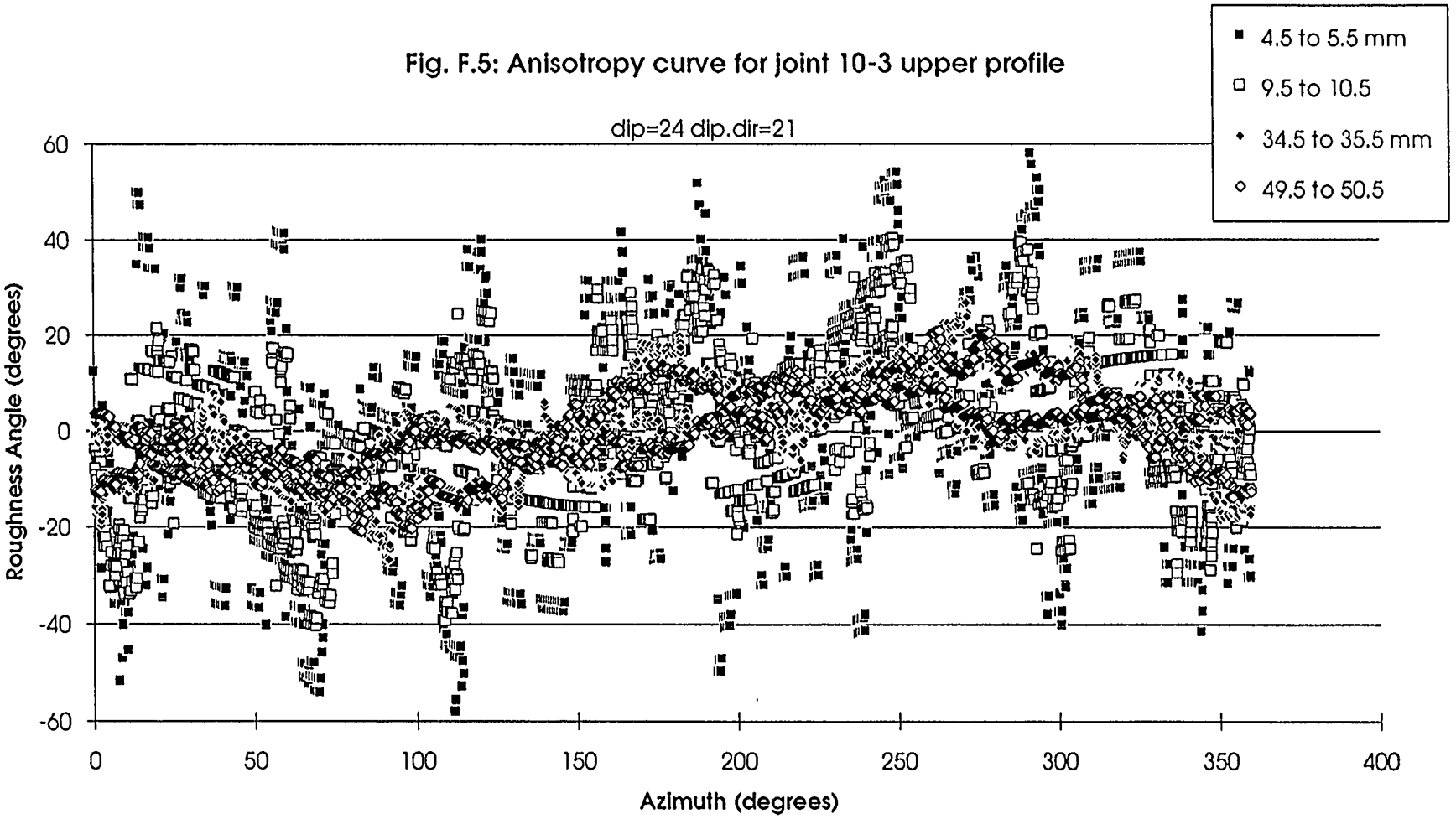

Fig. F.6: Anisotropy curve for joint 10-3 lower profile

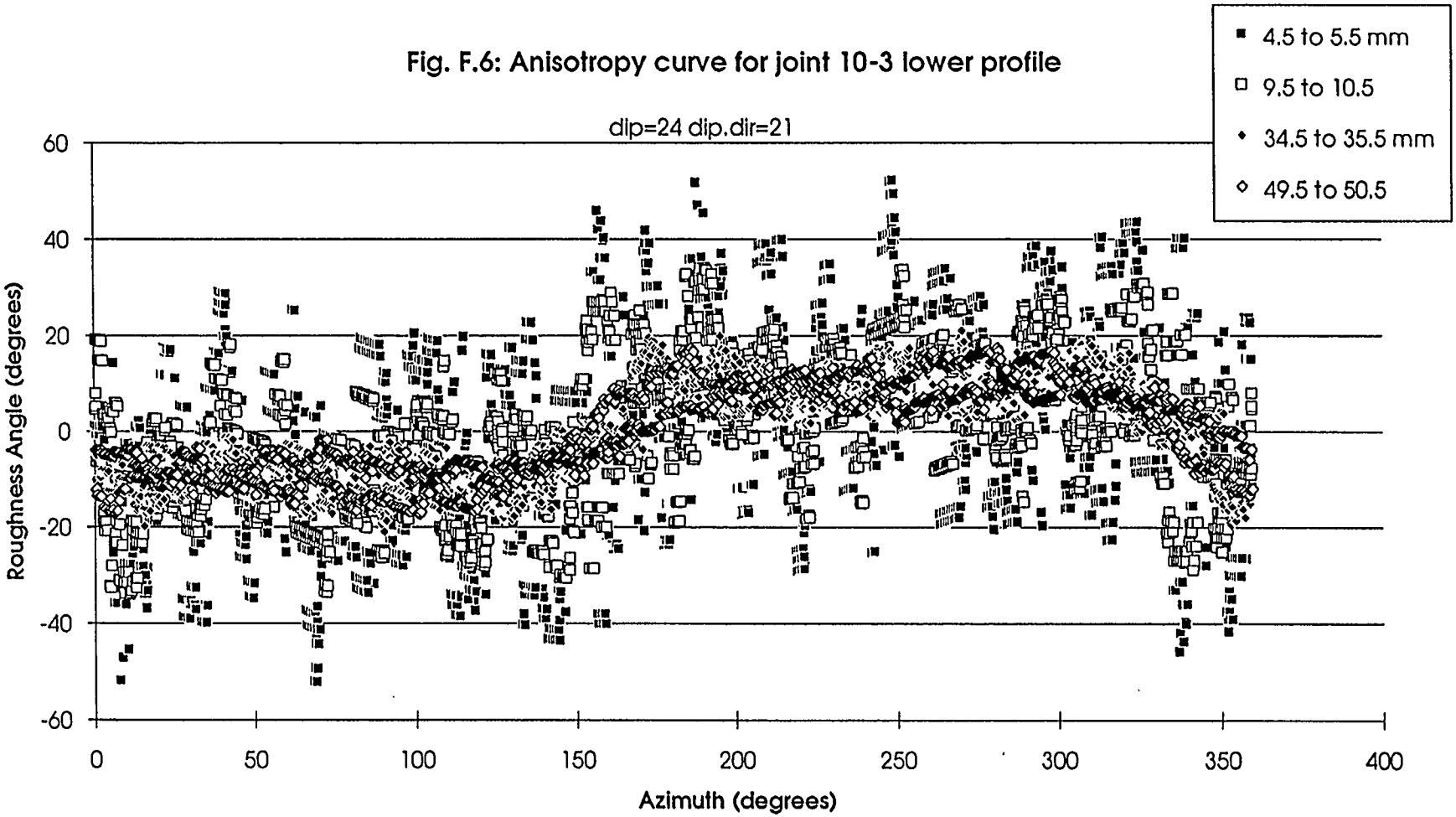

Fig. F.7: Anisotropy curve for joint 10-4 upper profile

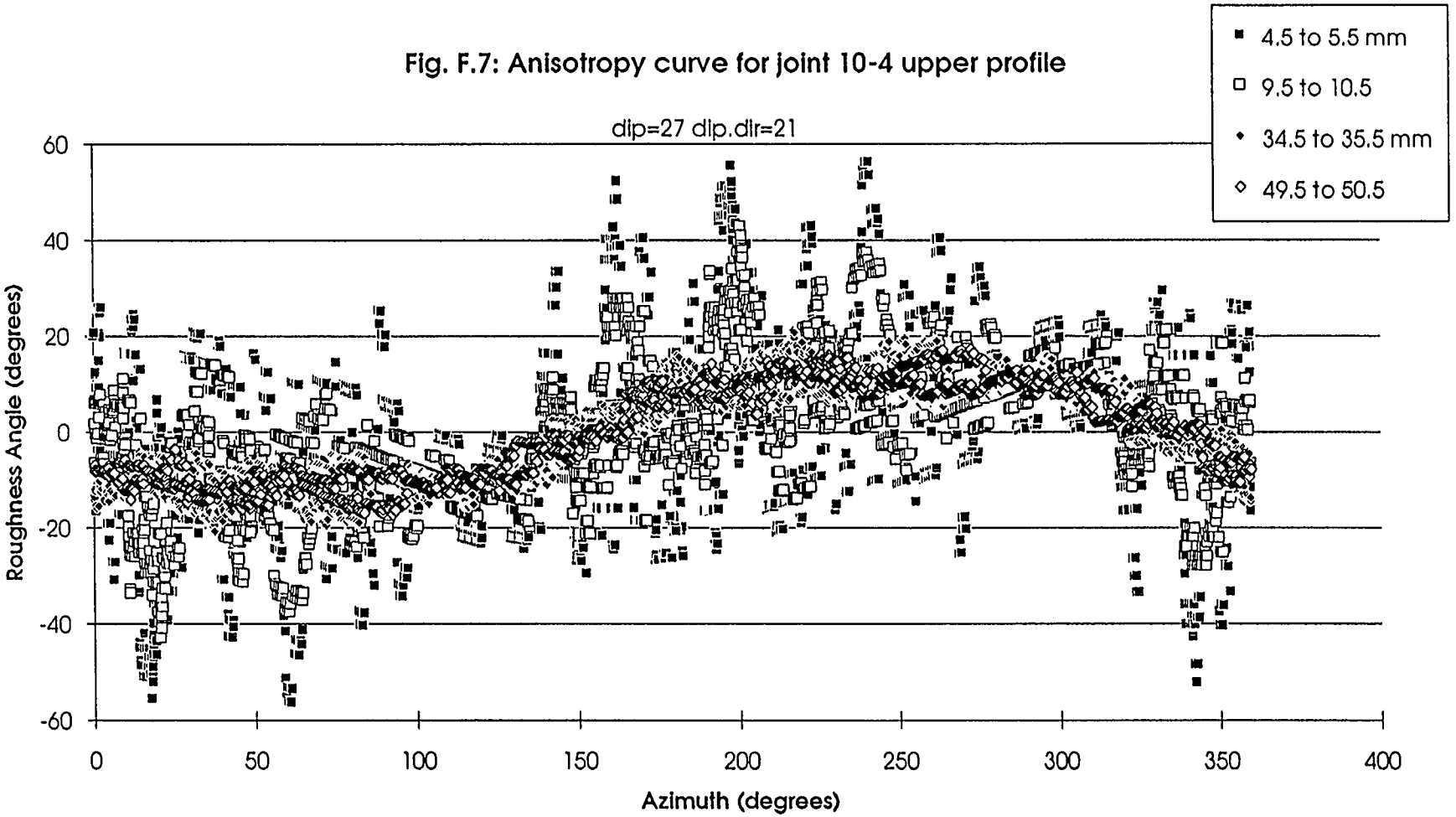

Fig. F.8: Anisotropy curve for joint 10-4 lower profile

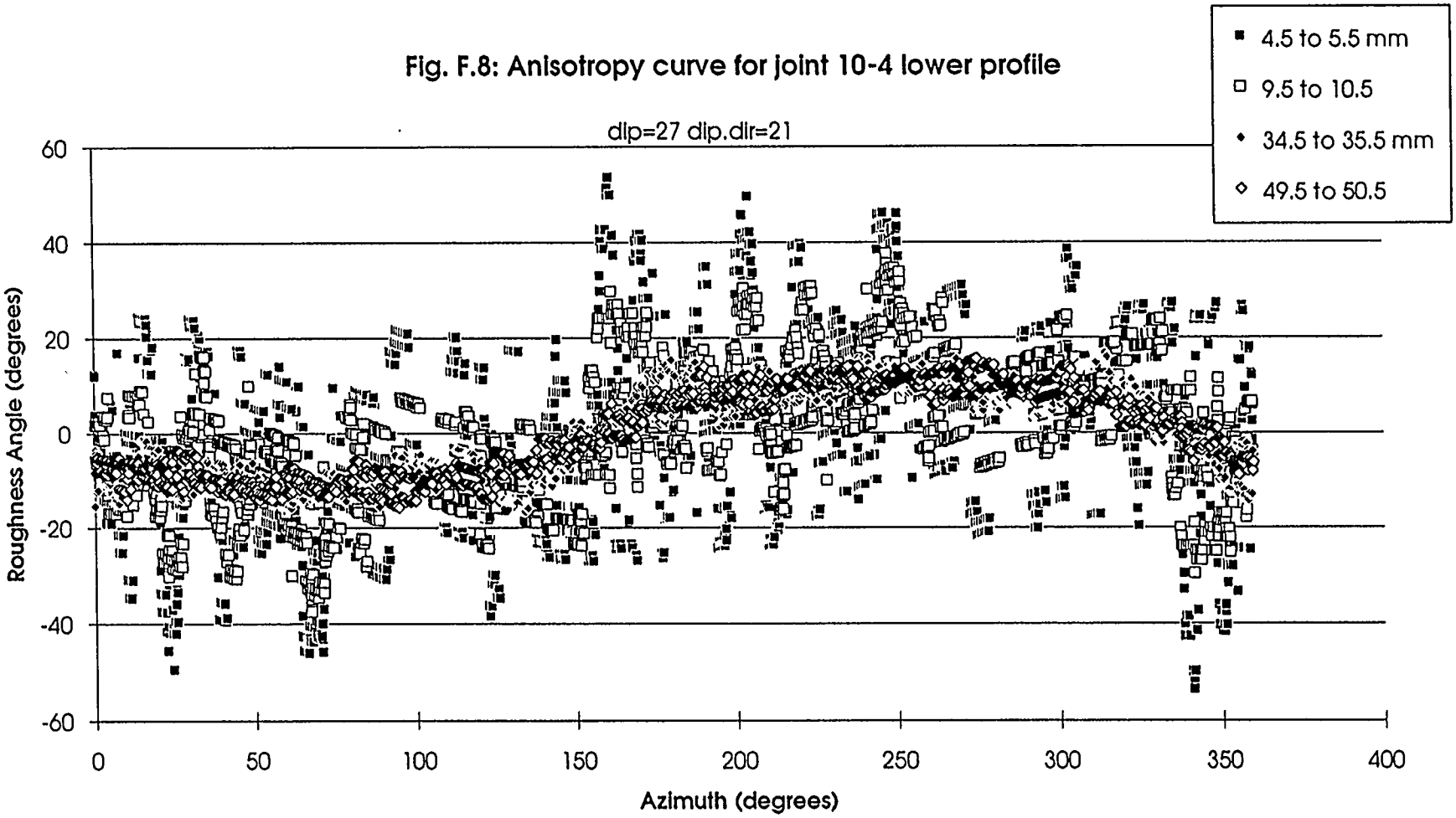

Fig. F.9: Anisotropy curve for upper profile of joint 19-1

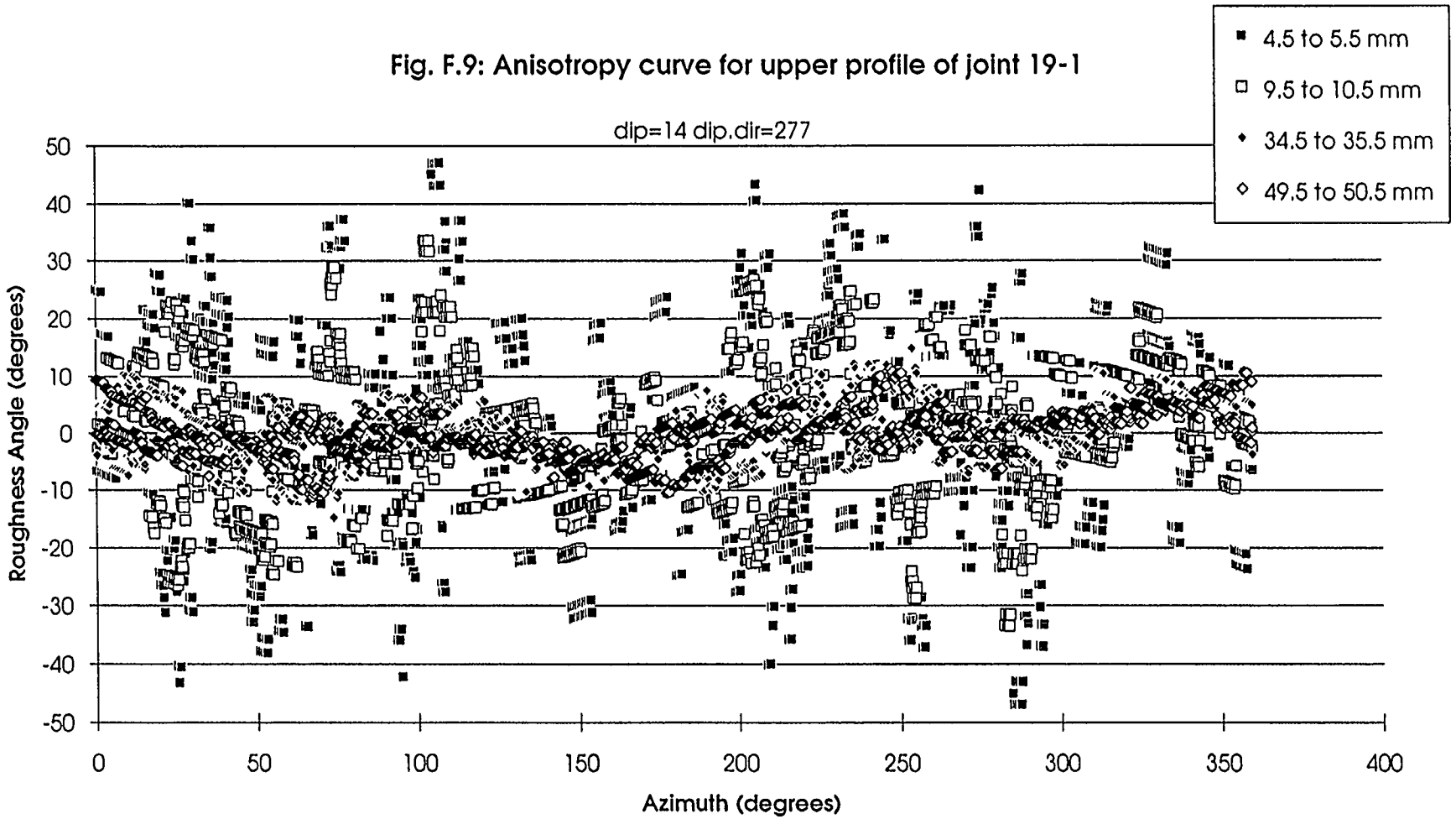

Fig. F.10: Anisotropy curve for lower profile of joint 19-1

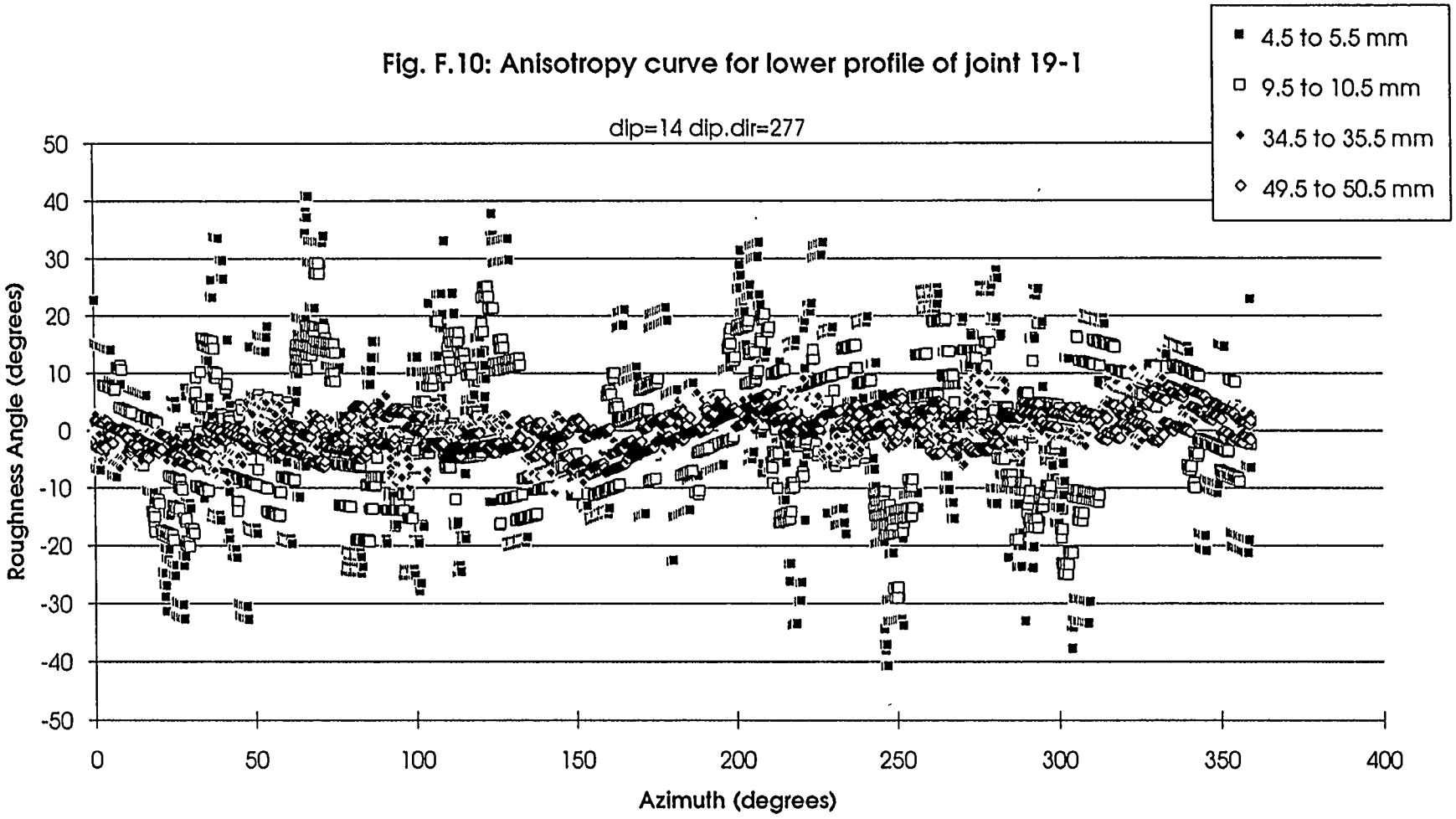

G. Results from aperture measurement synthetic experiment

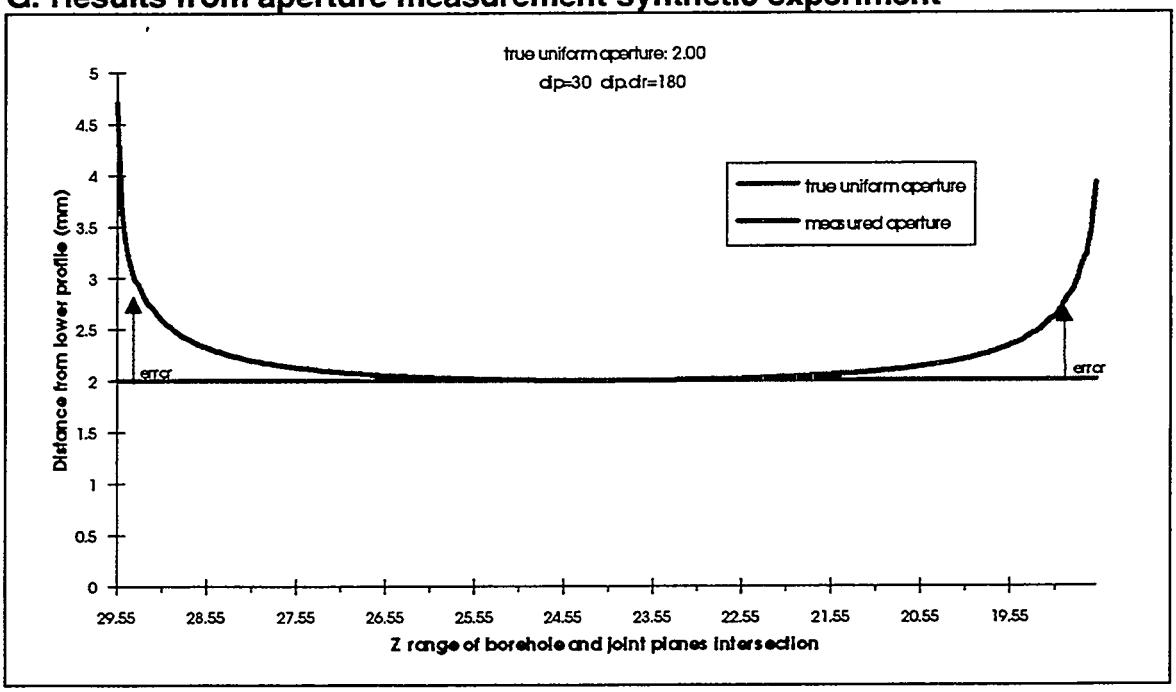

Figure G.1: Results of synthetic aperture measurement experiment for 30° dip

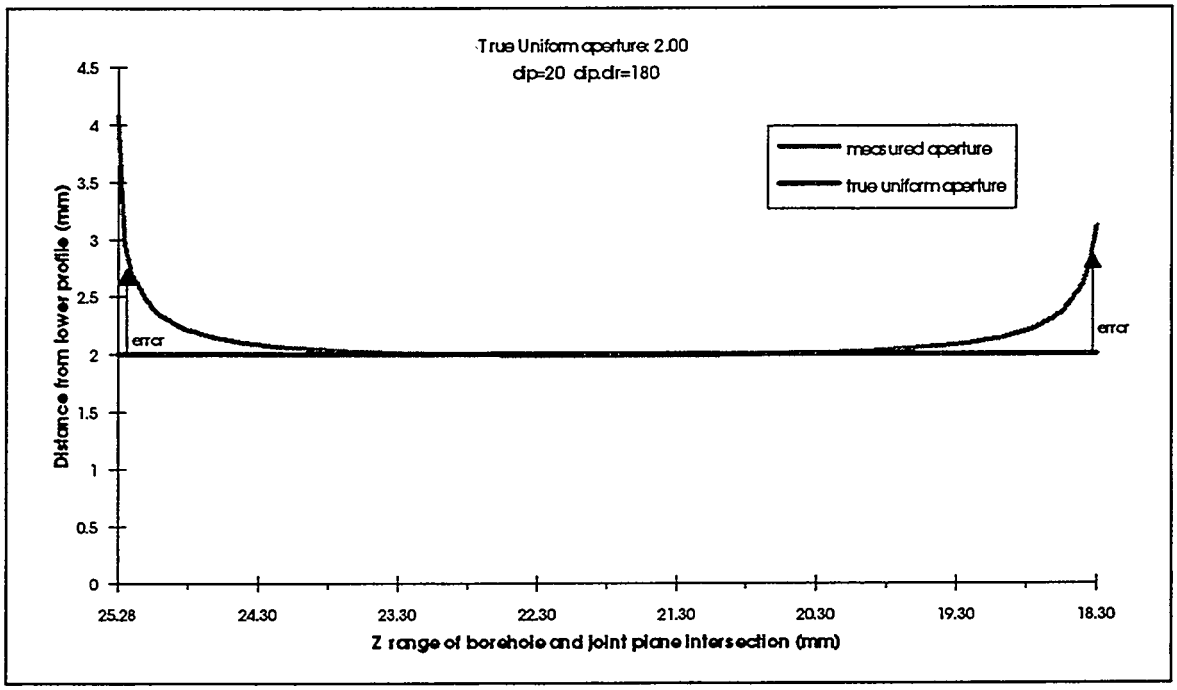

Figure G.2: Results of synthetic aperture measurement experiment for 20° dip

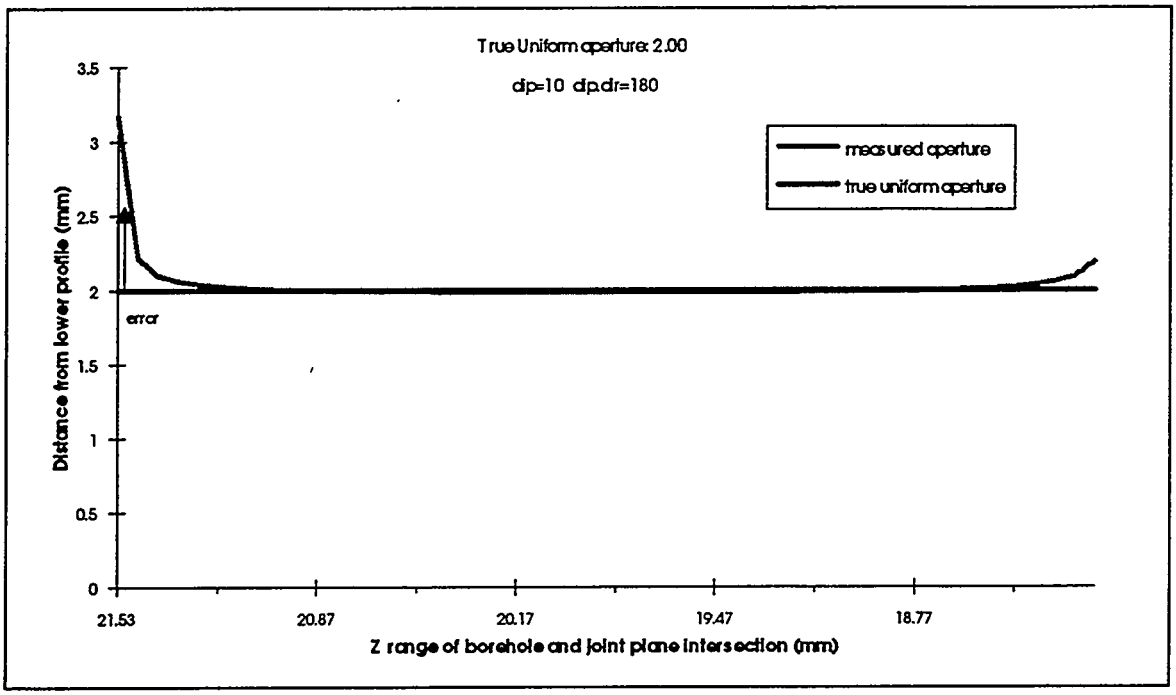

Figure G.3: Results of synthetic aperture measurement experiment for 10° dip

H. Verification of unrolling algorithm

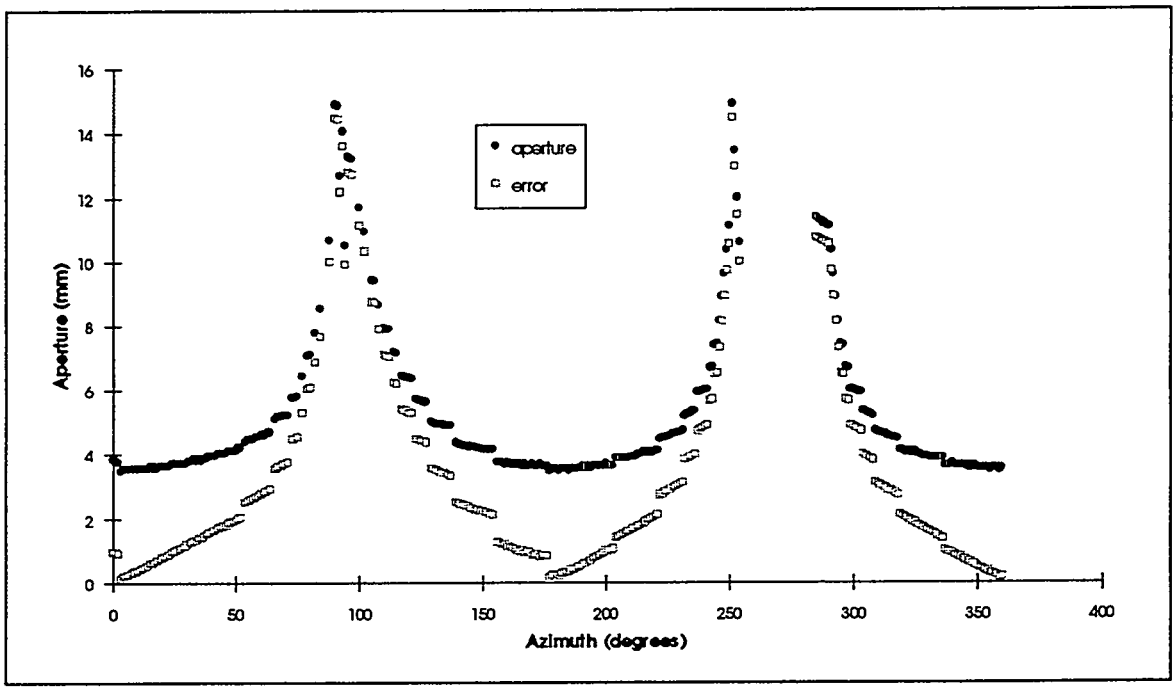

Figure H.1: Apertures of test data for verification of unrolling algorithm

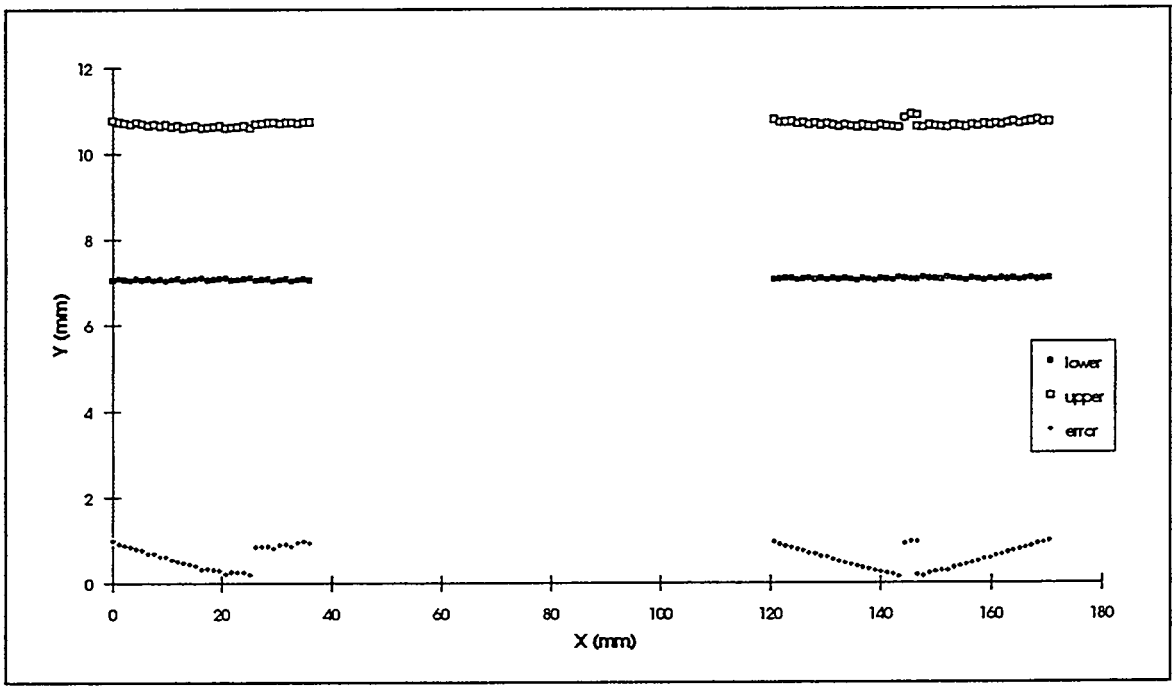

Figure H.2: Opposing profiles of test data for verification of unrolling algorithm

I. Examples of aperture measurements on joints in borehole 3-5

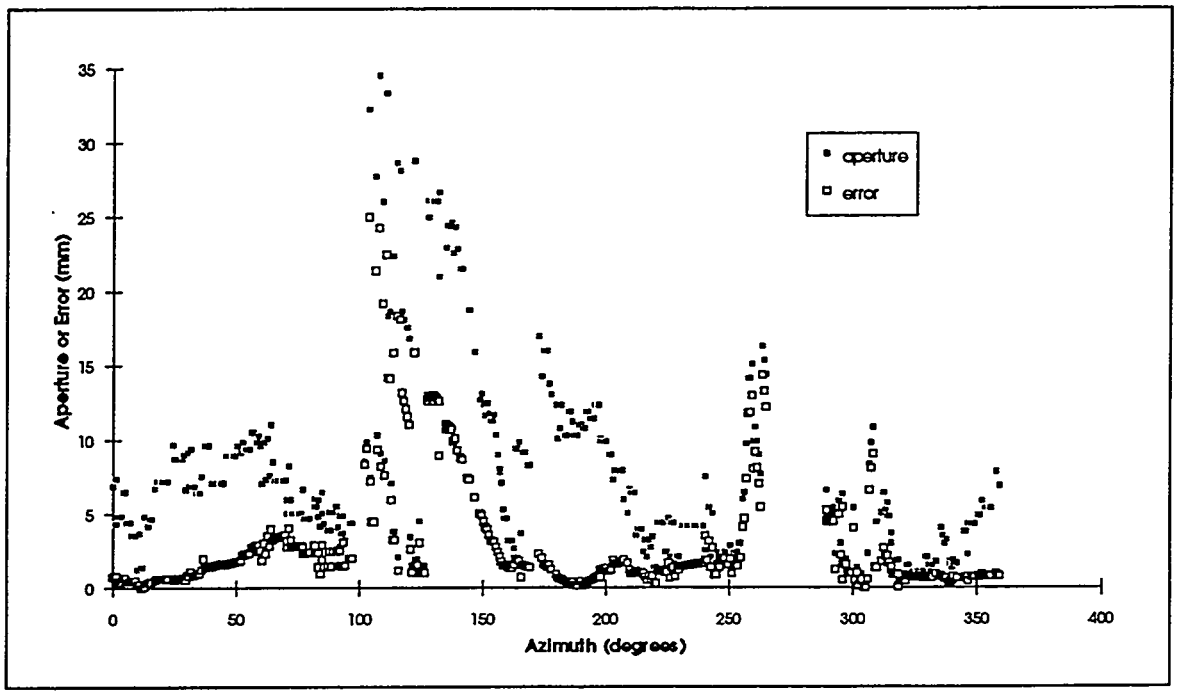

Figure I.1: Apertures and measurement errors for joint 18-1

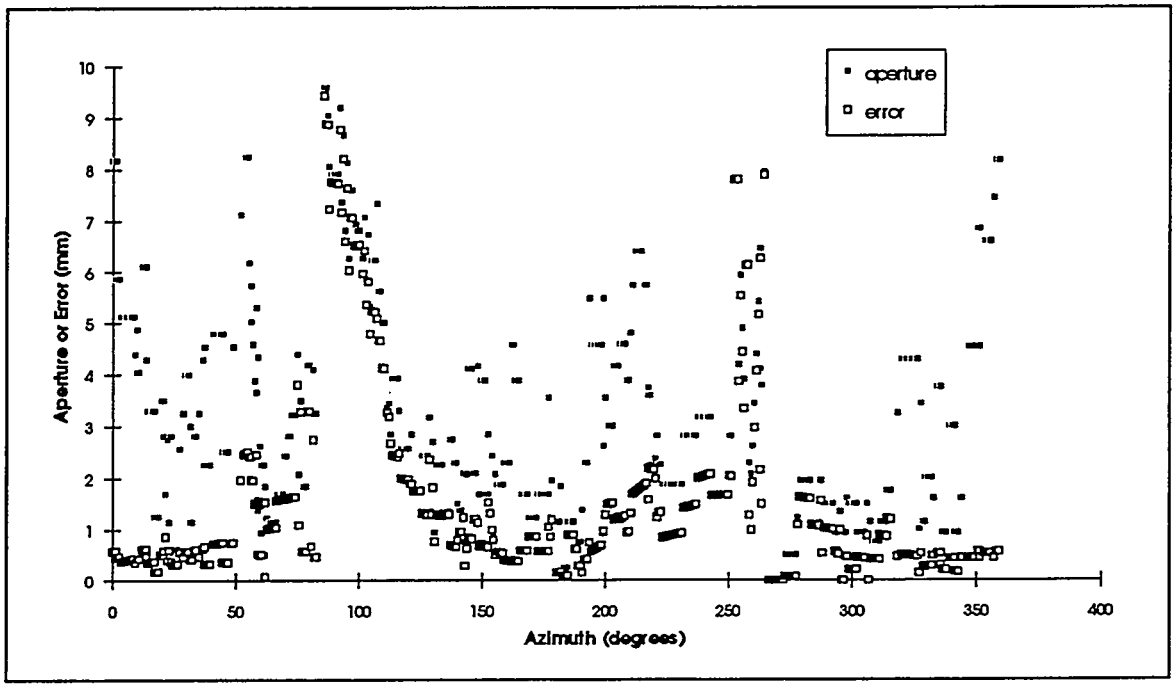

Figure I.2: Apertures and measurement errors for joint 19-2

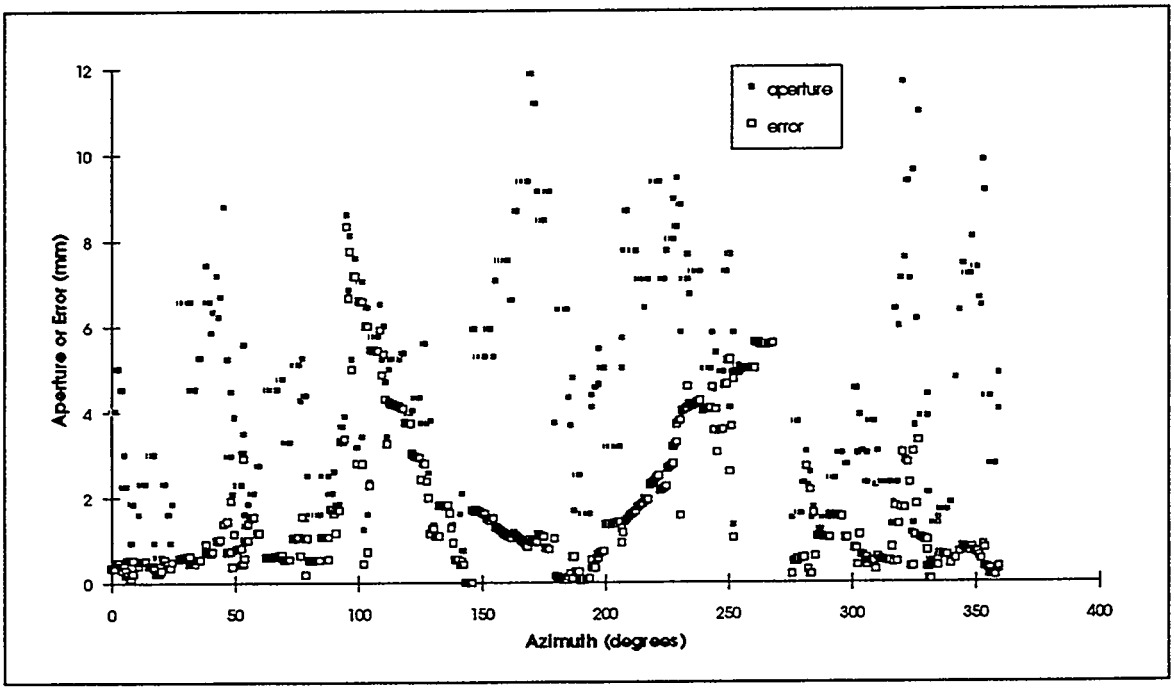

Figure I.3: Apertures and measurement errors for joint 19-3

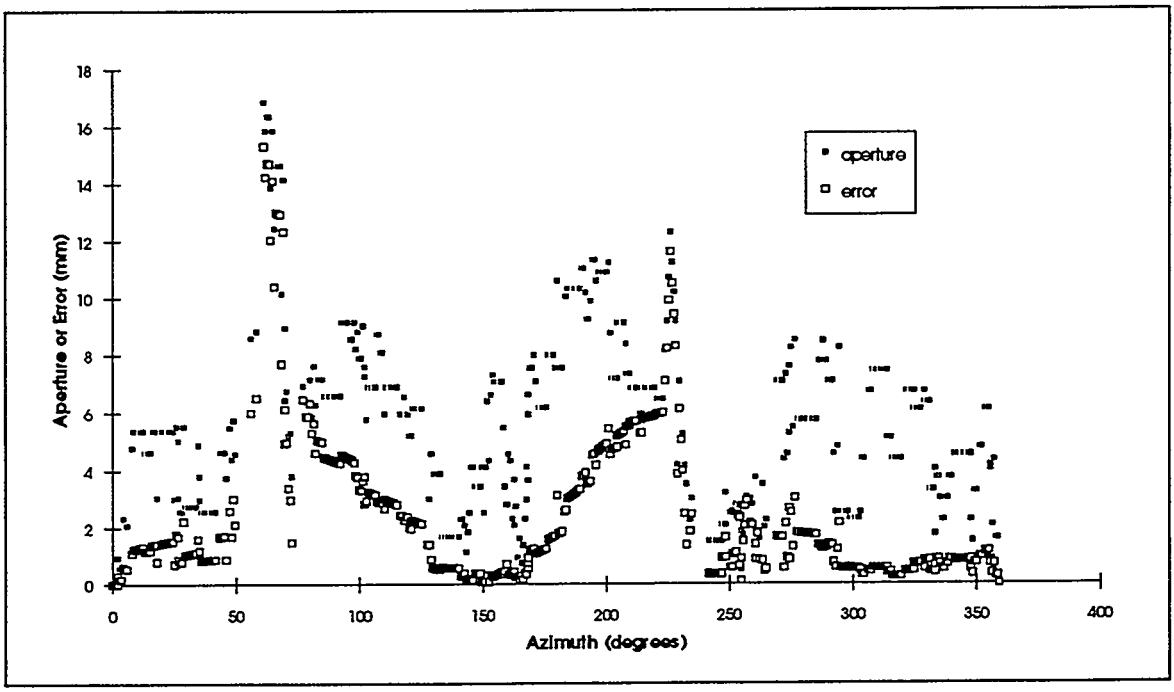

Figure I.4: Apertures and measurement errors for joint 19-4

J. Examples of unrolled profiles from joints in borehole 3-5

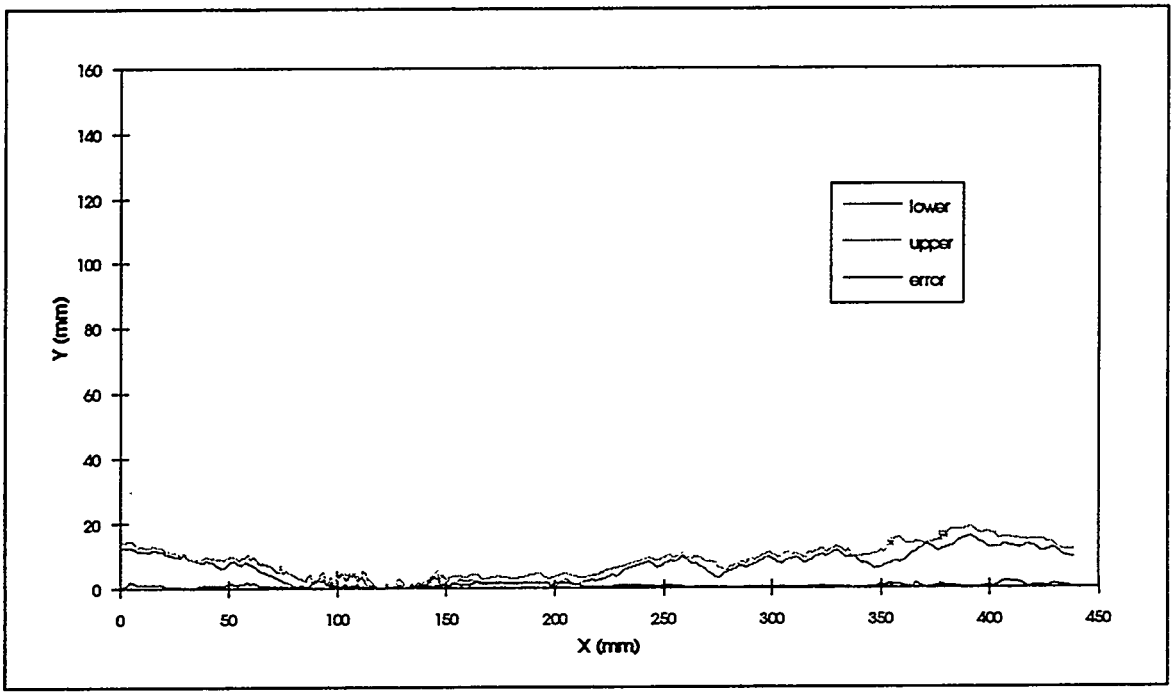

Figure J.1: Unrolled opposing profiles of joint 20-1

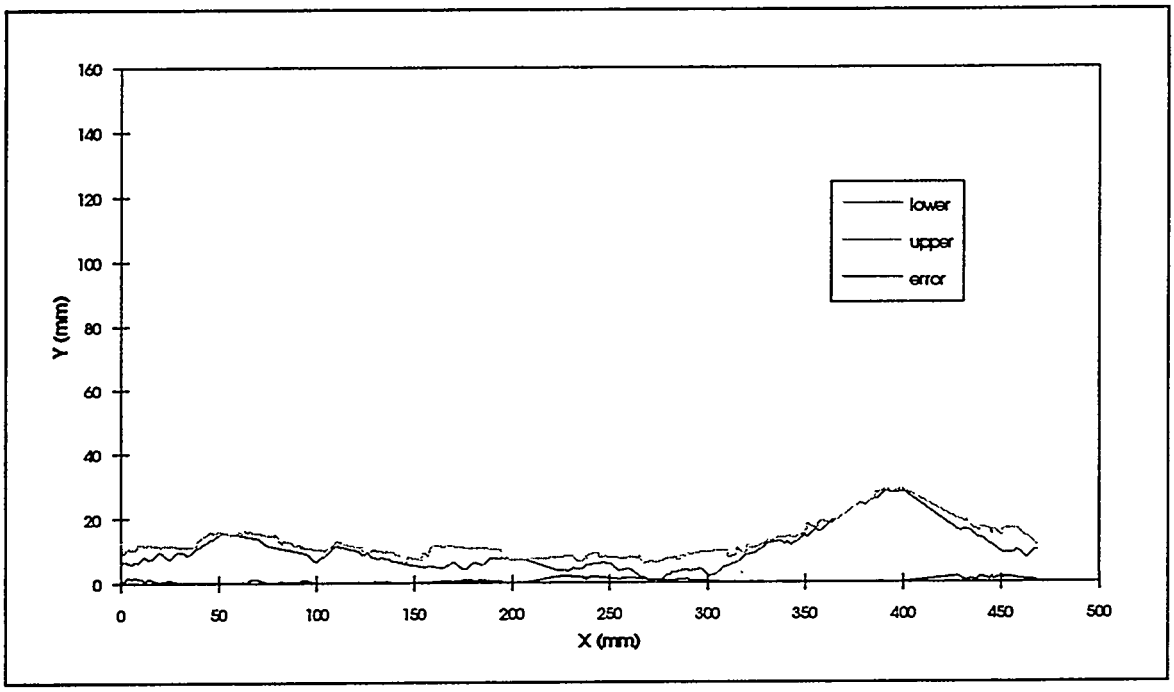

Figure J.2: Unrolled opposing profiles of joint 20-2

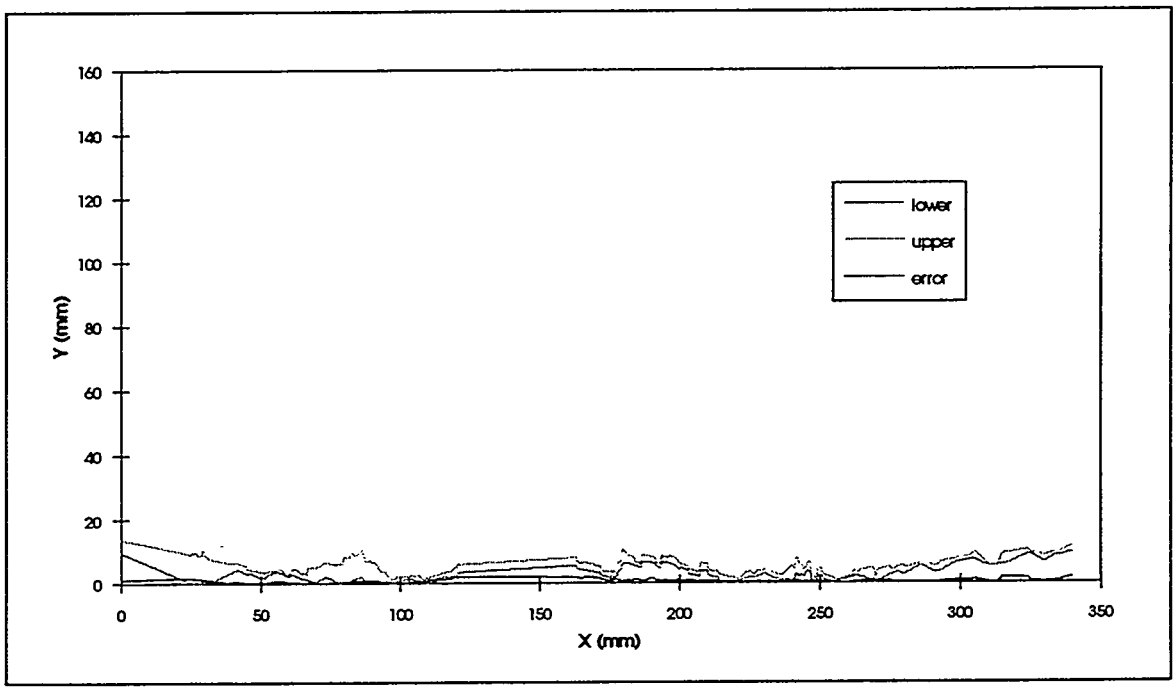

Figure J.3: Unrolled opposing profiles of joint 20-3

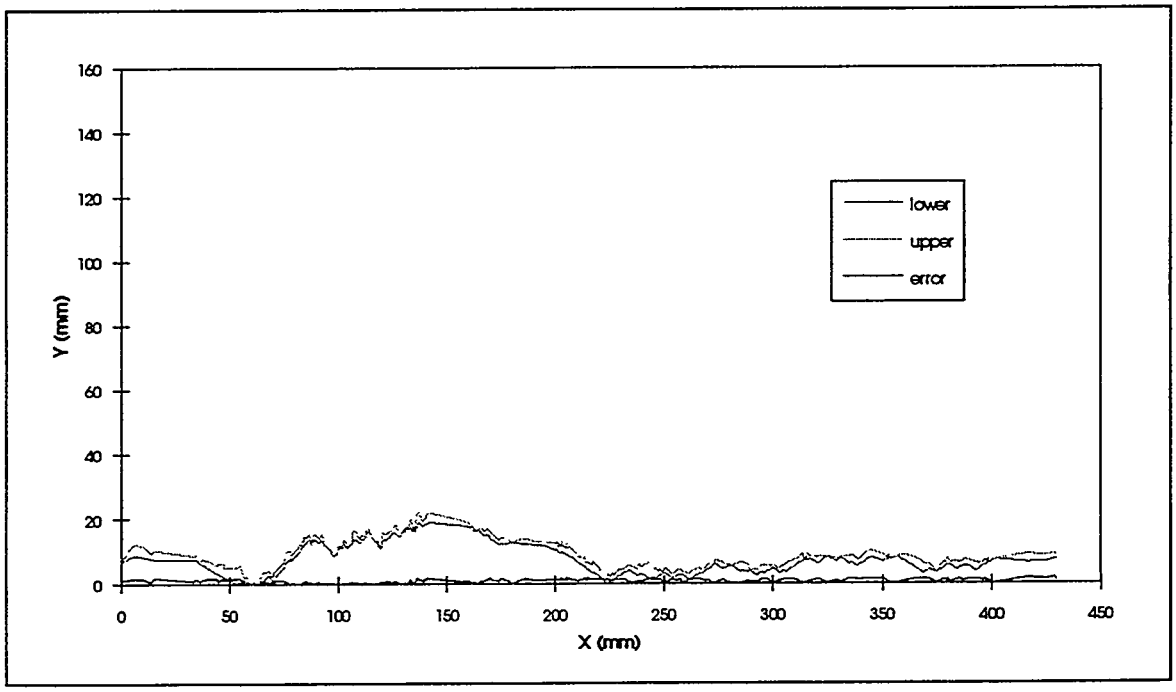

Figure J.4: Unrolled opposing profiles of joint 21-1